



Universiteit
Leiden
The Netherlands

Atomic-scale friction: thermal effects and capillary condensation

Jinesh, Kochupurackal Balakrishna Pillai

Citation

Jinesh, K. B. P. (2006, September 19). *Atomic-scale friction: thermal effects and capillary condensation*. Retrieved from <https://hdl.handle.net/1887/4562>

Version: Corrected Publisher's Version

License: [Licence agreement concerning inclusion of doctoral thesis in the Institutional Repository of the University of Leiden](#)

Downloaded from: <https://hdl.handle.net/1887/4562>

Note: To cite this publication please use the final published version (if applicable).

Atomic-Scale Friction:

Thermal Effects and Capillary Condensation

K.B. Jinesh

Atomic-Scale Friction: Thermal Effects and Capillary Condensation

PROEFSCHRIFT

TER VERKRIJGING VAN
DE GRAAD VAN DOCTOR AAN DE UNIVERSITEIT LEIDEN,
OP GEZAG VAN DE RECTOR MAGNIFICUS DR. D.D. BREIMER,
HOOGLERAAR IN DE FACULTEIT DER WISKUNDE EN
NATUURWETENSCHAPPEN EN DIE DER GENEESKUNDE,
VOLGENS BESLUIT VAN HET COLLEGE VOOR PROMOTIES
TE VERDEDIGEN OP DINSDAG 19 SEPTEMBER 2006
TE KLOKKE 13.45 UUR

DOOR

JINESH KOCHUPURACKAL BALAKRISHNA PILLAI

GEBOREN TE KAPICKAD, KERALA (INDIA)

IN 1978

Promotiecommissie

Promotor: Prof. dr. J.W.M. Frenken
Referent: Prof. dr. W. van Saarloos
Overige leden: Prof. dr. S.Yu Krylov (Russian Academy of Sciences, Moscow,
Russia)
Dr. E. Gnecco (Basel University, Switzerland)
Prof. dr. A. Fasolino (Radboud University, Nijmegen)
Prof. dr. P.H. Kes
Prof. dr. J.M. van Ruitenbeek
Dr. ir. T.H. Oosterkamp

Atomic-Scale Friction: Thermal Effects and Capillary Condensation

Jinesh Kochupurackal Balakrishna Pillai

ISBN-10: 90-921031-8

ISBN-13: 978-90-9021031-5

EAN: 9789090210315

A digital version of this thesis can be downloaded from

<http://www.physics.leidenuniv.nl/sections/cm/ip>

<https://openaccess.leidenuniv.nl>

The work described in this thesis was performed at the Kamerlingh Onnes Laboratory of Leiden University. This work is part of the research program of the Stichting voor Fundamenteel Onderzoek der Materie (FOM) and has been made possible by partial financial support from the Nederlandse Organisatie voor Wetenschappelijk Onderzoek (NWO).

to my beloved Parents and Brother

Table of contents

Chapter 1 Introduction to this thesis	1
1.1 Introduction	2
1.2 The Tomlinson model: how does motion lead to energy dissipation: friction?	4
1.3 Area of contact and adhesion in friction.....	8
1.4 The concept of superlubricity	10
1.5 Challenges in nanotribology	13
1.6 This thesis	14
1.7 References	18
Chapter 2 Instrumentation and Noise analysis	21
2.1 Introduction	22
2.2 Calibration of the Tribolover	24
2.3 Typical measurements: lateral force images and force loops.....	27
2.4 Noise analysis.....	28
2.5 Thermal effects and friction force measurements.....	32
2.6 References	33
Chapter 3 <i>Thermolubricity</i>: Temperature as a lubricant in atomic-scale sliding 	35
3.1 Introduction.	36
3.2 Modest thermal effects: the ‘thermal Tomlinson model’	37
3.3 Strong thermal effects: ‘thermolubricity’	39
3.4 Numerical evaluation of the rate equation: complete solutions	45
3.5 Experiments: effects of surface corrugation on friction.....	48
3.6 Discussion and conclusions	54
3.7 References	56
Chapter 4 Thermolubricity and velocity dependence of atomic friction.	57
4.1 Introduction	58
4.2 Thermal activation models and the velocity dependence of atomic friction.....	59

4.3 Fokker-Planck approach and velocity dependence of friction.....	61
4.4 Thermolubricity model and velocity dependence of friction	64
4.5 Experiments: velocity dependence in various friction regimes	71
4.6 Comparison between the experimental results and the thermolubricity model	74
4.7 Role of dimensionality in thermolubricity	82
4.8 Possible necessity for a multiple-mass-multiple-spring description.....	86
4.9 Summary	88
4.10 References	90
Chapter 5 Effect of forced excitations on atomic-scale friction	93
5.1 Introduction	94
5.2 Dependence of friction on excitation frequency	95
5.3 Friction at the lateral resonance frequency of the Tribolover.....	97
5.4 Interpretation.	98
5.5 Discussion	100
5.6 References	102
Chapter 6 Capillary condensation in atomic-friction experiments	103
6.1 Introduction: slippery when wet.....	104
6.2 When is a lubricant a lubricant?	105
6.3 Conflicting evidence on lubricating properties of water at the nanoscale ..	107
6.4 Lubrication by water – AFM studies.....	109
6.5 Capillary condensation.....	110
6.6 Experiments: friction and relative humidity	113
6.7 Mechanical behavior and velocity dependence of the capillary condensate....	116
6.8 Effective viscosity of the capillary condensation.....	122
6.9 Relaxation timescale of the condensate – additional evidence.....	124
6.10 A simple scenario to explain the tilting of the force loops	127
6.11 Conclusions	130
6.12 References	131

Chapter 7 Ice formation at room temperature and new physical phenomena in atomic friction	135
7.1 Introduction	136
7.2 Velocity dependence of friction at different relative humidities	138
7.3 Friction versus normal loads at high humidity	145
7.4 Summary of experimentally observed friction behavior.....	146
7.5 Conclusions	147
7.6 References	149
Chapter 8 Capillary condensation in atomic friction: large scan ranges.....	151
8.1 Introduction	152
8.2 Force loops at higher scan ranges	152
8.3 Writing ice.....	155
8.4 Dynamic response of the condensate line.....	156
8.5 Timescales and mechanisms	159
8.6 Conclusions	161
8.7 References	162
8.8 Appendix.....	163
Chapter 9 Conclusions.....	165
9.1 Summary of the work presented in this thesis	166
9.2 Future prospects: scientific challenges.....	168
Samenvatting.....	171
List of publications.....	177
Acknowledgements	179
Curriculum Vitae	180

Chapter 1

Introduction to this thesis

We discuss the basic concepts and models of atomic scale friction. This chapter further introduces the main subjects of this thesis, namely the role of thermal excitations and capillary condensation in atomic scale friction.

1.1 Introduction

Friction is the resistance to motion. Though seemingly simple and considered to be the one of the oldest scientific subjects in human history, the basic understanding of this phenomenon remains intriguingly incomplete. Friction is an irretrievable loss of energy and it seriously reduces the efficiency of the conversion and consumption of our energy resources. In view of the increasing need for energy and the decreasing resources of available energy, we recognize that understanding and controlling friction, lubrication and wear is very urgent and thus forms a highly relevant area of fundamental and application-oriented research.

The study of friction, lubrication and wear is known as ‘tribology’. The Greek verb τριβος means ‘to rub’ and hence the term represents the study of rubbing. The first documented study on friction was carried out by Leonardo da Vinci, about five centuries ago. But Leonardo’s insights remained unknown to the rest of the world until the 17th century when a French physicist, Guillaume Amontons, independently rediscovered and generalized two basic, empirical laws of sliding friction, namely that (a) friction is proportional to the applied normal force and (b) friction is independent of the contact area of the sliding surfaces. One century later, another French physicist, Charles Augustin de Coulomb introduced the third empirical law, namely that the friction force is independent of the sliding velocity, once sliding has started. Together, these three ‘laws’ are known as the Da Vinci-Amontons-Coulomb, or the Amontons-Coulomb laws of sliding friction, and they are of high technological importance [1].

The second friction law may look counterintuitive – after all, friction is brought about by the interaction between surfaces, which implies that the contact area should be of primary importance – but it works in practice. The explanation is that friction is generated at the contacts between micro asperities of the two sliding surfaces; in fact, friction *does* depend on the real area of contact, but not on the apparent contact area of the sliding surfaces. Amontons’ first law – friction is proportional to the normal load applied – is a simple consequence of the fact that for most practical surfaces the average contact area, e.g. the average number of micro contacts between the two surfaces, increases linearly with the applied normal force [2]. Although this allowed one to ascribe friction to the elastic and plastic effects of the micro-roughness of the sliding surfaces sliding, it did not reveal the truly microscopic origins of energy dissipation. As we will see later in this chapter,

experiments with atomically smooth surfaces that can exhibit substantial friction have shown that the interlocking of micro-asperities is not a necessary element of the energy dissipation mechanism.

Further progress in this research field had to await more refined instrumentation with a sensitivity for distances and forces down to the atomic scale. With the introduction of such techniques, only a few decades ago, the focus has shifted from large, multi-asperity contacts to the forces generated by individual, micron- and submicron sized asperities. This has given an enormous thrust to friction research, e.g. on dry friction between flat contacts and on the basics of lubrication. One example of the more complex instrumentation with high precision for force measurements is the Surface Forces Apparatus (SFA), an ingenious instrument developed by Tabor and Winterton in 1968 enabled the detailed study of atomically smooth (mica) surfaces in contact [3]. Studies with the SFA revealed that friction is highly sensitive to the atomic details of the contacting surfaces and that damage to the surfaces after overcoming the static friction force – wear – is not always associated with frictional motion (disproving the notion that friction is due to the rupture of molecular bonds between the sliding objects). This instrument is very popular for the study of the behavior of molecularly thin liquid films.

Jacqueline Krim and co-workers have developed the technique to use the Quartz Crystal Micro-balance (QCM) to investigate the behavior of smooth monolayers of molecules sliding over the surface on which they are adsorbed. Though the field of nano-scale friction and lubrication was developing at that time, the term *nanotribology* was first used by Jacqueline Krim and colleagues, in a publication that appeared in 1991 [4].

Although the SFA and the QCM are accurate enough to measure forces down to the scale of atomic friction, they suffer from the limitation of comparatively large areas of contact, typically of several square micrometers and more. Both instruments accurately trace the forces that arise during the collective motion of such large contacts. The key instrument presently dominating the new field of nanotribology is the Atomic Force Microscope (AFM), which has been invented in the mid 1980s by Binnig and coworkers [5]. The AFM really allows for nanoscale force measurements, as it naturally limits the contact size to the nanometer regime. With some care, even a single-atom contact can be investigated. Soon after its invention, Mate and colleagues adapted the AFM to measure lateral forces and they demonstrated the atomic-scale stick-slip motion of a sharp tungsten

tip over a graphite surface [6,7]. On the atomic scale, the tip apex, and with it the rest of the tip and the entire cantilever of the AFM, moved over individual rows of carbon atoms and dissipated energy much like strumming the strings of a guitar. This experiment has initiated a new approach in nanotribology. An Atomic force microscope used for measuring lateral forces is now referred to as a Lateral or Friction Force Microscope (LFM or FFM).

1.2 The Tomlinson model: how does motion lead to energy dissipation: friction?

The first model of friction that can be applied on the atomic scale has been introduced by L. Prandtl in 1928 [8] and by G.A. Tomlinson in 1929 [9]. Other models of atomic friction have been developed later [e.g. 10,11], highly inspired by the experiments of Mate *et al.*, but after more than seven decades the Prandtl-Tomlinson model still catches the essence of many of the more recent theories of friction.

The Prandtl-Tomlinson model adopts a very simple view of friction as the energy dissipated due to the sudden, irretrievable release of the elastic energy that is temporarily stored in the deformation, stretching or compression, of atomic bonds. In Tomlinson's own words, "*As the two bodies move relatively, there is a continuous change taking place in the pairs of molecules bearing the load, and the theory assumes that when two molecules come into contact, i.e., come into each other's repulsion field, and then separate, a loss of energy occurs which is manifest as friction*". At the time when Tomlinson formulated his model, it was meant to explain the molecular origin of macroscopic friction, i.e. to provide an atomistic view of the Amontons-Coulomb laws of friction. Tomlinson imagined a lattice where two atoms *A* and *B* as in Fig. 1 are in their equilibrium or stable positions. Atom *A* is fixed while atom *B* is allowed to move as if it were connected to *A* via a spring (with spring coefficient *k*). *C* is an atom belonging to the sliding upper surface that moves along a straight trajectory. When *C* approaches the attractive field of *B*, due to attraction, *B* lifts up, stretching its bond by an amount Δx . Once *C* has moved completely out of the attraction field, as sketched in the third geometry, *B* relaxes back and the energy associated with this relaxation is dissipated (to the lower surface). This energy is not retrievable, meaning that the energy is not conservative.

The Tomlinson model describes energy dissipation in a single contact between two surfaces. Real surfaces have a high density of asperities at which they make contact with one another. A reasonably successful attempt to extend the Tomlinson model to account for many-contact effects was made by Weiss and Elmer in 1996, combining it with the Frenkel-Kontorova model of a harmonic

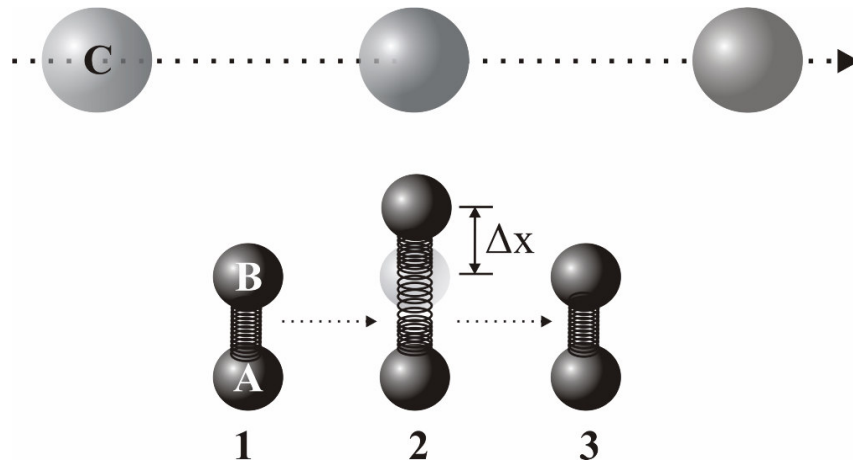


Fig.1.1. The Tomlinson picture of energy dissipation that causes friction. Geometry (1) represents a stable situation, where atoms A and B are in equilibrium positions. The upper atom C is far enough so that its effect on B is negligible. Geometry (2) represents the case when B is in the attractive field of C, and B stretches its bond with A. Geometry (3) is the final situation where C has moved sufficiently far that, B relaxes back. The energy dissipated in this picture is simply $\frac{1}{2} k(\Delta x)^2$, which is the elastic energy stored while stretching the chemical bond between A and B.

chain of atoms in a spatially periodic potential [12]. This is known as the Frenkel-Kontorova-Tomlinson (FKT) model of atomic friction [13]. Unlike models that propose the rupture of molecular bonds to cause friction [14,15], the FKT model assumes no chemical bonding between the asperity and surface atoms.

The general way of mapping the Tomlinson model on the geometry of an FFM is to associate atom C with the apex of an atomically sharp, rigid tip that is connected to the FFM cantilever, which responds to lateral forces on the tip apex by deforming with a spring coefficient k . The cantilever is connected to a rigid support. In this geometry, the flexible element (equivalent to the bond between A and B in figure 1.1) is placed on the side of the tip. Via the flexible cantilever, the

tip apex is dragged by the support through the potential of a rigid, regular surface lattice of periodicity a . The support position is denoted by X and the tip position by x . When the tip is dragged along the surface lattice, the deformation of the cantilever is simply $(X-x)$. The atomic potential of the lattice is usually approximated by a simple sine with amplitude U_0 . In this framework, the total potential energy of the system can be expressed as

$$U = -\frac{1}{2}k(X-x)^2 + \frac{U_0}{2}\left(1 - \cos\left(\frac{2\pi x}{a}\right)\right), \quad (1.1)$$

where the first term represents the elastic energy stored in the deformation of the cantilever and the second term is the sinusoidal atomic potential of the apex-substrate interaction. This combined potential is shown in Fig 1.2.

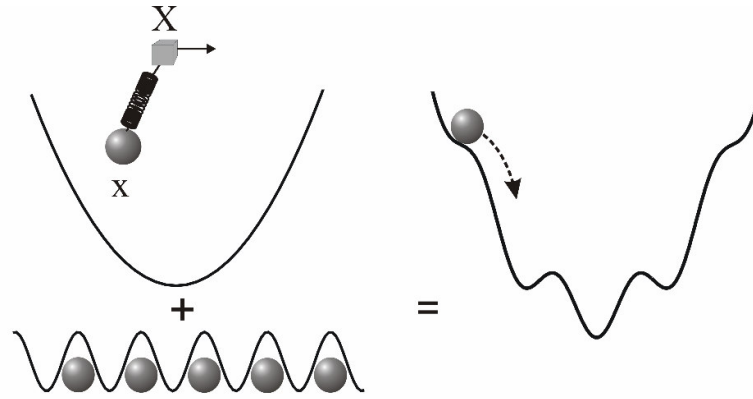


Fig.1.2. Application of the Tomlinson model to the geometry of an FFM experiment. The parabola on the left hand side represents the elastic energy stored in the deformation of the FFM cantilever and the sinusoidal potential below is the atomic potential corrugation of the interaction between the tip apex and the substrate lattice. The combined potential is shown on the right side, which is a corrugated parabola, which may have multiple local energy minima. The tip is held in one of these local minima. When the support position X is shifted this minimum changes depth. At a sufficiently large shift, the minimum vanishes, at which point the tip slips to the next potential minimum.

The position and depth of the local minima in this potential change with the support position X , which corresponds to shifting the parabolic (spring) contribution to the potential with respect to the fixed sinusoidal (lattice)

contribution. The tip is stuck in a local potential minimum until this potential minimum vanishes as a result of the movement of the support. At that point, the position of the tip becomes unstable and the tip slips to the next potential minimum. This cycle of sticking and subsequent slipping is repeated as long as the support moves, resulting in a stick-slip motion of the tip over the lattice of surface atoms. An inherent assumption in this description is that the energy that is released when the apex slips to the next energy minimum is dissipated completely and instantaneously. This actually means that the intrinsic, atomic-scale dissipation mechanism itself, which might be purely mechanical, via the generation of phonons in the substrate and the tip, or of electronic nature, via the generation of electron-hole pair excitations, is not really part of this model.

The results of an FFM observation can be presented in the form of a *lateral force image*, in which the color or brightness represents variations in lateral force, rather than the height variations usually shown in AFM images. When the force variations, $\pi U_0/a$, are sufficiently high and the sensitivity of the FFM is sufficiently good, atomic resolution can be achieved in these lateral force images. On a regular lattice a periodic pattern of successive stick-slip instabilities of the tip over the lattice atoms results. Now, following the same arguments of how stick-slip instabilities and hence atomic force variations can be observed with the FFM with a single-atom tip, atomic resolution is feasible even with an atomically smooth,

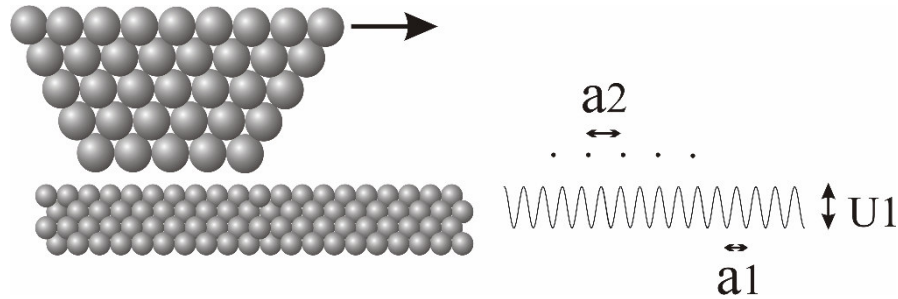


Fig. 1.3. Left: Sketch of a more realistic geometry of a friction measurement with an FFM. The tip is shown as a small piece of flat surface that consists of a few atoms that are touching the substrate simultaneously. **Right:** One-dimensional potential picture of the two contacting surfaces. Here, a_1 is the surface lattice constant and a_2 is the lattice constant of the tip. U_1 is the potential corrugation of the surface experienced by each of the tip atoms.

multi-atom area of contact. The reason is that the combined potential of all interactions over the contact area still exhibits a period, e.g. sinusoidal, variation with the periodicity of the substrate lattice [16].

The experimental situation is almost never that of a single-atom contact. Figure 1.3 shows the situation of a contact with a finite size, which is under a typical normal load of a few nanonewtons. If the lattice constants of the tip and the surface are different, then each atom on the tip side still feels the same atomic corrugation, with the same amplitude as the other tip atoms, but a different phase. Adding the potentials experienced by all atoms in the tip, the total potential for the tip as a whole will still show a corrugation with the period of the substrate, but the amplitude will be significantly reduced with respect to the situation of two matching lattices. This total potential still displays the atomic features of the substrate but local details, such as a missing atom or an atomic step, will appear smeared out over a width comparable to the tip radius. As an extreme consequence of this, atomic resolution has been claimed to be achieved in experiments with a macroscopically large graphite flake of 1 mm^2 area attached to a tip that was scanning over a graphite surface (the actual contact responsible for the stick-slip was thought to be limited to 96 atoms) [17]. Interestingly, there can be situations where the phase differences between the potential corrugations felt by the tip atoms are such that the amplitude of the total potential felt by the tip is equal or close to zero, thus making the contact insensitive to the atomic corrugation of the substrate and thus super-slippery. A trivial realization of this scenario in one dimension is the case where the tip diameter corresponds to an even number of atoms and the tip lattice spacing is 1.5 times the substrate lattice constant. We will return to this phenomenon below.

1.3 Area of contact and adhesion in friction

Friction has been proposed to be a phenomenon caused only by the surfaces of the sliding bodies. But is that really the case? The proposal by Zhong *et al* [10] was that the friction is related to the bonding energy between the surfaces, so that the friction coefficient is related to the adsorption energy of the sliding surfaces on each other. They showed that if a monolayer of Pd atoms slides over a graphite lattice, the coefficient of friction is very low because the adsorption energy of Pd on graphite is low. This theory neglects all effects of the atomic layers underlying

the sliding surfaces. In a comment on this work, J.B. Sokoloff argued that not only the atomic layers in contact, but the atomic layers lower to that also contribute to the dissipation process significantly [18]. That means, not only the chemical bonding between the atoms in contact but also the plastic deformation of the contact plays a prime role in dissipation. This is the essence of Bowden-Tabor model [19]. This assumption is valid in a wide range of contact areas. The Hertzian elastic theory for a sphere in contact with a plane, elastically deforming under an applied normal load, predicts that the contact area and hence the friction force is proportional to the 2/3rd power of the normal force applied ($A \propto F_N^{2/3}$). Adhesion between the sliding bodies enters this picture because it increases the contact area. This forms the essential ingredient that added to the Herz model by the Johnson-Kendall-Roberts (JKR) model, which introduces the adhesion forces between the surfaces via the surface tension γ . According to the JKR picture, the contact area would then be,

$$A = \pi(CR)^{2/3} \left(F_N + 3\pi\gamma R + \sqrt{6\pi\gamma R F_N + (3\pi\gamma R)^2} \right)^{2/3}, \quad (1.2)$$

where C is a constant that contains the elastic moduli and the Poisson ratios of the materials of the sphere and the planar substrate and R is the radius of curvature of the sphere (asperity). It is important to note that JKR theory predicts a non-zero area of contact even when the applied normal force is zero [19,20].

There are further, related theories for the adhesion and friction between single asperities. The DMT (Derjaguin-Muller-Toporov) theory allows deformation of the contacts under the influence of a normal force that includes the adhesion [21]. But, by contrast with the JKR model, the DMT model accounts for the adhesion between the entire surfaces, including those parts of the surfaces that are not in contact. A generalization of these theories exists in the form of the Maugis theory [22], with the disadvantage that it has to be evaluated numerically.

To investigate the force of adhesion between a surface and a nano-asperity, atomic force microscopes (AFM) are widely used. But it is extremely difficult to determine the precise contact area, in this case when the tip snaps away from the surface. This makes it difficult to quantify the relation between the contact area of the nano-asperity and friction at the nanoscale. An alternative is to use nano-clustered materials with different cluster sizes deposited on a well-defined surface

and drag them along the surface with an AFM tip. Nanoclusters of different sizes on the surface provide different areas of contact, which can be used to study the area-dependence of friction. There are recent nanoscale experiments to explore the area-dependence of friction, for instance, experiments using an FFM manipulating antimony nanoclusters of different sizes on a graphite surface [23]. Friction is in this case found to scale linearly with the contact area above a critical value of approximately $10,000 \text{ nm}^2$, below which the friction force was nearly zero. In fact, it was not long before that the origin of lubrication of graphite was revealed, which involves the atomic-scale geometrical details of the contacting surfaces [24]. A graphite flake of 3 nm diameter was shown to slide over a graphite surface with nearly zero friction in certain geometrical orientations, whereas a regular graphite crystal can not be sheared that effortlessly. These experiments indicate that there is an area of contact below which the traditional continuum elastic models break down. This critical area may depend on the elastic behavior of the sliding surfaces. Finally, there are recent theoretical investigations predicting that continuum mechanics cannot be applied on nanometer sized contacts, because the continuum theory breaks down at the atomic-scale surface roughness, in particular at atomically stepped surfaces [25,26], where a slight increase of surface area or normal force may cause a dramatic increase in friction force.

1.4 The concept of superlubricity

What could be the possible mechanisms that bypass the regular, elastic behavior of sliding contacts on the nanoscale? A plausible mechanism suggested by Hirano and Shinjo [27,28] is that smooth surfaces lock into each other on the atomic scale. To slide over one surface (which could be assumed to be a static substrate), the atoms of the sliding surface have to move either continuously (collectively) or by nonadiabatic (e.g. individual) jumping of the atoms. The first is called atomistic locking and the latter is dynamic locking. In this model, friction emerges from the top surface atoms jumping over the atomic potential of the lower surface. The transition between such dissipative sliding and the continuous sliding when the potential is made sufficiently weak is known as an Aubry transition [29].

When atomically smooth surfaces slide over another, the ratio of the lattice constants of the surfaces along the sliding direction can be either irrational or rational, in which case the contact is called ‘commensurate’. As explained in

section 1.2, when incommensurate lattices slide, individual atoms experience the same forces but the force variations on the individual atoms are all out of phase with respect to each other. The result is that energy temporarily invested in some atoms to overcome a local maximum in the atomic potential is compensated by the energy released by other atoms in the contact that are sliding into a local energy minimum. In effect, the total force acting on the contact is reduced and under certain conditions it can become so small that energy dissipation, i.e. friction, completely vanishes. Indeed, a spectacular reduction of friction has been demonstrated in computer simulations for two incommensurate copper lattices sliding over each other [30,31]. This situation of nearly vanishing sliding friction is called *superlubricity*. Alternatively, M. Müser has proposed to refer to this effect as *structural lubricity* [32-35]. Hirano and colleagues have claimed the first observation of a strong variation in the friction by changing the commensurability of the sliding surfaces in an STM study [36], but a more convincing proof of superlubricity has been provided in recent experiments by Dienwiebel *et al.* [24,37].

Superlubricity has important consequences in atomic friction. The potential corrugation of the surface, felt by the tip is a function of the normal force with which the tip is pushed onto the surface. i.e. $U_0 = U_0(z)$, where z is the height of the tip above the substrate. Therefore, when the sliding surfaces are in registry (commensurate lattices), friction increases with normal load. This is because, according to the Tomlinson model, the maximum force (F_{max}) the tip requires to slip over the surface potential barrier to the next potential well is $\pi U_0/a$, with a being the lattice constant of the surface. (Note that F_{max} is not the frictional force, but is the maximum lateral force in each slip event of the tip). Therefore, even at constant contact area, a commensurate contact should exhibit a friction force that depends noticeably on the normal load. When the lattices are incommensurate (and the normal load is low enough that the contact is superlubric) the tip finds stable positions everywhere along the sliding trajectory and the system shows (near) zero friction, independent of the normal load. Fig. 1.5 shows the load dependence of atomic friction when the lattices of a graphite flake and a graphite substrate are (a) commensurate and (b) twisted to an incommensurate contact.

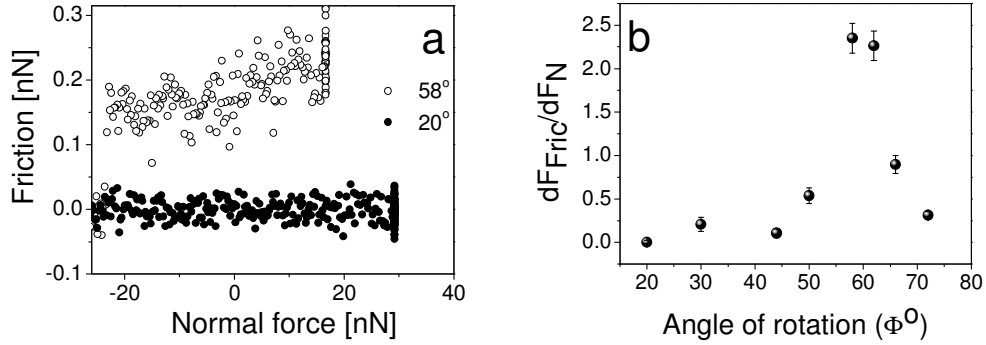


Fig. 1.5. (a) Dependence of friction on commensurability of a nanoscale graphite flake sliding over a graphite surface. When the lattices are twisted 20° out of registry the friction force is nearly zero and it exhibits no measurable dependence on the normal force. A significant load-dependence is evident when the system is twisted into registry (58°). (b) The slope of the friction versus normal load, a quantity related to the coefficient of friction, plotted against the twist angle. (Data analyzed from the experiments by M. Dienwiebel [37]).

What is so ‘super’ about superlubricity? There has been some discussion on the nomenclature. Unlike superfluidity and superconductivity, superlubricity is not a quantum phenomenon and when it occurs, friction is reduced strongly but not completely to zero [13]. The term superlubricity was originally introduced to indicate the possible vanishing of friction due to the lattice mismatch between two sliding surfaces. Later, this term has also been used to describe other types of significant reduction of friction. For example, the ultrasonic (or surface acoustic) wave induced reduction of friction is referred to as superlubricity [38]. In another context, exceptionally low energy dissipation of boundary-lubricated surfaces also has been referred to as superlubricity [39]. We will see in this thesis that friction can be suppressed under a well-chosen combination of several parameters, such as velocity, temperature, contact area, elasticity and even external force modulations that simultaneously influence friction. In this thesis the word superlubricity will be reserved for the vanishing of friction because of geometrical reasons, including the incommensurability effects and the potential corrugation effects.

Superlubricity can be described within the context of the Tomlinson model. There is a critical potential amplitude U_0 for the surface atoms to pin the tip and cause stick-slip motion and thus energy dissipation (friction). Below this amplitude,

only continuous variations in the elastic stretching and compression of atomic bonds occur and the motion becomes non-dissipative. The atoms simply follow the sliding body without pinning to the lower surface potentials. A detailed discussion is given in Chapter 3 of this thesis. We will refer to the emergence of friction when the surface potential exceeds this finite value as the friction transition [27,28].

1.5 Challenges in nanotribology

When two rough surfaces with a macroscopic area of apparent contact slide over each other, friction is the statistical average of a number of physical phenomena taking place in billions of micro and nano contacts. This multitude of phenomena includes plastic and elastic deformations of the contacts [40], inertia effects similar to what Tomlinson has already indicated [41], wear, where material is ruptured away [42], sound (phonon) generation [43], adhesion that pulls the surfaces close together (the principle with which a lizard can walk over walls and ceilings) [44], locking of the contacts by contaminants [45], rupture of bonds and electric charge transfer [46], electron-hole generation, charge density waves [47,48] etc. For example, phonon generation is associated with stick-slip motion of the surfaces, the same principle of sound generation from a violin. Each of these phenomena plays its own role and they may scale differently with the average contact size, thus possibly making practical, i.e. macroscopic friction quite different from what is observed in a single, nanoscale contact.

There are several motivations to work on nanotribology. First of all, investigating single, nanoscale contacts allows us to resolve the fundamental issues of energy dissipation at the atomic scale, elucidating the origin of friction by precise measurements with well-defined surfaces sliding over each other under fully controlled atmosphere, temperature and other conditions. On the other hand, since technology is proceeding to ever smaller components, the field of nanotribology is also generating practical knowledge and know-how for (future) applications. A good example is formed by micro and nano electromechanical systems (MEMS and NEMS). Lubrication by water or other common lubricants used in ordinary machines is not feasible in these miniature machines because of the large adhesive forces between the moving parts [49,50]. In particular, self-assembled monolayers (SAM) have been proposed to be a good candidate in this

respect [51], with tunable adhesive properties (depending on their hydrophobicity or hydrophilicity).

In dry cases, at smaller contacts such as in these devices, adhesion models may not work efficiently because the adhesion is dominated by Van der Waals forces at the nanoscale [52]. On the other hand, how a model lubricant works under practical conditions is still a matter of limited understanding [53]. Many computer simulations have been performed on lubrication in the last decade, many taking octamethyl cyclotetrasilane (OMCTS) and dodecane molecules as model lubricating systems. The preference for these molecules lies more in their structural properties that make the simulation tasks somewhat easier, than their practical use. OMCTS is a nearly ideal, hard-sphere molecule with a diameter of 9 Å, while dodecane is the prototype chain-like molecule. One-to-one correspondence between simulations and SFA experiments has been reported since late 1980s. But when the most important and simple lubricant – water – comes into play, everything gets complicated; theories as well as experiments yield strongly conflicting results [39,54,55]. Although the need for efficient, nanoscale lubrication for micro and nano electromechanical engineering is strong, the science of molecular-scale lubrication is still in infancy.

The biggest challenge in nanotribology is to bridge the gap between science and technology! Technology is advancing largely without detailed knowledge of the atomic-scale phenomena at work in friction. But at certain length-scales, technology is forced to meet the basic scientific principles. The adhesion between moving components of MEMS devices is a good instance to show this. Though the effects of Casimir and van der Waals forces have long been studied in science, they have identified to be prominent at length-scales of a few tens of nanometers causing stiction in MEMS and even worse in NEMS [52,56].

1.6 This thesis

Having reviewed several aspects of modern nanotribology, we finally concentrate on two fundamental aspects that are relevant for friction and lubrication under practical conditions: (1) *thermolubricity*, the effect of thermal excitations on friction and (2) *capillary condensation*, the phenomenon of water condensing in narrow cavities and its influence on atomic scale friction.

Thermolubricity:

The word thermolubricity refers to the lubricating role of thermal excitation in atomic-scale friction. We start our discussion of this phenomenon by a brief description of the experimental set-up in **Chapter 2** and an analysis of the intrinsic noise of the instrument, showing that the main contribution is thermal activation of the sensor. Exploiting this, we describe how thermal activation of an FFM tip affects atomic friction experiments in **Chapter 3**. We introduce a new approach to atomic friction using the Fokker-Planck equation. Though thermal activation of nano-asperities and its favorable consequences in sliding friction have been studied before, not much work has been performed in the extreme limit where thermal noise reduces the friction force nearly completely to zero, which could in principle be used for effective dry lubrication. Not many experiments have been reported at very low velocities either. A widely accepted concept is that thermal vibration of the FFM tip helps overcoming the potential barriers of the friction contact when the thermal energy $\frac{1}{2}k_B T$, on average available to the tip, is a noticeable fraction of the barrier height. This notion leads to the prediction of a friction force proportional to the logarithm of the sliding velocity [57,58] or at higher speeds following a 2/3rd logarithmic power-law-dependence on velocity [59,60]. This is a weak velocity dependence but we show that thermal excitation can also lead to a dramatic reduction of friction at the atomic scale and a nearly complete loss of atomic resolution in the force images, namely when the surface atomic barrier height is lowered to a value comparable to the thermal energy or when the system is given enough time to perform multiple thermal jumps per lattice spacing of support motion. We investigate the effects of surface corrugation on friction and find that even at high relative corrugation, the tip can show thermal jumps over the barriers and a systematic reduction of friction is demonstrated using our high-resolution friction force microscope. In **Chapter 4** we present velocity-dependent atomic friction measurements and demonstrate the multiple back and forth jumps of the tip resulting in a dramatic reduction (much more than logarithmic) of friction with reducing scan velocity.

Chapter 5 describes the effects of external vibrations on atomic friction. Here, instead of the natural, thermal vibrations of the tip, the cantilever is externally excited to much larger amplitudes, using an acoustic source. We find that even at higher amplitudes of vibration the tip still senses the atomic corrugation. This study

allows us to study the tip-sample interaction strength and possible practical implications of reducing friction with resonance vibrations of the sliding surfaces.

Capillary condensation:

Water vapor can undergo a first-order phase transition to the liquid state at relative humidities significantly below 100%, when confined to narrow (nano) cavities. This phenomenon of capillary condensation is well known in a variety of practical settings [61,62]. Water bridges thus forming between the surfaces increase the adhesion. Capillary condensation plays a role in sand piles [63] and it is one of the determining elements for the strength of seismic rocks [64,65]. Although water is known to be a good lubricant in every-day life, its lubricating properties are absolutely different in the context of nanoscale sliding. As mentioned in the previous section, this is still a controversial subject. FFM is an ideal tool to investigate the nanoscale lubrication properties of water since the contact sizes are very small and the adhesion forces can be estimated experimentally with high precision. Moreover, unlike the larger contact areas of a few square micrometers in the SFA, an FFM gives much smaller contact diameters where a few water molecules are trapped in a minute volume.

In **Chapter 6**, we study the effect of relative humidity (RH) on the sliding friction of tungsten on highly oriented pyrolytic graphite (HOPG), a combination of a hydrophilic and a hydrophobic surface. The RH is the key parameter, because it controls the dimensions of the water bridge between the tip and the surface. We show that water behaves amazingly differently in this confined geometry. Water acts like a glue that tends to hold the tip fixed to the HOPG surface. The water bridge exhibits mechanical behavior close to that of ice! The molecular relaxation timescales of the condensate estimated from these experiments are spectacularly long with respect to the characteristic reorientation times of normal water molecules. Low-velocity measurements reveal a lattice spacing that corresponds to the basal plane of the hexagonal ice lattice. The full variation of this behavior as a function of scan velocity and relative humidity will be presented in **Chapter 7**.

We have conducted attempts to drag the water capillary bridge by rapidly increasing the scan range. Instead of dragging the droplet along the hydrophobic surface, the tip writes temporary lines of ice on the surface, which increases the friction significantly. The ice lines drawn by the tip on the surface survive there for several seconds, again a counterintuitively long timescale. This strong memory

effect is evident to affect friction dramatically, and we discuss these aspects in **Chapter 8** of this thesis.

Chapter 9 concludes this thesis and summarizes the new physics revealed in our atomic-scale friction measurements.



1.7 References

1. B.N.J. Persson, *Sliding friction: Physical principles and applications*, Springer-Verlag Series, Berlin (1997), page 9.
2. J.A. Greenwood, J.B.P. Williamson, *Proc. R. Soc. Lond. A* **295**, 300 (1966).
3. D. Tabor, H.S. Winterton, *Nature* **219**, 1120 (1968).
4. J. Krim, D.H. Solina, R. Chiarello, *Phys. Rev. Lett.* **66**, 181 (1991).
5. G. Binning, C.F. Quate, C. Gerber, *Phys. Rev. Lett.* **56**, 930 (1986).
6. C.M. Mate, G.M. McClelland, R. Erlandsson, S Chiang, *Phys. Rev. Lett.* **59**, 1942 (1987).
7. C.M. Mate, R. Erlandsson, G.M. McClelland, S Chiang, *Surf. Sci.* **208**, 473 (1989).
8. L. Prandtl, *ZS f. angew. Math. u. Mech.* **8**, 85 (1928).
9. G.A. Tomlinson, *Phil. Mag. S.* **7**, 905 (1929).
10. W. Zhong, D. Tománek, *Phys. Rev. Lett.* **64**, 3054 (1990).
11. G.M. McClelland, in *Adhesion and Friction*, edited by M. Grunze and H.J. Kreuzer, Springer-Verlag Series, Berlin (1990), page 1.
12. Y.I. Frenkel, T. Kontorova, *Sov. Phys. USSR* **1**, 137 (1939).
13. M. Weiss, F.J. Elmer, *Phys. Rev. B* **53**, 7539 (1996).
14. A.E. Filippov, J. Klafter, M. Urbakh, *Phys. Rev. Lett.* **92**, 135503 (2004).
15. G.V. Dedkov, *Materials Letters*, **38**, 360 (1999).
16. S. Morita, Y. Sugawara, K. Yokoyama, S Fujisawa, *Fundamentals of tribology and bridging the gap between the macro-and micro/nanoscales*, edited by B.Bhushan, Kluwer, Dordrecht (2001), page 83.
17. K. Miura, N. Sasaki, S. Kamiya, *Phys. Rev. B* **69**, 75420 (2004).
18. J.B. Sokoloff, *Phys. Rev. Lett.* **66**, 965 (1991).
19. E. Meyer, R.M. Overney, K. Dransfeld, T. Gyalog, *Nanoscience: friction and rheology on the nanometer scale*, World Scientific Publishing, Singapore, 1998, page 18.
20. B. Bhushan, *Principles and applications of tribology*, Wiley-Interscience Publication, New York (1999).
21. B.V. Derjaguin, V.M. Muller, Y.U.P. Toporov, *Colloids and Surfaces* **7**, 251 (1983).
22. D. Maugis, *J. Colloid Interface Sci.* **150**, 243 (1992).
23. C. Ritter, M. Heyde, B. Stegemann, K. Rademann, U.D. Schwarz, *Phys. Rev. B* **71**, 85405 (2005).

24. M. Dienwiebel *et al.*, *Phys. Rev. Lett.* **92**, 126101 (2004).
25. B. Luan, M.O. Robbins, *Nature* **435**, 929 (2005).
26. J.N. Israelachvili, *Nature* **435**, 893 (2005).
27. M. Hirano, K. Shinjo, *Phys. Rev. B* **41**, 11837 (1990).
28. K. Shinjo, M. Hirano, *Surf. Sci.* **283**, 473 (1993).
29. S. Aubry, *Physica D* **7**, 240 (1983).
30. M.R. Sørensen, K.W. Jacobsen, P. Stoltze, *Phys. Rev. B* **53**, 2101 (1996).
31. M.R. Sørensen, *Computer simulation of Nanotribology for metals*, PhD Thesis, Technical University of Denmark, 1997.
32. M.H. Müser, *Phys. Rev. Lett.* **89**, 224301 (2002).
33. M.H. Müser, M.O. Robbins, *Phys. Rev. B* **61**, 2335 (2000).
34. M.H. Müser, L. Wenning, M.O. Robbins, *Phys. Rev. Lett.* **86**, 1295 (2001).
35. M.H. Müser, *Europhys. Lett.* **66**, 97 (2004).
36. M. Hirano, K. Shinjo, R. Kaneko, Y. Murata, *Phys. Rev. Lett.* **78**, 1448 (1997).
37. M. Dienwiebel *et al.*, *Surf. Sci.* **576**, 197 (2005).
38. T. Hesjedal, G. Behme, *IEEE Trans. Ultrason. Ferroelect., Freq. Contr.*, **49**, 356 (2002).
39. Y. Zhu, S. Granick, *Phys. Rev. Lett.* **93**, 96101 (2004).
40. A. Buldum, S. Ciraci, *Phys. Rev. B* **55**, 2606 (1997).
41. P. Reimann, M. Evstigneev, *Phys. Rev. Lett.* **93**, 230802 (2004).
42. R. Bennewitz *et al.*, *Phys. Rev. B* **60**, R11301 (1999).
43. A. Buldum, D.M. Leitner, S. Ciraci, *Phys. Rev. B* **59**, 16042 (1999).
44. M. Urbakh, J. Klafter, D. Gourdon, J. Israelachvili, *Nature* **430**, 525 (2004).
45. G. He, M.H. Müser, M.O. Robbins, *Science* **284**, 1650 (1999).
46. R. Budakian, S.J. Putterman, *Phys. Rev. Lett.* **85**, 1000 (2000).
47. H. Matsukawa, H. Fukuyama, *Phys. Rev. B* **49**, 17286 (1994).
48. A. Maeda *et al.*, *Phys. Rev. Lett.* **94**, 077001 (2005).
49. B. Bhushan, *Wear* **259**, 1507 (2005).
50. A.A. Polycarpou, A. Suh, *Fundamentals of tribology and bridging the gap between the macro-and micro/nanoscales*, edited by B.Bhushan, Kluwer, Dordrecht (2001), page 301.
51. E.E. Parker, W.R. Ashurst, C. Carraro, and R. Maboudian, *J. Microelectromech. Syst.* **14**, 947 (2005).
52. F.W. Delrio *et al.*, *Nature Mat.* **4**, 629 (2005).
53. O.M. Braun, M. Paliy, S. Consta, *Phys. Rev. Lett.* **92**, 256103 (2004).
54. M.L. Gee, P.M. McGuiggan, J.N. Israelachvili, *J. Chem. Phys.* **93**, 1895 (1990).

- 55. U. Raviv, J. Klein, *Science* **297**, 1540 (2002).
- 56. F.M. Serry, D. Walliser, G.J. Maclay, *J. Appl. Phys.* **84**, 2501 (1998).
- 57. J.N. Glosli, G.M. McClelland, *Phys. Rev. Lett.* **70**, 1960 (1993).
- 58. E. Gnecco *et al*, *Phys. Rev. Lett.* **84**, 1172 (2000).
- 59. T. Baumberger, P. Berthoud, C. Caroli, *Phys. Rev. B* **60**, 3928 (1999).
- 60. Y. Sang, M. Dube, M. Grant, *Phys. Rev. Lett.* **87**, 174301 (2001).
- 61. J.N. Israelachvili, *Intermolecular and Surface forces*, Academic Press, London, 2nd ed. (2002), page 330.
- 62. J. Jang, G.C. Schatz, M.A. Ratner, *Phys. Rev. Lett.* **92**, 85504 (2004).
- 63. L. Bocquet, E. Charlaix, S. Ciliberto, J. Crassous, *Nature* **396**, 735 (1998).
- 64. D. Broseta *et al*, *Phys. Rev. Lett.* **86**, 5313 (2001).
- 65. Y.Q. Song, S. Ryu, P.N. Sen, *Nature* **406**, 178 (2000).

Chapter 2

Instrumentation and Noise analysis

This chapter describes the special-purpose friction force microscope used in this thesis. We analyze the intrinsic noise in this instrument and show that it originates for a large part from the thermal vibrations of the cantilever. This opens the door for investigations of the role of temperature in atomic scale friction measurements.

2.1 Introduction

The prerequisite of an ‘ideal’ friction experiment is an ‘ideal’ friction force microscope (FFM). Since friction is a lateral force, the basic requirement of the instrument is simply the ability to measure the lateral forces in two dimensions with high resolution. Moreover, since adhesion between the FFM tip and the surface is inevitable even under ultrahigh vacuum (UHV) conditions, an ideal FFM has a force sensor that is relatively stiff in the normal direction. Usually, lateral forces are measured with regular, commercial atomic force microscopes (AFMs). In addition to the bending of the cantilever, from which one obtains the normal force, the torsion is measured to determine the lateral force. This approach has several disadvantages. Most importantly, the lateral force sensitivity is much less than the normal force sensitivity, because of the high torsional spring constants of common, ‘diving-board’ type cantilevers. This usually also has the consequence that the normal spring constant is so low that the tip snaps to contact with the surface during its approach, which can result in serious damage to the tip. Another disadvantage is that it is very hard with traditional cantilevers to measure lateral forces in *two* lateral directions, rather than just one. Several ingenious designs of friction force sensors and cantilevers are available, but most of them are highly complex in structure and methodology. A description of several alternative cantilevers can be found in Ref. [1].

To perform friction experiments with high resolution, we have developed a completely home-built friction force microscope that works in controlled ambient environments [1]. The specialty of our instrument is the dedicated friction force sensor called the Tribolover™, which has a geometry that is optimized for the above requirements for friction measurements: it has a high sensitivity to lateral forces in two dimensions and a high stiffness in the normal direction [2,3]. Figure 2.1 shows a scanning electron microscope image of a Tribolover™.

Unlike the standard AFM set-ups where the deflection of a laser beam, reflecting off the cantilever is used to measure the force experienced by the tip, we employ optical interferometry to detect the deformation of the sensor in response to lateral and normal forces. These sensors are made from (100) oriented p-type silicon wafers, using a combination of optical lithography, wet etching and highly anisotropic ion etching techniques. The pyramidal structure at the center of the Tribolover exposes four smooth (111) faces, each at a well-defined angle of 54.74°

with respect to the (100) plane. These (111) faces are obtained by wet etching of a carefully prepared, oxidized cross pattern in the silicon wafer. This selective etching creates very smooth and shiny facets, which act as ideal mirrors for the interferometry.

The ‘swastika’ shaped arms satisfy the combination of requirements on the spring coefficients of the force sensor. Prior to the fabrication, finite element analysis was used to calculate the optimal dimensions for this sensor. Typical dimensions of the arms are: length = 350 μm , width = 2 μm and height (thickness) = 10 μm . There can be slight variations in the width of the arms due to inhomogeneous etching. One important point of the sensor is that the tip is not fabricated together with it. Instead, the pyramid contains a central hole, in which we can attach tips of any material. This provides us with full flexibility in the choice of the material combinations for which we measure atomic-scale friction. In this thesis, we concentrate on a single combination, namely an electrochemically etched tungsten tip of nearly 100 μm length and a graphite (HOPG) surface.

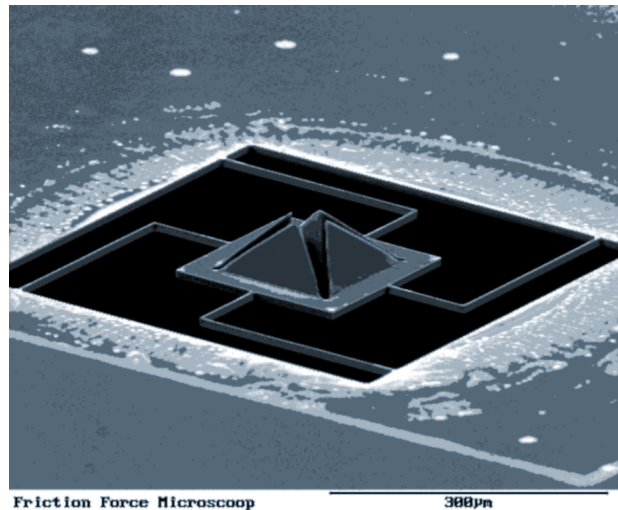


Fig. 2.1. Scanning electron microscope image of a TriboloverTM. The four faces of the open pyramid in the middle of the sensor act as highly reflective mirrors. Together with the polished end faces of four optical fibers, they constitute four separate optical interferometers. A sharp, electrochemically etched tungsten tip of 100 μm is inserted through the pyramid and glued in place, the sharp end of the tip thus protruding from the rear side of the pyramid. [2,3].

We use four optical fibers, etched and polished at the end, each pointing towards one of the four pyramid faces, to set up four simultaneously operating, optical interferometers. The laser beam coming through each of these optical fibers generates two reflections: one from the pyramid face to which it is pointing and the other from the polished end face of the fiber itself. These two reflected beams interfere with each other and the resulting intensity is measured by a photodiode, which is connected to a home-built amplifier. Each fiber is glued in a nanomoter that is used to bring the end face to within a few wavelengths (780 nm) from the pyramid face at such a distance that the derivative of the interference signal with respect to changes in the distance is at its maximum; this procedure maximizes the sensitivity. The optical path difference between the two reflections changes when the pyramid is displaced, either in the normal direction or in one of the lateral directions. In this way, each interferometer measures a projection of the three-dimensional displacement vector of the central pyramid. The combination of the four interferometer signals is used to accurately determine the components of this displacement along the X-, Y- and Z-directions. Standard RHK electronics is used to drive the scanning motion and control the data acquisition. It is also used for part of the data analysis. Home-built drift-compensation electronics allows us to counteract slow thermal drifts in the instrument with slowly varying offset voltages on the scan piezos. This allows us to perform scans at extremely low velocities, as low as 0.01 nm/s, without significant contributions to the tip speed due to thermal drift. A detailed description of the entire instrument is given in Ref. [1].

2.2 Calibration of the Tribolover

In order to convert the deflections of the pyramid of the Tribolover into forces, we need to calibrate the spring constants of the sensor in X-, Y- and Z-directions as accurately as possible. Such calibration is difficult in traditional AFM cantilevers, for which often an already calibrated cantilever is used or the thermal noise spectra is analyzed. The calibration of the Tribolover is rather straightforward. We record the thermal resonance vibration frequency of the cantilever using a Fast Fourier Transform (FFT) analyzer. We add spherical micro glass beads of different diameters (typically from 40 to 200 μm in diameter) on the rear side of the pyramid (before mounting the tip) and record the resonance frequency shift with the added mass. The mass of each micro glass bead can be estimated accurately using the

density of the material and the diameter of the bead as observed in an SEM or a high-resolution optical microscope. With this method we can routinely obtain a calibration accuracy of 4% along X, Y and Z.

For unclear reasons we have not been able to discriminate the resonance peaks of the Tribolover in the frequency spectrum of its displacement noise, even though the integrated noise level is only a factor 2 above the expected thermal noise level (see below). In order to still accurately measure the resonance frequencies of the Tribolover, we have used external excitation of the sensor with a loudspeaker connected to a sine wave generator, with which the sound frequency was ramped from 0 to 50 kHz. The lowest X, Y and Z resonance frequencies of the cantilever are below 50 kHz and these resonances are excited by the sound from the loudspeaker. If there are inhomogeneities in the dimensions of the X and Y arms because of the inhomogeneous etching, we sometimes observe split resonance peaks corresponding to the resulting, small differences between the spring constants in the two lateral directions. In practice, we choose those cantilevers that have the equal X and Y spring constants, within 2%. Adding the mass of a glass bead shifts the resonance frequencies to lower values. If k is the Tribolover spring constant, M is the (effective) mass of the sensor and m is the added mass, the resonance frequency of the cantilever ν is given by

$$\nu = \frac{1}{2\pi} \sqrt{\frac{k}{M + m}} \quad (2.1)$$

A plot of the mass of the glass micro-beads against $1/(2\pi\nu)^2$ should then be a straight line with a slope k . Figure 2.2 shows the calibration plots for the Tribolover used in most of the experiments in this thesis. From the slopes of the two straight lines we obtain a lateral spring constant of $k_{X,Y} = 6.1 \pm 0.23$ N/m and a normal spring constant of $k_Z = 30.5 \pm 1.31$ N/m.

After the calibration of the sensor, we attached an electrochemically etched tungsten tip at the rear side of the sensor. We used an NaOH solution to etch a long tungsten wire with a diameter of 125 μm and the sharp end of the tip was cut to a length of 100 μm . We used a micromanipulator to pick up the tip and position it in the central hole of the sensor's pyramid without damage to the tip or the sensor. Silver epoxy was used to glue the tip in place. Scanning electron microscope images of such a sharp tungsten tip are shown in Fig. 2.3.

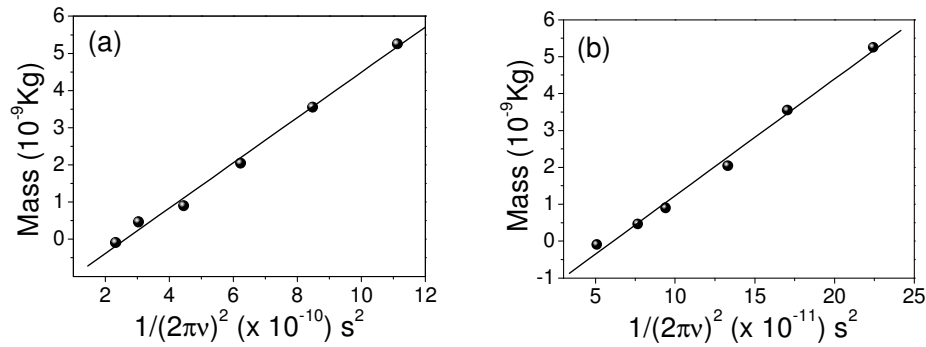


Fig. 2.2. Tribolover spring constant calibration plots. (a) Calibration in the X- and Y-directions gives a (common) lateral spring constant of $k_{X,Y} = 6.1$ N/m. (b) Calibration in the Z-direction gives a normal spring constant of $k_Z = 30.5$ N/m. The error bars are smaller than the size of the points, which derive from minor uncertainties in the estimates of the diameters of the glass micro-beads.

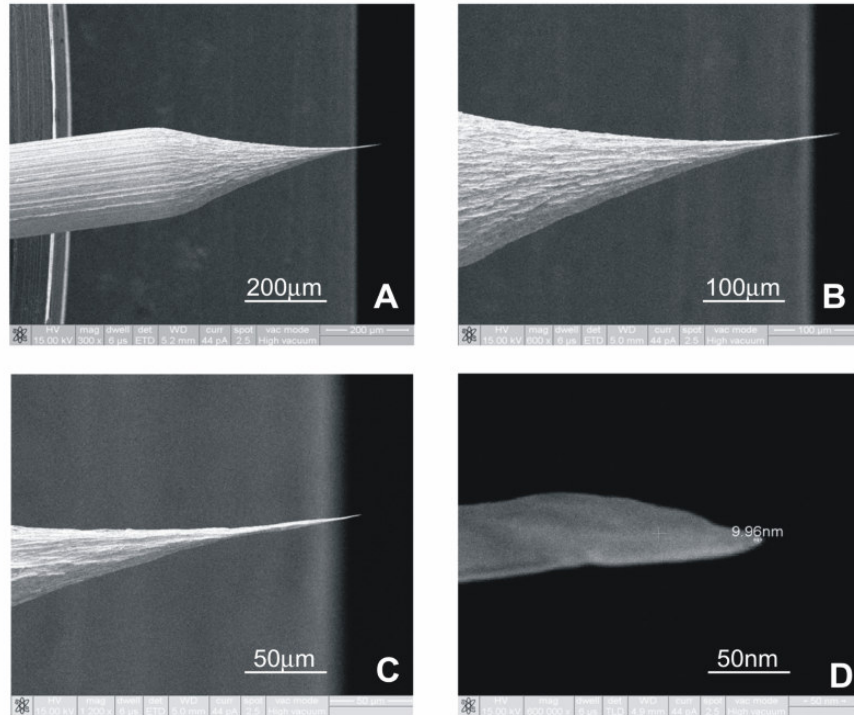


Fig. 2.3. SEM images of a typical FFM tungsten tip we used for friction measurements. The mean radius of curvature of the tip apex is about 5 nm in this case.

2.3 Typical measurements: lateral force images and force loops

In our system, the Tribolover together with the optical fiber system is fixed and we scan the sample by applying voltages to a piezo tube that is connected to the sample holder. The lateral range of this piezo tube is approximately $2\text{ }\mu\text{m}$, but in this thesis we have limited the scans to smaller ranges of to 250 nm . A typical lateral force image on highly oriented pyrolytic graphite (HOPG) and a single force loop are shown in Fig. 2.4. In this scan, the feedback electronics was used to continually adjust the vertical tip position in order to maintain a constant normal force of 3.7 nN . The parallel, horizontal lines in the image indicate that the scan direction was oriented parallel to a high-symmetry direction of the graphite lattice.

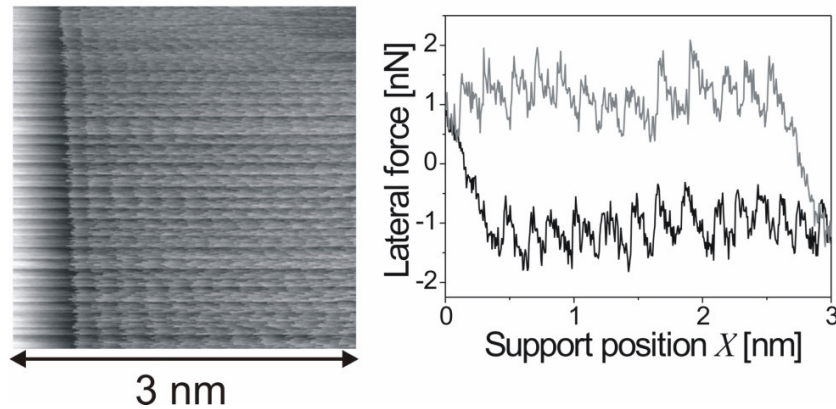


Fig. 2.4. Typical lateral force image (forward direction; left panel) and force loop (one forward scan line in black and the reverse line in grey; right panel) obtained with the Tribolover with a tungsten tip on the graphite (HOPG) surface. The scan range is 3 nm and the image contains 512×512 pixels. The normal force was fixed at 3.7 nN and the scan velocity was 30 nm/s . The image has a vertical band at the left side, which can also be recognized in the force loop and reflects the build-up of sufficient lateral force at the beginning of each scan line to initiate sliding over the atoms in the lattice. The motion of the tip over the graphite lattice exhibits clear stick-slip character (vertical stripes in the force image and saw-tooth structure in the friction loop). The period of this motion corresponds to the graphite basal plane lattice constant of 0.246 nm . The friction force is defined as the average lateral force (after the initial force build-up part of the scan lines).

The total energy dissipated while the tip is dragged along the substrate lattice during one friction loop is given by the area enclosed by the loop. What we

measure in experiments is only the lateral force experienced by the support (the Tribolover pyramid in this case). The loop has a static part in the beginning, while the tip is stuck to the initial atomic potential well, and the force builds up until the derivative of the force becomes equal to the effective spring constant of the cantilever-and-tip combination. At this point the tip slips to the next energy minimum and the stick-slip process is repeated until the scan direction is reversed. The friction force is the average force experienced during the stick-slip part of the scan. It corresponds to the average amount of energy dissipated per unit of sliding distance.

Generally, the system can be thought to behave as the combination of two spring constants: (1) the spring constant k_T of the cantilever and (2) the so-called contact stiffness k_C , which is again a combination of two spring constants, namely the spring constant corresponding to the interaction between the tip and the surface and the tip compliance, i.e. the elasticity of the tip itself. The slope of the initial, ‘static’ part of a friction loop corresponds to all these spring constants acting in series and is known as effective spring constant, k_{eff} [4,5,7].

$$\frac{1}{k_{eff}} = \frac{1}{k_T} + \frac{1}{k_C} \quad (2.2)$$

Obviously, the most flexible element in this combination will dominate the initial part of the force loop and usually this is *not* the cantilever. The calibrated Tribolover™ has a spring constant of 6.1 N/m and measuring the slope of the initial force build-up in the friction loops similar to that shown in Fig. 2.4, we estimated an average k_{eff} of 4.5 N/m. This directly gives the contact stiffness $k_C = 17.2$ N/m. It means that the contributions from the tip-compliance and the tip-substrate adhesion play significant roles in determining the signal when the tip is in contact with the surface.

2.4 Noise analysis

Even though the atomic lattice of the HOPG can be recognized in the force map, Figure 2.4 looks convoluted with a high level of intrinsic noise, which makes it difficult to see the individual atoms in the lateral force image. This noise is also clearly present in the individual friction loop in Fig. 2.4. We may expect the

following three sources of instrumental noise: (1) thermal vibrations of the cantilever, (2) noise in the laser used in the interferometry (intensity variations and mode switching) and (3) electronic noise (both in the detection and the scan electronics). In addition to these intrinsic sources of noise, relative vibrational motion of the tip and the sample, resulting from external excitation (acoustic noise and building vibrations) will be introduced when the tip is in contact with the substrate. Here we concentrate on the intrinsic sources by keeping the surface far away from the tip. Figure 2.5 shows a typical noise recording, with the noise signal expressed in equivalent force units. The force signals in Fig. 2.5 were filtered by a low-pass filter, set at a cut-off frequency of 1 kHz, as was used in most of our friction measurements.

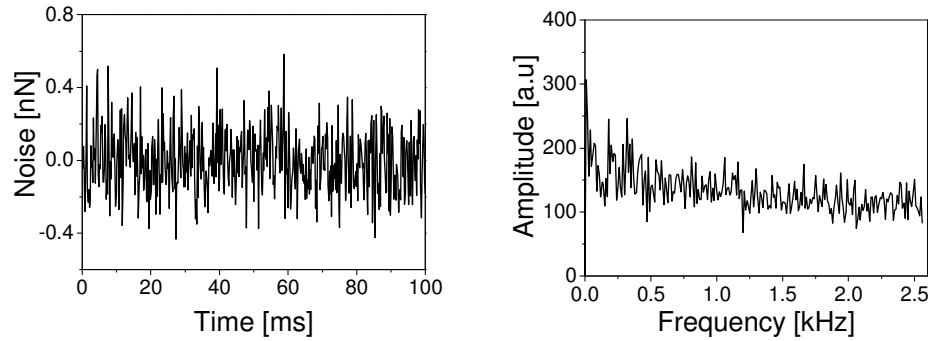


*Fig. 2.5. **Left:** Noise recorded by the sensor when the tip is not in contact with the surface. The signal is the combination of thermal, laser and electronic noise in the detection part of the instrument. The sweep time was 100 ms and the band width of the low-pass filter was set to 1 kHz. **Right:** Averaged Fast Fourier Transform (FFT) of signals showing no special frequency appearing in the spectrum.*

Let us consider the thermal vibrations of the cantilever. The amplitude (root mean square displacement) X_T , with which the cantilever is vibrating is determined by the thermal energy stored in the cantilever [6].

$$\frac{1}{2}kX_T^2 = \frac{1}{2}k_B T, \text{ from which we obtain} \quad (2.3)$$

$$X_T = \sqrt{\frac{k_B T}{k}},$$

where k is the spring constant of the cantilever, k_B is the Boltzmann constant and T is the temperature. The corresponding force noise (rms force variation) amounts to

$$F_T = kX_T = \sqrt{kk_B T} \quad (2.4)$$

This simple estimate shows that the standard deviation of the position of a thermally vibrating cantilever with an elastic constant of 6.1 N/m will be 0.026 nm at $T = 300$ K. The corresponding standard deviation of the (lateral) force will be 159 pN. Figure 2.6 shows the distribution of the force variations, which is described well by a Gaussian with a standard deviation of 148 pN, which is very close to the calculated value.

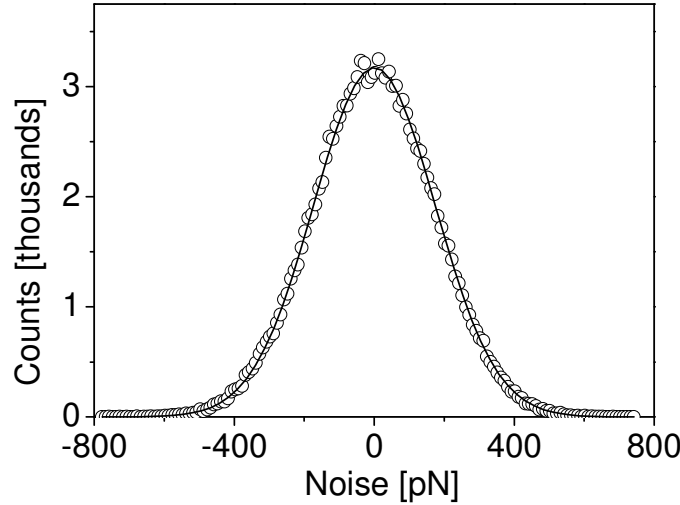


Fig. 2.6. Distribution of the noise in signals like that shown in Fig. 2.5, recorded when the tip is far away from the surface. The bin width of the distribution is 10 pN. The open circles are the experimental data and the solid curve is a Gaussian fit. The distribution has a width of 148 pN.

The seemingly good agreement between the measured noise amplitude and the expected amplitude is fortuitous, the width of the experimental distribution being limited severely by the low-pass filter, which was set at a of 1 kHz low frequency, which is low with respect to the resonance frequency of the cantilever of 3.6 kHz. In addition, the pixel frequency in most of our measurements, including those in Fig. 2.5, was limited (5120 Hz), which introduces an additional, digital low-pass filtering.

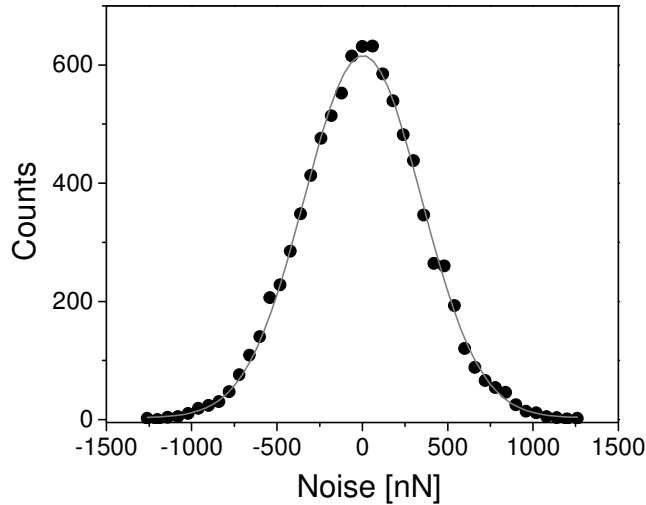


Fig. 2.7. Distribution of the noise in friction loops when the pass-filter is at 10 kHz. The grey line is the Gaussian fit to the data, with a standard deviation of 291.5 pN. The loops were measured at a scan velocity of 30 nm/s.

Using a pass filter with a bandwidth of 10 kHz in the detection electronics, we allow most of the thermal motion of the cantilever to be recorded and processed. This gives a much more realistic estimate of the noise level of the system.

The Gaussian distribution of the noise when the pass-filter is at 10 kHz as shown in Fig. 2.7 gives a standard deviation of 291.5 pN. The fact that this number is not significantly different from the width measured with the tip out of contact implies that the possibility of relative motion of the sample with respect to the tip does not introduce additional noise in the instrument. Since the theoretically estimated thermal noise of 159 pN is roughly a factor 2 below the observed noise level, additional sources of noise must be present in the system. We can rule out significant heating of the Tribolover (and thus stronger thermal excitations) due to laser heating of the pyramid because of the low laser power and the high reflectivity of the pyramid surface. The fact that we observe a Gaussian distribution suggests that the source of extra noise is also not the coupling in of acoustic noise (sound) or building vibrations. We assume that the extra noise is due to variations in the laser power and to electronic noise generated by the photodiodes and the detection electronics.

The fact that we did not observe any significant reduction of noise in the signal when the tip was made in contact with the surface indicates that the additional noise present is from the instrument. When the tip is in contact with the surface, the spring constant that would influence the noise is $k_T + k_C = 23.3$ N/m. The reduction in the noise due to this new spring constant by the tip touching the surface is only about 10%, which means that the majority of the noise in the signal when we use 10 kHz pass-filter is purely instrumental.

2.5 Thermal effects and friction force measurements

In addition to being a source of noise in the measurement, the thermal motion of the cantilever and tip should also be regarded as a phenomenon in itself that influences the stick-slip mechanism of atomic friction. The role of thermal excitations has been discussed extensively in recent literature [8-10]. Actually, temperature can act as an efficient lubricant for sliding motion [10]. At normal forces of a few nano Newtons, commonly used in atomic-friction measurements, the corrugation of the interaction potential between a tip and the graphite surface, i.e. the height of the potential barriers, is in the range of 0.2 to 0.5 eV, depending, of course, on the number of tip atoms in contact with the surface. These barriers are only one order of magnitude higher than the thermal energy at room temperature (0.025 eV), which must mean that thermal excitations do play an important role during a large fraction of the stick-slip trajectory, when the remaining energy difference with the top of the nearest barrier is only a few $k_B T$. As we will see, most of the noise in measurements such as those in Fig. 2.4 results from thermally assisted sliding of the tip. In the next chapter we discuss the theoretical background of such thermal effects and study their role in our friction experiments in more detail.



2.6 References

1. M. Dienwiebel, *Atomic-scale friction and superlubricity studied using a high resolution friction force microscopy*, PhD thesis, Leiden University, The Netherlands, 2003.
2. T. Zijlstra, J.A. Heimberg, E. van der Drift, D. Glastra van Loon, M. Dienwiebel, L.E.M. de Groot, J.W.M. Frenken, *Sensors and Actuators A: Physical* **84**, 18 (2000).
3. M. Dienwiebel *et al.* *Rev. Sci. Instrum.* **76**, 043704 (2005).
4. E. Meyer, R.M. Overney, K. Dransfeld, T. Gyalog, *Nanoscience: friction and rheology on the nanometer scale*, World Scientific Publishing, Singapore (1998), page 83.
5. R.W. Carpick, D.F. Ogletree, M. Salmeron, *Appl. Phys. Lett.* **70**, 1548 (1997).
6. H.J. Butt, B. Cappella, M. Kappl, *Surf. Sci. Rep.* **59**, 1 (2005).
7. M. Dienwiebel, N. Pradeep, G.S. Verhoeven, H.W. Zandbergen, J.W.M. Frenken, *Surf. Sci.* **576**, 197 (2005).
8. J.N. Glosli, G.M. McClelland, *Phys. Rev. Lett.* **70**, 1960 (1993).
9. E. Gnecco *et al.*, *Phys. Rev. Lett.* **84**, 1172 (2000).
10. S.Yu Krylov, K.B. Jinesh, H. Valk, M. Dienwiebel, J.W.M. Frenken, *Phys. Rev. E* **71**, 65101(R) (2005).

Chapter 3

Thermolubricity: Temperature as a lubricant in atomic-scale sliding

The influence of thermal excitations on atomic-scale sliding is investigated in this chapter by a combination of analytical modeling, numerical calculations and FFM experiments. We explore various regimes of conditions where the thermal effects dominate. Our model predicts that even if the potential energy barriers are an order of magnitude higher than the thermal energy $k_B T$, thermal effects can noticeably change the sliding. The theory also covers the situation that thermal excitations make the tip perform multiple backward and forward jumps to neighboring potential wells, which leads to a significant reduction of friction. Re-analyzing recently reported experiments on superlubricity of a graphite flake sliding over a graphite surface, we identify a sizeable thermal contribution to the suppression of friction in these experiments.

3.1 Introduction

A growing number of technological applications require low friction between moving components but do not tolerate traditional lubricants. For instance, under the extreme conditions of space applications, in machines working at high temperatures and in instruments that operate in ultrahigh vacuum, common liquid lubricants cannot be used. On the other hand, in machines that are applied in clean conditions solid lubricants in powder form, such as graphite and molybdenum disulphide can often not be used. A special class of instrumentation with its own friction and lubrication problems is that of micromachines and nanotechnology. As we discussed in Section 1.5 lubrication by liquids does not work in MEMS technology, because of the large adhesive forces between the moving microscopic parts that are introduced by the liquids. In fact, even the capillary condensation of water in a MEMS structure can be sufficient to stall the device completely and even damage it. Efficient techniques to lower and control dry friction are thus extremely desirable. Several promising approaches exist for this, namely *superlubricity* (Chapter 1), the use of thermal excitations [1] and the use of externally excited lateral resonant motion of the moving parts [2].

As early as in 1928, L. Prandtl has recognized the effect of temperature and predicted the reduction of friction of macroscopic sliding objects due to thermal activation [1]. Although Prandtl considered friction in a rather generic context, not describing the nano-scale details of the phenomenon, the results of his model capture the essence of the lubricating role played by temperature. It has taken seven decades to demonstrate the importance of Prandtl's predictions, because, with the advent of the atomic force microscope (AFM) and especially the friction force microscope (FFM), it has become possible only recently to investigate these thermal effects experimentally on the atomic scale. As we saw in the first two chapters, measurements on this scale can be performed with an atomically sharp AFM or FFM tip that is dragged over a crystal lattice under a modest normal load. The tip is connected via a flexible cantilever with a well-defined, lateral spring constant k to a rigid support.

If we start by neglecting the role of thermal excitations, we can describe the motion of the tip within the framework of the Tomlinson model [3] (see Chapter 1). In the absence of thermal excitations, the only force available to make the tip overcome the atomic potential barriers is the spring force exerted by the support via

the cantilever. That is, the tip mechanically slips to the next potential minimum when the combined system of the cantilever and the tip-surface interaction becomes unstable, which is the case when the tip is at a location where the second derivative of the surface potential U with respect to the tip position x is equal to the spring constant of the cantilever (i.e. $d^2U/dx^2 = k$). As the consequence of this dragging, the tip repeatedly slips over the atomic barriers with a saw-tooth-like variation of the lateral force, which is known as stick-slip motion [4]. There are two important implicit assumptions within the Tomlinson model. First, the tip resides always in a (local) minimum of the total potential (tip-surface interaction potential plus elastic energy of the deformed cantilever). Secondly, in every slip event the tip dissipates its excess energy instantaneously and completely, i.e. the motion of the tip in the local potential energy well is overdamped. The landscape of local minima and maxima in the combined potential experienced by the tip changes continually with the motion of the support, new local minima being formed and existing ones being removed every time the support is moved over one lattice spacing of the substrate. When the depth of the local minimum in which the tip resides is reduced to zero the tip slips to the next minimum. We refer to these unstable points where the tip has to slip to the next potential minimum as *critical points*. At zero absolute temperature, the stick-slip motion of the tip faithfully reproduces the lattice of these critical points, which has precisely the same symmetry and lattice constants as the substrate lattice.

Thermal excitations assist the tip in overcoming the barriers prior to the critical points mentioned above. This introduces a stochastic element (noise) in the motion and reduces the average lateral force, i.e. leads to less friction. In the following, we introduce thermal excitations in the Tomlinson model and cast its solution in the form of a set of rate equations that we solve numerically. We end this chapter by demonstrating these thermal effects in actual measurements of nanoscale friction on a graphite surface.

3.2 Modest thermal effects: the ‘thermal Tomlinson model’

As described above, the traditional Tomlinson model describes friction on a very simple level. It involves only two contributions to the total potential energy of the system, namely the energy stored in the cantilever spring and the tip-substrate interaction, and it provides a fully deterministic description of the atomic-scale

stick-slip motion of the tip. We now first consider the effect of modest thermal vibrations of the atoms in the tip and those in the substrate. We start with the tip in one of the local minima in the combined potential, sketched in Fig. 3.1. Like all degrees of freedom of the cantilever-tip-substrate system, the vibrational mode connecting the present tip configuration with the next potential energy minimum carries an average energy of $\frac{1}{2}k_B T$.

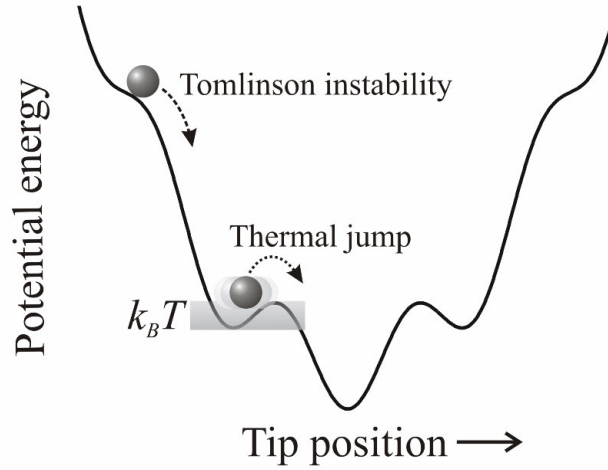


Fig. 3.1. Typical situation in the thermal Tomlinson model. When the remaining potential barrier to the next minimum is reduced to a height comparable to the thermal energy, thermal excitations make the tip jump. These early, ‘pre-critical’ jumps lower the friction force (average lateral force).

When the support is translated parallel to the surface, the potential barrier height U separating the local minimum in which the tip resides from the next minimum gradually decreases. When it is comparable to a few times the thermal energy $k_B T$, the tip has a high probability per unit of time to jump to the next potential minimum. In this way, at finite temperatures (and finite scan velocities) the tip almost never reaches the critical point at which the system is mechanically unstable and the tip is forced to slip (Fig. 3.1). The role of thermal activation manifests itself in any time dependent experiment on atomic friction. The simplest example is the velocity dependence. McClelland and coworkers were the first who examined this in atomic friction using molecular dynamics simulations [5]. They investigated the rupture of molecular bonds and the resulting stick-slip motion of an AFM tip on polymers and modeled it on the basis of thermally activated motion

of the tip between surface potential wells. Using straightforward transition-state theory, they introduced an attempt frequency r_0 and a Boltzmann factor to predict the rate of successful, forward jumps between neighboring potential wells in order to compute the flow of probability from one potential well to the next [6,7]:

$$\frac{dP(t)}{dt} = r_0 P(t) \exp\left(-\Delta U^+(t) / k_B T\right) \quad (3.1)$$

Here, $P(t)$ is the probability of finding the tip in a particular potential well and ΔU^+ is the height of the potential barrier in the forward direction. The main assumption here is that the tip can perform a pre-critical jump to the next potential well, but the possibility of a reverse jump is completely neglected since the barrier height for such a reverse jump is much higher than the forward barrier. This simple picture predicts that one can vary the strength of the effect of thermal excitations on the sliding motion by varying either the temperature T , the amplitude U_0 of the corrugation of the tip-surface interaction potential, or the scan velocity V of the support. The dependence on T and on U_0 should be strong, while the dependence on V may be expected to show a weak, logarithmic-type character, in view of the exponential form of the Boltzmann factor [6,7].

3.3 Strong thermal effects: ‘thermolubricity’

An alternative and more general way to view the tip motion in the presence of thermal excitations and under the simultaneous influence of the spring force exerted via the cantilever by the moving support, is as some a form of ‘driven diffusion’. Thermal excitations can assist the tip in jumping not only forward but also backward, i.e. against the direction in which the support moves (Fig. 3.2). As we shall see, the contribution of such reverse jumps depends strongly on T , U_0 and V and becomes significant when $k_B T / U_0$ is sufficiently high and/or V is sufficiently low.

When the time that the support takes to travel over one atomic distance is long enough that the tip makes several spontaneous forward and reverse jumps in that time, the required bias to make the tip follow the slow support motion, i.e. to make the frequency of forward jumps slightly higher than that of reverse jumps, is

very small; in other words the friction force becomes extremely low. For this situation we introduce the new term *thermolubricity*.

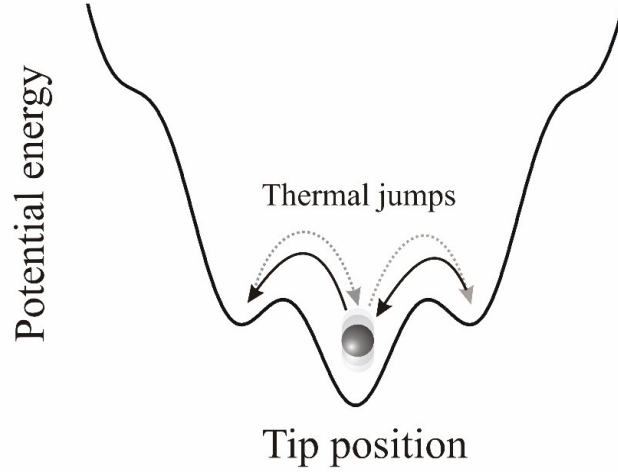


Fig. 3.2. When the barriers are low enough with respect to the thermal energy and the velocity is low enough, the tip shows not only forward jumps but also a significant frequency of backward jumps and can be considered to perform ‘driven diffusion’.

3.3a Formulation of the model: The Tomlinson parameter and the time-scales

As discussed in Section 1.2, the Tomlinson model contains two potential energies – the elastic energy of the cantilever and the potential energy of the tip-surface interaction – given by Eqn 1.1:

$$U(X, x) = \frac{U_0}{2} \left(1 - \cos\left(\frac{2\pi x}{a}\right) \right) + \frac{1}{2} k (X - x)^2 \quad (\text{Eqn 1.1})$$

Stick-slip motion of the tip is a result of the competition between the potential barrier height and the elastic energy of the cantilever. It is customary to introduce a dimensionless parameter γ , which we will refer to as the relative corrugation or the Tomlinson parameter.

$$\gamma = 2\pi^2 \frac{U_0}{ka^2} \quad (3.2)$$

When $\gamma > 1$ the total potential energy of equation 1.1 exhibits several local minima, which leads to the familiar stick-slip instabilities in the motion of the tip. When $\gamma \leq 1$, i.e. when the cantilever is sufficiently stiff with respect to the surface

corrugation, there is only a single stable minimum in the total potential energy for every support position. Under these conditions, the cantilever distortions (compression and elongation) still follow the sinusoidal atomic corrugation of the surface, but the motion is smooth and exhibits no stick-slip instabilities. Within the Tomlinson model, the net friction force is zero in this case, the backward lateral forces experienced while climbing the potential hills being precisely equal to the forward forces felt half a period later while descending into the valleys. In other words, the energy invested in the first half of the period is returned to the system during the second half, as a result of which there is no energy dissipation. There are several ways to bring a sliding system into this regime. Socoliuc *et al.* have reduced the amplitude U_0 of the tip-surface potential by scanning their tip over an NaCl(100) surface at significant negative normal forces, i.e. while pulling against the Van der Waals attraction between tip and surface, until they found reversible sliding with ultra-low dissipation [8]. Dienwiebel *et al.* have measured the lateral forces between a graphite flake and a graphite surface. By rotating the two lattices with respect to each other, they were able to make U_0 very low, even for substantial (positive) normal forces, low enough to result in ultra-low dissipation [9]. In this case, where the slipperiness is caused by the incommensurability of the contacting lattices, we speak of *superlubricity*. We should realize that in the cases of ultra-low friction discussed here, the dissipation is not completely absent. Even when stick-slip instabilities are completely avoided, the system can lose energy irretrievably by processes such as electron-hole pair generation.

We return to the stick-slip case, where $\gamma > 1$. It is easy to derive the values of γ at which the number of local minima in the potential changes. For instance, if $1 < \gamma < 3\pi/2$, the total potential U will have either one or two wells, depending on the position X of the support. Generally, there will be n or $(n-1)$ wells when $(2n-3)\pi/2 < \gamma \leq (2n-1)\pi/2$.

At non-zero temperature the dynamics of the tip are to be taken into account. There are four basic timescales or frequencies involved in this problem: (1) the frequency with which the support scans over the atomic lattice V/a , where V is the velocity of the support and a is the lattice constant; (2) the frequency ν of rapid inherent motion of the tip in a potential well, which depends weakly on the tip position, $\nu = (2\pi)^{-1} M^{-1/2} (k + 2\pi^2 U_0 / a^2)^{1/2}$, with M the effective mass of the

cantilever-plus-tip; (3) the frequency of successful, thermally activated jumps between potential wells; and (4) the damping parameter η , which is the rate of relaxation of the energy and momentum of the tip-cantilever combination into the phonon bath and into other excitations of the substrate, tip or cantilever.

We assume the backward and forward r_i^\pm jump rates of the tip between neighboring potential wells to follow a simple Arrhenius law,

$$r_i^\pm = r_0 \exp\left(-\frac{U_i^\pm}{k_B T}\right), \quad (3.3)$$

where the subscript i refers to the specific potential well, U_i^\pm is the potential energy barrier for a forward jump to well $i+1$ (+) or for a reverse jump to well $i-1$ (-), and the pre-exponential factor r_0 is the attempt rate for such jumps. Since the potential profile within the Tomlinson model itself is changing continually due to the support motion, the potential barriers are functions of the support position, i.e. $U_i^\pm = U_i^\pm(X)$. We follow the simple form of transition state theory and equate the pre-exponential factor r_0 of Eqn 3.3 to the vibrational frequency ν .

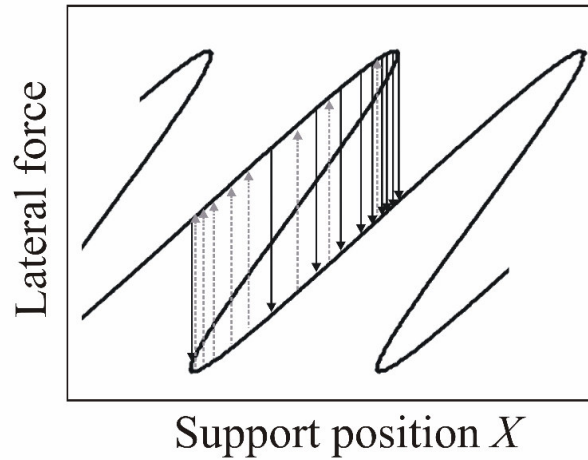


Fig. 3.3. Variation of the lateral force with the support position X (solutions of Eqn. 1.1). The exponentially varying probabilities of thermally assisted jumps are indicated here via the density of solid arrows (forward jumps) and dashed arrows (backward jumps).

Equation 3.3 explicitly shows us that when the support moves forward and reduces the forward energy barrier, the rate of jumps to the next local energy minimum increases exponentially. This makes the pre-critical jumps almost inevitable while jumps from deep potential wells can be rather infrequent. This idea is illustrated in Fig. 3.3, where the jump rate is shown to increase exponentially as the system approaches the critical points.

3.3b The Fokker-Planck approach

The interaction of the tip with the thermal excitations of the system introduces elements of nonequilibrium statistical mechanics in this problem. While individual tip trajectories can be calculated using Langevin dynamics, the average behavior of the system can be described much more efficiently using a kinetic equation, for instance, of the Fokker-Planck type [10]. This allows us to obtain the probability densities $p(x, t)$ of finding the tip at a given time t at a given position x . Evstigneev and Reimann have attempted to describe the thermal activation of the tip through a Fokker-Planck approach, molding it in a Brownian framework [11–14]. The most dominant timescales at play in the measurements are the long timescale of the slow scan motion and the short timescale of the rapid motion of the tip within the potential wells. In view of the large difference between these timescales, we can average over the faster class of processes and replace the probability density $p(x, t)$ by a discrete set of probabilities $p_i(t)$ of finding the tip in well i at time t . Assuming that the transitions between neighboring wells follow the Arrhenius law described by Eqn 3.3, we formulate the rate of change of the probability $p_i(t)$ to find the tip in well i in terms of the jump rates between well i and the two neighboring wells, $(i-1)$ and $(i+1)$. In this way, the kinetic equation is reduced to a system of continuity equations for $p_i(t)$ in discrete space of the form

$$V \frac{dp_i}{dX} = \frac{dp_i}{dt} = -(r_i^+ + r_i^-) p_i + r_{i-1}^+ p_{i-1} + r_{i+1}^- p_{i+1} \quad (3.4)$$

Again, V is the scan velocity, with which the support moves over the surface; p_i , p_{i-1} and p_{i+1} are the probabilities of finding the tip in wells i , $(i-1)$ and $(i+1)$. The jump rates r_i^\pm are determined by Eqn 3.3, with the potential barriers

$U_i^\pm(X)$ for forward or backward jumps from well i depending on support position X . This set of differential equations naturally describes all regimes involving thermal activation of the tip. At low surface corrugations it incorporates the effects of multiple back and forth jumps between neighboring potential minima and at higher surface corrugations, it describes the flow of probability when the tip motion reduces to the familiar pre-critical jumps that take place when the remaining forward barrier U_i^+ is a few times the thermal energy $k_B T$ or lower. Fig. 3.3 is illustrative to understand the physical mechanism described by Eqn 3.4. The success rate of jumps of the tip to a neighboring potential well is determined by the attempt frequency of the tip and the energy barrier (Eqn 3.3). As the barrier in front of the tip decreases in time, the probability of a forward jump increases exponentially with that. When the barrier becomes as low as a few times the thermal energy, thermally activated jumps becomes ‘inevitable’. So, when the corrugation is high each term on the right-hand side of Eqn 3.4 is small because of the large barrier heights, except in the vicinity of a critical point, where one of the terms becomes large. In this case, the set of equations basically reduces to a single one, equivalent to Eqn 3.1.

The mean (ensemble averaged) lateral force as a function of the support position X can be found as

$$\bar{F}(X) = -k(\bar{x} - X). \quad (3.5)$$

The mean position of the tip, which appears in this expression, is given by

$$\bar{x} = \bar{x}(X) = \sum p_i(X) x_{\min}^{(i)}(X). \quad (3.6)$$

Here, the $x_{\min}^{(i)}$ represent the X -dependent positions of the wells (i.e. all local minima of the total potential).

Let us consider a simple situation in which at most two local minima exist in the total potential energy. Since the total probability is 1 and hence $p_1 + p_2 = 1$, the system of equations (3.4) is reduced to a unique equation for, say p_1 (the probability to be in the left well). Moreover, it is sufficient to find a solution only for the motion over one period of the surface potential, say $0 < X < a$. This is allowed by the fact that the coordinate of the critical points corresponding to the disappearance of the well of origin is smaller than a . Furthermore, nontrivial behavior takes place only in the interval between the critical points X' , where a new well appears, and X'' , at which the previous well disappears. Outside of this

interval either $p_1 = 1$ (for $0 < X < X'$) or $p_1 = 0$ (for $X'' < X < a$). In the interval of interest $X < X < X''$, the equation for p_1 takes the form:

$$V \frac{dp_1}{dX} = -r_1^+ p_1 + r_2^- (1 - p_1) , \quad (3.7)$$

with $r_1^+ = \nu \exp(-U_1/k_B T)$ and $r_2^- = \nu \exp(-U_2/k_B T)$. Here U_1 and U_2 are the barriers between the two minima as seen from the left and the right respectively. Note that, for the given potential of the form of Eqn 1.1, these quantities are known although cumbersome functions of X . The mean (ensemble averaged) lateral force as a function of X is given by

$$\bar{F} = -k \left[p_1 x_{\min}^{(1)} + (1 - p_1) x_{\min}^{(2)} - X \right] \quad (3.8)$$

3.4 Numerical evaluation of the rate equation: complete solutions

We can analyze Eqn 3.4 numerically without any simplifying approximation. To this end, we evaluate the probabilities at regular time intervals $\Delta t = \Delta X/V$, where ΔX is a small step in support position (typically 0.001 nm) and V is the constant scan velocity of the support. Assuming that at $X = 0$, the probability of finding the tip in the first well is unity, the probabilities are evaluated using the values of the potential barriers corresponding to each discrete position of the support position. For each interval ΔX , the change of probability Δp_i is estimated in each well, and the calculation is performed over a total of four lattice spacings or more, i.e. for X ranging from zero to $4a$ or higher. We check that the results over the last lattice spacing are identical to those one lattice spacing earlier, thus ensuring that the results are not affected by the initial condition that $p_1(X = 0) = 1$. For each of the support positions X_n ($n = 1, 2, \dots, N$) over the fourth lattice spacing we calculate the average tip position, using Eqn 3.6. With the average tip positions, the average lateral force at each position X_n or time X_n/V is then calculated using Eqn 3.5. By integrating the $\bar{F}(X_n)$ lateral force curve over the fourth lattice spacing, the friction force is obtained as the average lateral force,

$$F_{friction} = \frac{1}{N} \sum_{n=1}^N \bar{F}(X_n) \quad (3.9)$$

In Fig. 3.4 we have plotted examples of the evolving probabilities in each well, for two relative surface corrugations of $\gamma=8$ and $\gamma=3$, a cantilever spring constant of $k=1.8\text{N/m}$ and a support velocity of $V=30\text{nm/s}$. At the higher corrugation (Fig. 3.4a) either two or three wells are present in the potential, depending on the support position X . We see that the probability to find the tip in the initial potential well reduces smoothly to zero while the probability of finding it in the second well becomes unity. This high corrugation has situated the system in the regime of pre-critical jumps, in which backward jumps are very infrequent. At the lower relative corrugation (Fig. 3.4b) only one or two wells are present. The probability of finding the tip in the initial potential well remains well above zero all the way up to the point where the well disappears. Under these conditions the rate of backward jumps is in the same order of magnitude as the rate of forward jumps and the tip jumps back and forth many times per lattice spacing traveled by the support.

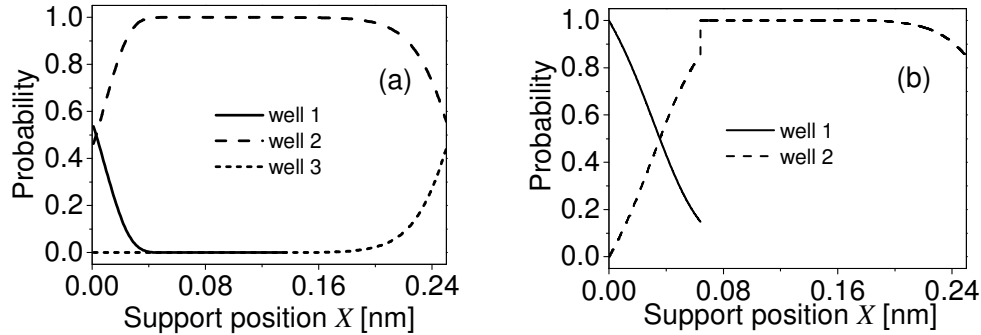


Fig. 3.4 Evolution of the probabilities to find the tip in the local wells of the total potential energy profile, calculated for a cantilever spring constant of 1.8 N/m, attempt frequency of 1.6 kHz and a support velocity of 30 nm/s. (a) At a high relative surface corrugation of $\gamma=8$ pre-critical jumps dominate. They make the probability in the initial well reduce smoothly to zero before the Tomlinson instability point is reached and the initial well disappears. Under these conditions the rate of backward jumps is negligible. (b) At a low relative surface corrugation of $\gamma=3$ forward and backward jumps are frequent, also when the system is not close to a critical point. The tip has a significant probability to be in the initial well even at the support position at which this well disappears.

Figure 3.5 combines the results of such calculations for a large number of relative corrugations γ , for the 0.246 nm lattice constant of the graphite basal plane, an effective cantilever spring constant of 1.8 N/m estimated from the friction experiments, a velocity of 30 nm/s and for three different values of the attempt frequency ν , in the form of a plot of the friction force versus γ .

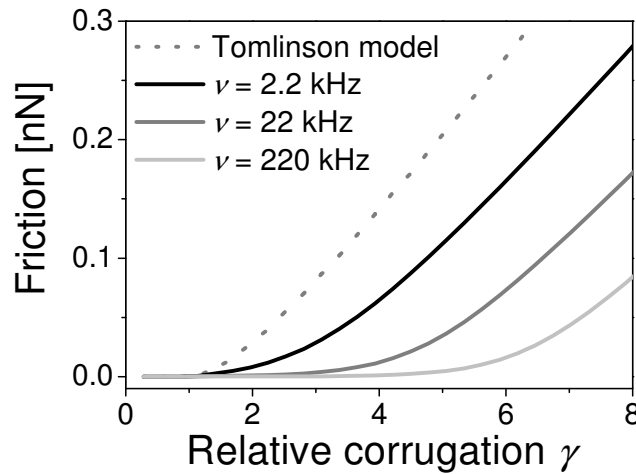


Fig. 3.5. Friction as a function of the relative corrugation γ , predicted by the Tomlinson model (dashed curve) and by the thermolubricity model (solid curves). The calculations were done using a lattice constant of 0.246 nm, a spring constant of 1.8 N/m and a support velocity of 30 nm/s, to compare with experimental data. These calculations illustrate the dramatic suppression of friction for different values of the attempt frequency of 2.2 kHz, 22 kHz and 220 kHz. Evidently, when the attempt frequency is high enough, friction can be very low even at relatively high corrugations.

The plot shows that the Tomlinson model predicts dissipationless sliding of the tip for relative corrugations $\gamma \leq 1$. In the case of weak thermal effects, i.e. when only pre-critical jumps occur, and the friction force develops a weak logarithmic velocity dependence, Eqn 3.1 predicts a modest lowering of the friction force with respect to the Tomlinson curve. The lower three curves in Fig. 3.5 show the numerical results for the case of strong thermal effects. In that case, significant lowering of the friction force is possible even at relative corrugations much higher than 1. These results show that temperature can act as a very efficient lubricant.

A counterintuitive aspect of the calculations in Fig. 3.5 is that the difference with the Tomlinson curve increases towards higher γ -values, whereas one might expect that at higher corrugations the effect of thermal excitations should become less important. This seeming contradiction is resolved by looking at the relative values, as we have done in Fig. 3.6. We refer to the reduction factor between the thermally lowered friction force and the friction force expected within the Tomlinson model as the ‘thermolubrication’ factor. As Fig. 3.6 shows, this factor can be significantly below unity for an intermediate range of γ -values where thermal effects manifest themselves very strongly via high frequencies of spontaneous forward and backward jumps, but at higher γ -values it necessarily approaches unity when only pre-critical jumps remain in a ever narrower range of X -positions before each critical point.

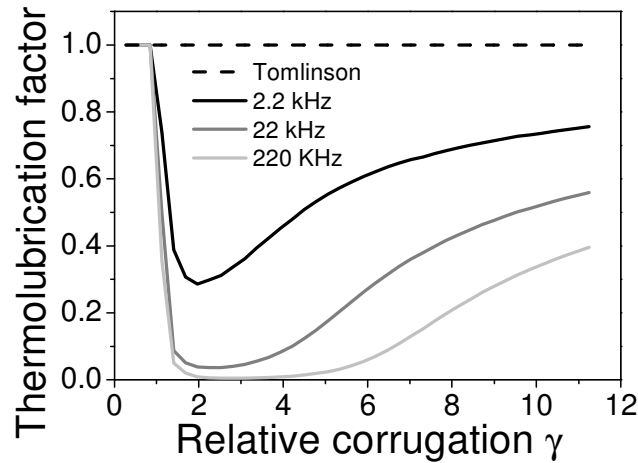


Fig. 3.6. Ratio of the friction values predicted by the thermolubricity model to corresponding values from the Tomlinson model, plotted against the relative corrugation γ . We refer to this ratio as the thermolubrication factor. The dashed, horizontal line is the Tomlinson model itself. The solid curves approach the Tomlinson line at high corrugations, where only pre-critical jumps occur.

3.5 Experiments: effects of surface corrugation on friction

An ideal check of thermolubrication at lower surface corrugation would be an experiment in which the surface corrugation experienced by the tip is controlled in the range of e.g. $1 < \gamma < 10$ (c.f. Fig. 3.6). Such an experiment would demonstrate

the manifestation of thermolubricity at lower relative corrugations and the effects of pre-critical jumps at higher relative corrugations. Recently, Schirmeisen *et al.* have demonstrated that a slight change in the surface corrugation leads to significant changes in the tip-jump statistics [15]. Two remarkable experiments reported recently have shown the reduction of friction by reducing the surface corrugation deliberately – one by varying the normal load exerted by the scanning tip on the surface and the other by varying the relative orientation of the lattices of two surfaces that were sliding over each other [8,9]. In the first case, the normal load was controlled so that the relative potential corrugation γ was varied over a wide range, and when the normal load was reduced sufficiently that $\gamma \leq 1$, the system slid with nearly zero dissipation. In the latter case, a tungsten tip was scanning over a graphite surface, but a graphite flake was strongly attached to the tip, so that the sliding actually took place between two graphite lattices. By rotating the substrate around the tip axis the degree of (in)-commensurability between the two lattices could be tuned, thus making the potential corrugation maximal for a narrow region of flake-substrate orientations where the two lattices were in registry and could only slide with high dissipation, and making it extremely low and leading to superlubricity for a wide range of non-matching orientations.

Here, we reanalyze the experimental data on superlubricity of Ref. [16], in search for thermal effects at a range of relative corrugations. The friction loops in this experiment clearly exhibit systematic changes in the motion of the tip, as sensed by the Tribometer. Figure 3.7 depicts typical friction loops observed under three different substrate-flake orientations, namely (a) in registry, (b) partially out of registry, and (c) even more out of registry. For reference, the variation of the friction force with the angle of rotation of the two lattices is reproduced in Fig. 3.7d. The two peaks in Fig. 3.7d are 60° apart and correspond to cases when the flake and graphite lattices are in registry. At most intermediate orientations, $\gamma \leq 1$ and the friction force is reduced to a near-zero value. For further details of this experiment we refer to Refs. [16,17].

The three force loops in Fig. 3.7 are all for γ -values above unity. As γ is reduced, the area enclosed by the friction loop shrinks, i.e. the friction force is reduced. We recognize that also the nature of the friction loop changes from that of well-defined, nearly regular stick-slip instabilities (a) to irregular stick-slip with superimposed, spontaneous backward and forward jumps (b), to completely

stochastic, drift-like motion. This change in character indicates that in this experiment the reduction of the friction force is due to a large part to spontaneous, thermal jumps.

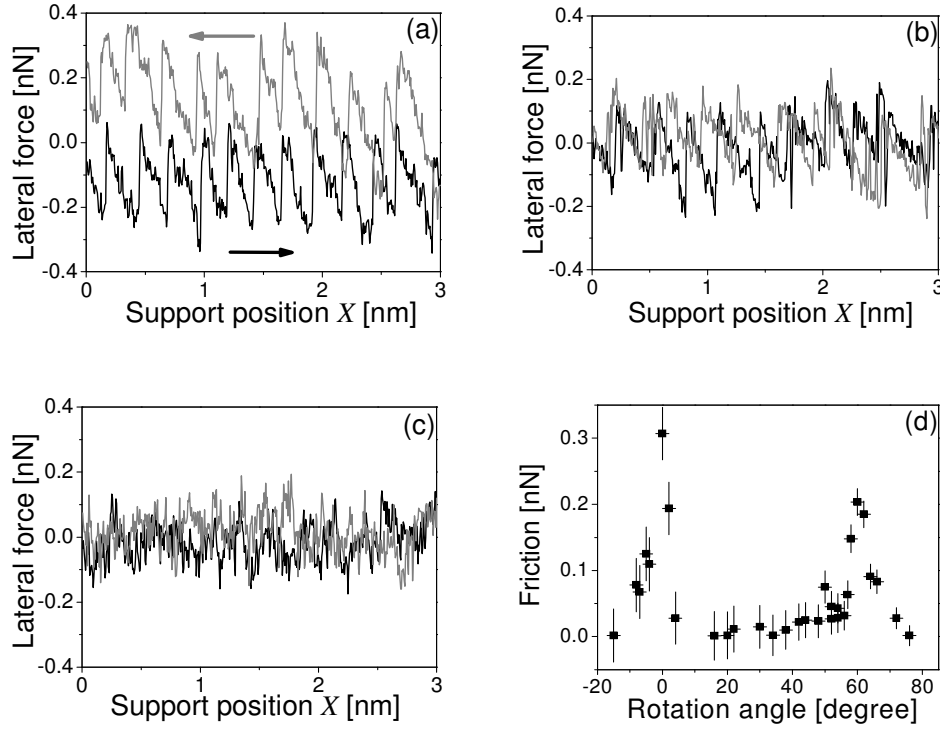


Fig. 3.7. Variation in stick-slip behavior between different rotation angles of a graphite flake with respect to a graphite substrate. In the force loops of panels (a-c), the black and grey curves are the forward and reverse scans. (a) At a relative orientation of 0° the lattices are in registry and dissipation is high. In this case we observe well-defined stick-slip motion. (b) At an intermediate orientation of 5° the system is partially out of registry and the stick-slip motion is irregular and we observe additional, spontaneous backward and forward jumps. (c) At 20° the lattices are more incommensurate and it is difficult to recognize any stick-slip character in the stochastic motion of the tip. The Tomlinson model allows us estimate the potential corrugations from the friction loops using Eqn 3.10, from which we obtain the following estimates: (a) $\gamma=5.25$, (b) $\gamma=3.33$ and (c) $\gamma=2.47$. Note that even in panel (c) the system is not superlubric, i.e. $\gamma>1$. For reference, panel (d) shows the orientation dependence of the friction force. Data taken from the experiment of Refs. [16,17]

For a full quantitative comparison between the experiment and the theory of the previous section, we have made a careful selection of force loops. This was necessary because the actual motion of the tip (flake) is essentially *two*-dimensional, whereas the theory has been restricted to a *one*-dimensional lattice. In the experiments of Refs. [16,17] a large part of the scans has been performed for a sliding direction parallel to the [0001] crystallographic axis of the graphite substrate. The fully two-dimensional sensitivity of the Tribolover allowed for measurements in which this alignment was maintained even when the tip and substrate were azimuthally rotated with respect to each other. In the two-dimensional force maps, in particular those at higher friction forces (closer to commensurate contact), we could easily recognize a periodic pattern of scan lines exhibiting a single period of 0.246 nm, corresponding to nearly one-dimensional trajectories of the flake over the two-dimensional substrate, and scan lines with two periods of 0.246 and 0.142 nm, corresponding to more zig-zag type trajectories. Since the lattice period plays a key role in our theory, we have selected for our quantitative analysis the one-dimensional type scan lines (force loops) with a single lattice period. We have verified that without this selection procedure the outcome of our analysis is not significantly different.

The relative corrugation γ can be estimated from the force variations in a friction loop by use of the Tomlinson model, which relates the maximum force F_{max} to the amplitude of the potential U_0 ,

$$F_{max} = \pi \frac{U_0}{a} \quad (3.10)$$

Combining this expression with Eqn 3.2, we can readily estimate the relative corrugation γ completely in terms of experimental parameters, namely the spring constant k , the lattice parameter a and the maximum lateral force F_{max} :

$$\gamma = 2\pi \frac{F_{max}}{ka} \quad (3.11)$$

One of the effects of thermal (and in particular pre-critical) jumps is to reduce the average maximum force with respect to the value predicted by Eqn 3.11. However, if we concentrate on *individual* force maxima, and select the highest ones, we can still obtain a relatively good, albeit slightly low estimate of F_{max} . In practice we have used the average of a few of the highest force peaks in a set of friction loops to estimate F_{max} for each set of conditions. This procedure is illustrated in Fig. 3.8.

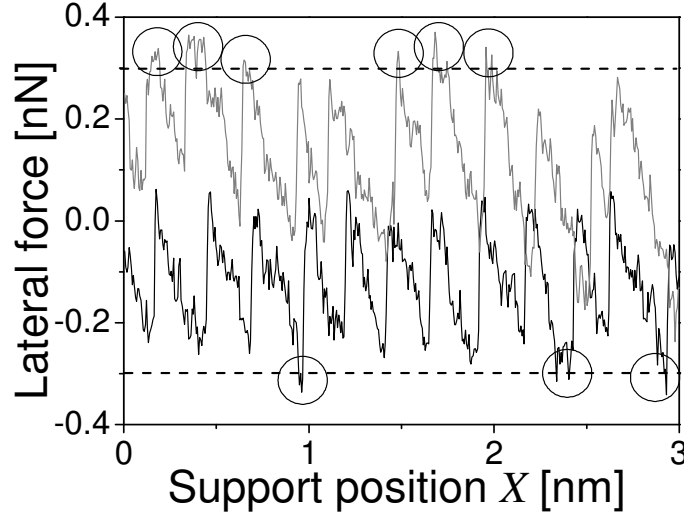


Fig. 3.8. Illustration of the selection of force maxima for the determination of γ . The average of the highest force maxima, encircled here, was used to obtain F_{max} from which γ was calculated using Eqn 3.11. The dashed lines are only for demonstrating the selection procedure of the force maxima in a selected loop.

There is an additional complication in obtaining γ from the experiment using Eqn 3.11, which involves the choice of the spring constant k . There are two seemingly natural choices that one can make here and both are wrong! First of all, one could use $k = k_T$, i.e. directly equate the spring constant in Eqn 3.11 to the calibrated spring constant of the Tribolover, which amounted to 5.75 N/m in the present experiment [16]. This value would be too high because the actual stiffness of the system is determined not only by the Tribolover but also by several other flexible elements in series with the Tribolover, as explained in Chapter 2. The second possibility would therefore be to use $k = k_{eff}$, i.e. to associate the spring constant in Eqn 3.11 with the full combination of the Tribolover spring constant and the contact stiffness (see Chapter 2 for the definition), which can be read off directly from the initial slope in every experimental force loop. This value would be too low because k_{eff} contains a dominating contribution $d^2U/dX^2 = (2\pi/a)^2 U_0$ from the tip-substrate interaction potential, which has a low amplitude U_0 that is different for every flake-substrate misalignment angle. In the limit of very low U_0

this even makes k_{eff} proportional to U_0 . Since F_{max} is proportional to U_0 (c.f. Eqn 3.10), k_{eff} should become proportional also to F_{max} in this regime. That this is indeed the case in the present set of measurements can be verified in Fig. 3.9, which shows a linear relation between k_{eff} and F_{max} .

The proper choice for the spring constant k in Eqn 3.11 is the combination k_s of the Tribolver spring constant k_T and the tip compliance k_{tip} .

$$\frac{1}{k_s} = \frac{1}{k_T} + \frac{1}{k_{tip}} \quad (3.12)$$

After all, γ is supposed to compare the strength of the measurement system (Tribolver plus other compliances that are not in the tip-substrate contact) with the strength of the tip-substrate interaction. As explained in Ref. [16] we can determine k_{tip} and k_s from the force loops, which for this experiment resulted in $k_{tip} = 2.7$ N/m and $k_s = 1.8$ N/m. The latter value has been used for k in Eqn 3.11 to obtain the γ values from all friction loops in the analysis in this chapter.

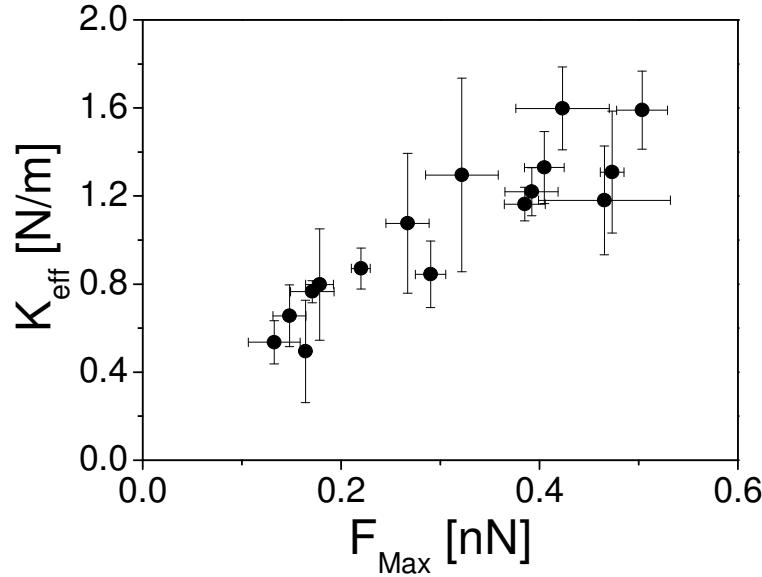


Fig. 3.9. Effective spring constant versus maximum force, obtained from force loops at a wide range of relative flake-substrate orientations. The linear relation indicates that the effective spring constant is strongly dominated by the contribution to the contact stiffness deriving from the weak tip-substrate interaction.

The result of our analysis for the selected ‘one-dimensional’ scan-lines is plotted in Fig. 3.10 as the friction force against the relative corrugation γ . We

immediately recognize that the experimental results are systematically below the curve calculated with the Tomlinson model for the same spring constant. This is a second, clear indication for the effect of thermal excitations in the motion of the tip. The thermal effects manifest themselves most strongly at lower relative corrugations, where they make friction nearly vanish well above $\gamma = 1$.

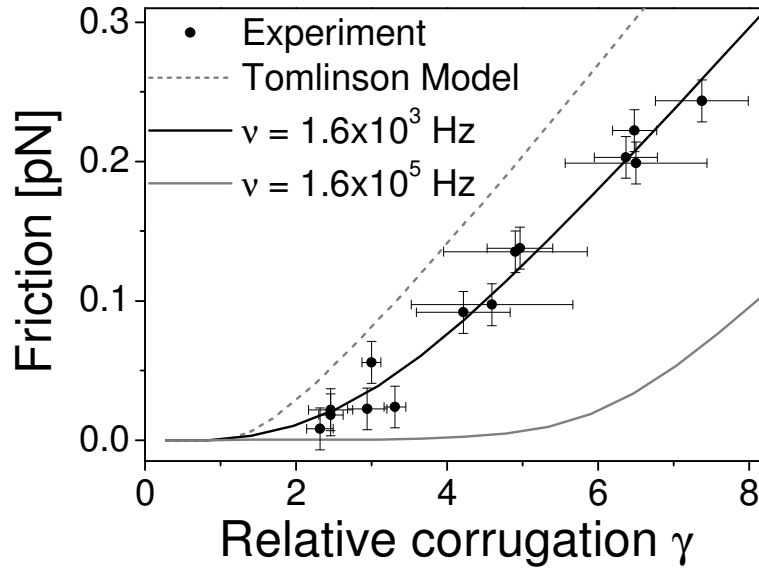


Fig. 3. 10. Friction against relative corrugation. The data points are obtained from the experiment. They are compared with the prediction from the Tomlinson model (dashed curve) and results for the thermolubricity model (solid curves). The parameters used in the calculations are obtained from the experiment ($k=1.8$ N/m, $a=0.246$ nm, $v=30$ nm/s). The thermolubricity model is shown here for two values of the attempt frequency. Excellent agreement is obtained with the experimental data for an attempt frequency of 1.6 kHz.

3.6 Discussion and Conclusions

The theoretical fit to the experimental data in Fig. 3.10 is rather convincing. The only adjustable parameter in this fit is the attempt frequency ν , for which we find a value of 1.6 kHz. This value is in the same order of magnitude as the resonance frequency of the cantilever, which suggests that the thermal vibrations of the entire cantilever dominate the thermolubrication effect.

There are several questions that remain open at this point. As mentioned above, the tip compliance estimated from these experiments (in the stick-slip regime) is 2.7 N/m. The presence of a finite tip compliance implies that the tip apex should behave as a second oscillator. The low value of 2.7 N/m, which is typical for the lateral compliance of tips in FFMs and AFMs, indicates that this second oscillator must have an extremely small (effective) mass. Since the tip compliance is in the same order of magnitude as the cantilever spring constant, we expect this second oscillator to have a much higher resonance frequency than 1.6 kHz but a thermal vibration amplitude that is comparable to that of the cantilever. These properties should make the second oscillator much more efficient in thermally assisting the sliding motion. At this point it is unclear why the much more rapid motion of the tip apex seems not to dominate the thermal effects.

A second open issue concerns the absence of strong thermal effects in the experimental data of Socoliuc *et al.* [8]. Their cantilever resonance frequency is almost two orders of magnitude higher than that of our Tribolover and their tip compliance is comparable to ours. Based on this, one would expect equally strong or stronger thermal effects in their experiment. Further work will be necessary to resolve these interesting issues.

Finally, there are three obvious parameters to vary, in order to systematically probe the effects of thermal excitation. In this chapter we have analyzed data in which the amplitude of the tip-surface potential was varied. In the next chapter we will concentrate on the dependence of the thermal effects on the support velocity. Future experiments to also address the temperature dependence will require modifications of our experimental setup.



3.7 References

1. L. Prandtl, *Zeitschr. f. angew. Math. u. Mech.* **8**, 85 (1928).
2. F. Dinelli, S.K. Biswas, G.A.D. Briggs, and O.V. Kolosov, *Appl. Phys. Lett.* **71**, 1177 (1997).
3. G.A. Tomlinson, *Phil. Mag. S.* **7**, 905 (1929).
4. C.M. Mate, G.M. McClelland, R. Erlandsson, S. Chiang, *Phys. Rev. Lett.* **59**, 1942 (1987).
5. J.N. Glosli, G.M. McClelland, *Phys. Rev. Lett.* **70**, 1960 (1993).
6. E. Gnecco, R. Bennewitz, T. Gyalog, Ch. Loppacher, M. Bammerlin, E. Meyer, H.-J. Güntherodt, *Phys. Rev. Lett.* **84**, 1172 (2000).
7. Y. Sang, M. Dube, and M. Grant, *Phys. Rev. Lett.* **87**, 174301 (2001).
8. A. Socoliuc, R. Bennewitz, E. Gnecco, E. Meyer, *Phys. Rev. Lett.* **92**, 134301(2004).
9. M. Dienwiebel, G.S. Verhoeven, N. Pradeep, J.W.M. Frenken, J.A. Heimberg, H.W. Zandbergen, *Phys. Rev. Lett.* **92**, 126101 (2004).
10. H. Risken, *The Fokker-Planck Equation*, Springer, Berlin, (1996).
11. M. Evstigneev, P. Reimann, *Phys. Rev. Lett.* **93**, 230802 (2004).
12. M. Evstigneev, P. Reimann, *Phys. Rev. B* **71**, 056119(2005).
13. M. Evstigneev, P. Reimann, *Europhys. Lett.* **67**, 907 (2004).
14. P. Reimann, M. Evstigneev, *New Journal of Physics* **7**, 25 (2005).
15. A. Schirmeisen, L. Jansen, H. Fuschs, *Phys. Rev. B* **71**, 245403 (2005).
16. M. Dienwiebel, N. Pradeep, G.S. Verhoeven, H.W. Zandbergen, J.W.M. Frenken, *Surf. Sci.* **576**, 197 (2005).
17. M. Dienwiebel, PhD Thesis: *Atomic-scale friction and Superlubricity studied using High-resolution friction force microscopy*, Leiden University, 2003.

Chapter 4

Thermolubricity and velocity dependence of atomic friction.

In this chapter we concentrate on the velocity dependence of atomic-scale friction, which we approach both theoretically and experimentally. Our numerical calculations show that a one-dimensional version of the thermolubricity model introduced in Chapter 3 fits the experimental data of friction of a tungsten tip on a graphite surface at each scan velocity with a different attempt frequency. We also investigate a two-dimensional version of our model, which explicitly includes the two-dimensional nature of the motion of the tip over the corrugated surface, taking into account the minimum-energy paths. Interestingly, we find that this two-dimensional aspect strongly reduces friction at low velocities, enabling our model to fit our data reasonably well at all velocities with a single attempt frequency.

4.1 Introduction

In this chapter we explore the velocity dependence of friction as an ideal experiment to probe the dissipation mechanisms and time-scales associated with it. In the original Amontons-Coulomb description, the friction force does not depend on velocity. Nevertheless, pronounced effects of velocity on dynamic friction and of the waiting time on static friction are known. Here we will see that velocity dependent behavior on the nanoscale can be quite different from that of macroscopic contacts.

The velocity dependence of atomic-scale friction can have several origins, of which the most important are:

1. thermal activation of the nano-asperity or the tip in the substrate atomic potential wells [1]
2. dynamical formation and rupture of molecular bonds [2].
3. plastic and elastic deformations of the tip and surfaces [3]
4. presence of ‘third particles’ or impurity atoms between the sliding surfaces [4]
5. presence of a lubricant and multitudes of different physical phenomena occurring in thin liquid films between the sliding surfaces [5]
6. formation, growth and rupture of capillary bridges between the sliding asperities [6]

There are extensive discussions in the literature on each of these mechanisms, but we are still far from a complete understanding. In practice, it is difficult to set up experiments that concentrate on just a single of these mechanisms and exclude the others. In addition, some of these mechanisms are already quite complex in themselves. For instance, simulations demonstrate that the velocity dependence of friction between two periodic surfaces changes drastically when a single impurity atom is introduced between them, which modifies the interaction potentials of the sliding surfaces [7].

Here we will focus only on the first aspect, the velocity dependence introduced in the atomic friction force by thermal excitations of the tip resulting in the velocity dependence of atomic friction. We will encounter a variety of velocity regimes in which the thermal effects have a different signature.

4.2 Thermal activation models and the velocity dependence of atomic friction

As discussed in the previous chapters, the Tomlinson model reproduces many of the non-thermal aspects of atomic-scale friction. It is often referred to as a zero-temperature model, in the sense that the thermal excitations of the tip in the surface potential wells are completely neglected. The tip is tacitly assumed to dissipate all its energy in each slip event, as a critically damped or overdamped oscillator, converting it into elemental excitations such as phonons and electron-hole pairs. In a strict quantum mechanical sense, the Tomlinson model would not be possible at zero temperature, since the dissipation of energy via the excitation of phonons would only be possible at non-zero temperatures when sliding at velocities below the phonon velocity. In fact, the sliding at velocities below this threshold should actually proceed with zero dissipation at zero temperature [8].

As discussed in Chapter 3, one can introduce weak thermal effects in the Tomlinson model by giving the tip the possibility to move to the next potential energy minimum before the one in which it resides has disappeared completely. Using the rate equation given by Eqn 3.1, one can cast the probability for such pre-critical jumps into an Arrhenius form. This activated process leads to a logarithmic type of dependence of the friction force on the sliding velocity. This is a comparatively weak regime of thermal activation, because the thermal effects become noticeable only when the potential barrier is reduced to a few times the thermal energy [9]. If the energy barrier is assumed to vanish linearly with the buildup of lateral force one obtains the relation

$$F_{fric} \propto \ln V \quad (4.1)$$

Very close to the critical point ($\Delta U^+ \sim 0$) the approximation that the energy barrier ΔU^+ diminishes linearly with the lateral force is not valid. Sang *et al.* have proposed a model of thermal activation of the tip with a ramped creep, a potential that is ramped up continuously by the motion of the support [10]. Based on this they predict

$$F_{fric} \propto (\ln V)^{2/3} \quad (4.2)$$

Both predictions (Eqns 4.1 and 4.2) have been verified experimentally [11], although at higher velocities, the tip jump statistics indicates that Eqn 4.2 is the more accurate theory [12].

The applications of these simple logarithmic laws that govern nano-friction are diverse. For thermal activation observed in many systems, varying from atomically smooth surfaces to microscopically rough interfaces, this is an important velocity regime. There are also other scenarios that result in a logarithmic velocity dependence of friction. For instance, a logarithmic decrease of friction with velocity can result from the competition between the timescale of the scanning and the nucleation timescale of capillary condensation between the tip and the surface [6]. A logarithmic velocity dependence can also be due to the long relaxation timescales of confined lubricants under shear [13], or the intrinsic relaxation timescales of the sliding materials themselves [14]. A system undergoes stick-slip instabilities under an applied external lateral force when the motion requires overcoming activation barriers and when the motion is dissipative. Generally, at non-zero temperature these activated processes will lead to some type of logarithmic velocity dependence. Also in the rather different context of shearing ordered layers of organic molecules on a surface, where thermal activation acts against the entropy-driven ordering of the molecules, a logarithmic velocity dependence is observed [15].

The predictions of Eqn 4.1 and 4.2 are neither novel, nor surprising. In many fields that are not even explicitly connected to friction thermally activated jumps over spinodal barriers have been treated with the same results. For instance in the case of pinning and transport of charge density waves [16], the result of *thermally activated premature depinning* is a logarithmic velocity strengthening of friction. On the macroscopic scale of multicontact interfaces, the state and rate dependent friction (SRF) model of Rice and Ruina [17] states that the dynamic (kinetic) friction coefficient μ depends on two parameters – the sliding velocity V and a time-dependent state variable ϕ , which represent the ageing of the multicontact interface,

$$\mu(V, \phi) = \mu_0 + B \ln \left(\frac{\phi}{\phi_0} \right) + A \ln \left(\frac{V}{V_0} \right) \quad (4.3)$$

which shows that thermal activation process and the consequent logarithmic velocity dependence may also be recognized in the behavior of ensembles of many contacts. Baumberger and colleagues have discussed the effect of ageing and thermal activation of microcontacts in detail, where they found that at higher velocities, the slope at the spinodal limit will result in a $[\ln(V/V_0)]^{2/3}$ variation of the

frictional forces [18]. Baumberger *et al.* have also demonstrated the two logarithmic laws in experiments on macroscopic sliding bodies with contacts of e.g. paper or PMMA. The first prediction of a logarithmic velocity dependence in atomic-scale friction is due to Glosli and McClelland who performed molecular dynamics simulations of organic layers [19]. Fig. 4.1 shows their result, comparing both MD simulation data and a thermal activation model. Their prediction has been verified experimentally in solid Langmuir films [20].

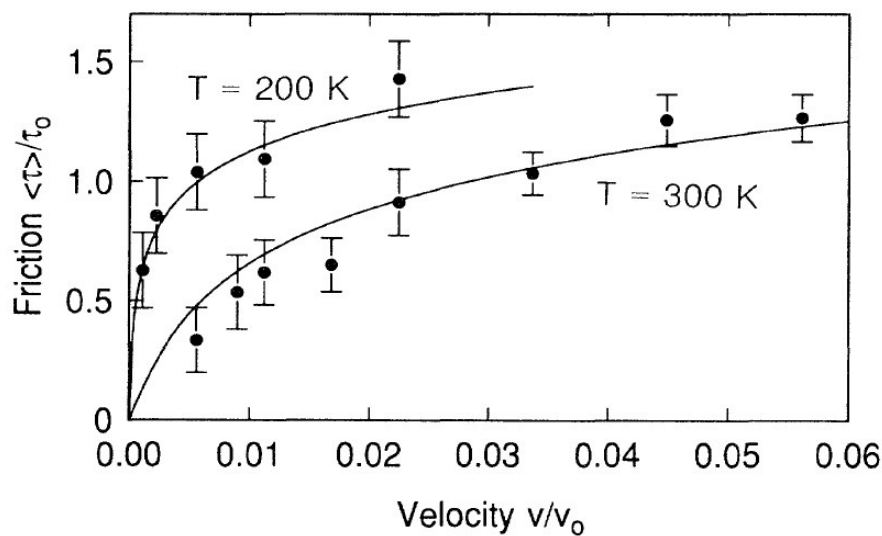


Fig. 4.1. Velocity dependence of friction obtained by molecular dynamics simulations on the friction between two ordered layers of alkane chains by Glosli and McClelland [19]. The solid curves show the thermal activation model, which predicts a logarithmic velocity dependence of friction.

4.3 Fokker-Planck approach and velocity dependence of friction

As we discussed in the previous chapter, thermal activation can make the tip overcome energy barriers even when these are much higher than the thermal energy. This activated process can be formulated in terms of the Fokker-Planck equation [21] which has become a standard approach in this field. Dudko *et al.* proposed an elegant treatment of the thermal activation of the tip, generalizing the Tomlinson model by adding a noise term [22]. Their model takes into account the irregular motion of the tip, as the temperature increases. Although this model only included the effect of forward jumps, they argued that the inclusion of backward

jumps would lead to a further reduction of friction at low velocities, when the frequency of such jumps would be substantial. Through this approach, Dudko and co-authors conclude that at lower velocities, atomic-friction has a weak logarithmic dependence on the scanning velocity due to thermal fluctuations. At higher velocities, viscous drag dominates and it acts as the major source of dissipation. The stick-slip regime is the highest velocity regime where thermal effects are manifest and temperature acts as a *lubricant*. At velocities comparable to the phonon velocity of the material, elastic deformations of the tip are so essential that the tip slides smoothly over the surface. Recently, Evstigneev and Reimann have analyzed the thermal activation of the tip, for a wide range of spring constants, describing the rates of multiple back and forth jumps of the tip [23]. The main message of these approaches is that thermal excitations can result in multiple jumps of the tip, both in the direction of the moving support and against that direction. This implies that the logarithmic velocity dependence of atomic friction, which is the result of only the forward jumps, should be restricted to a small velocity range. Combining all this information, we summarize the different friction regimes as follows:

At ultra-low velocities, typically of the order of a few nm/s or lower, thermal activation makes the tip perform multiple backward and forward jumps between neighboring potential wells, thus making friction dramatically low [1]. We will discuss this aspect in detail later in this chapter.

At slightly higher velocities of the order of a few tens of nm/s, the tip will perform predominantly pre-critical jumps. These give rise to a logarithmic velocity dependence of the friction force [9].

1. At velocities of the order of a few hundred nm/s, the ramped creep assumption is more appropriate and the velocity dependence is modified to $(\ln V)^{2/3}$. Over this velocity regime, the modified Tomlinson model holds and at higher velocities, friction is constant (at the value given by the traditional Tomlinson model) [24].

The torsional resonance frequency of a typical AFM cantilever is ~ 250 kHz. If the scan velocity (frequency with which lattice periods are traversed) is higher than the damping rate of the tip, the excess energy will not be dissipated completely between subsequent slip events. Under these conditions, friction may be either lowered [25] or increased [26], depending on the cantilever resonance frequency and the scan velocity. At these velocities, the (parametric) resonances can lead to

chaotic motion of the tip that does not reproduce the lattice period of the substrate [27].

2. At very high velocities, which are usually higher than the typical AFM scan speed, it is the *viscous drag* that causes dissipation (theory: Ref. [25], MD Simulation: Ref. [3,28]). These velocities are usually of the order of the phonon velocity of the substrate material. Up to this viscous drag regime, the friction force is equal to or less than the constant force predicted by the Tomlinson model. The addition of the viscous-drag damping term that represents the intrinsic energy dissipation of the sliding interface and is proportional to the scan velocity causes the friction force to increase linearly with velocity in the limit of high velocities.

Interestingly, all this information about the velocity dependence of friction reported by nanotribologists over the past five years has been familiar to the micro- and macro-tribology community already for a decade. For instance, nearly all these friction regimes have been investigated and explored by Caroli and Nozières in 1996 [29]. Fig. 4.2 shows a generic plot from their work in which the velocity dependence of friction is shown for an ensemble of microscopic contacts over the full range of velocities ranging from the zero-velocity limit to the limit of very high velocities (above the sound velocity).

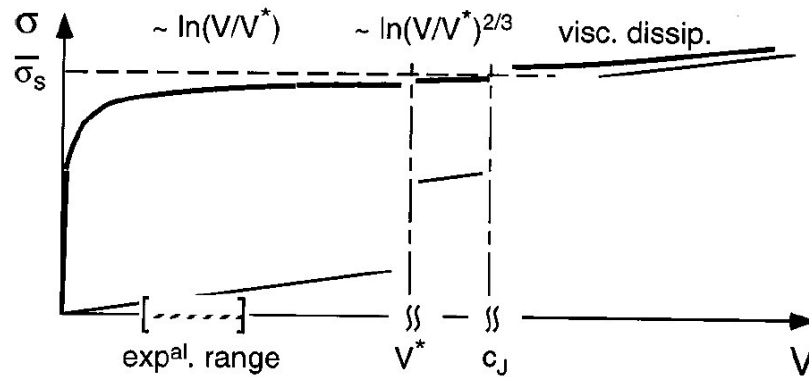


Fig. 4.2. Different regimes of friction depending on the sliding velocity for an ensemble of microcontacts, obtained by the SRF (state and rate dependent friction) model, reported by Baumberger et al. [18]. This forms a nearly complete summary of the regimes that should be expected for a single nanocontact. Between the velocity regimes with the $2/3^{\text{rd}}$ power law and with the linear increase (viscous regime) a single nanocontact should be expected to exhibit a range of velocities where friction varies with velocity due to washboard resonances and chaotic motion.

Most of the analyses mentioned in this section have explored in great deal either the logarithmic velocity dependence or velocity ranges above that. By contrast, little attention has been paid to the velocity regimes below the logarithmic velocity range. From the perspective of thermal effects, this low-velocity limit is the most interesting regime where thermal effects should be strongest. For this reason we concentrate on ultra-low velocities in this chapter.

4.4 Thermolubricity model and velocity dependence of friction

The problem concerning the inclusion of inertia effects in the Fokker-Plank approach is that the results rely very much on the effective mass chosen in the model [3,22]. One of the main parameters in a one-dimensional, one-spring model is the effective mass of the cantilever, which is given by $m^* = k_{eff} / (2\pi f)^2$, where f is the resonance frequency of cantilever when the tip is in contact with the surface. As we see later in this chapter, our experiments demonstrate clear deviations from the predictions of a simple one-spring model, indicating that the effective mass of the system can vary from the mass of a single atom at the tip apex to the (effective) mass of the entire cantilever, which is a mass range of many orders of magnitude. The advantage of the rate equations for probabilities, as given by Eqn 3.4, is that it excludes nontrivial terms like the effective mass from the model, but estimating probability distributions of the tip in the vicinity of its equilibrium position.

4.4a Definition of the basic parameters

We introduce two dimensionless parameters α and β that allow us to distinguish between several qualitatively different friction regimes.

$$\begin{aligned}\alpha &\equiv (V / a\nu) \sim (V / a\eta) \\ \beta &\equiv \left(\frac{V}{a\nu} \right) = \frac{V}{a\nu} \exp\left(\frac{U_0}{k_B T} \right) = \alpha \exp\left(\frac{U_0}{k_B T} \right)\end{aligned}\tag{4.4}$$

Here, α shows how fast or slow the scanning process is with respect to both the inherent motion of the tip in a surface potential well and the relaxation rate of the momentum to the thermal bath; β is a parameter that shows how fast or slow the scanning process is with respect to the rate of activated jumps of the tip between neighboring surface potential wells. Obviously, both parameters are correlated.

Stick-slip motion occurs in the velocity regime, where the support drags the tip to the next minimum before the tip jumps by itself due to thermal activation. In terms of the two parameters, this implies that the stick-slip regime corresponds to the case $\alpha \ll 1, \beta \gg 1$, where thermal activation is negligible and the tip *sticks* nearly everywhere in a potential well except in the vicinity of the critical point where it will make a pre-critical jump to the next well. There are two important timescales involved in this process: one is the slow time variation of the support motion that drags the tip to the next potential well and the other is the rapid motion of the tip apex within each potential well. The first inequality $\alpha \ll 1$ assures that the movement of the tip from the critical point to the neighboring well is much faster (actually on the order of ν^{-1}) than the slower motion of the support. So it is seen by the support as a fast *slip*. The excess energy released during the transition from the critical point to the bottom of the well is completely dissipated in the slip event (on a timescale of η^{-1}). This is the origin of the fact that the friction force in this regime is independent of the characteristic dissipation rate η . The slip starts in the vicinity, but, due to thermal excitations, just before the critical point, which leads to a logarithmic velocity dependence of the friction, as mentioned before.

Thermal activation of the tip manifests itself much more strongly when we reduce β , which can be accomplished by lowering the velocity, but, equivalently, also by increasing the temperature or reducing the amplitude of the potential. When $\beta \ll 1$ the scanning is slow with respect to the natural occurrence of thermally activated jumps between neighboring surface potential wells. In this regime, the tip can be found on average at a position \bar{x} that effectively ‘drifts’ with the support position X , while the average difference $X - \bar{x}$ determines the mean lateral force. Although the instantaneous lateral force exhibits rapid, irregular fluctuations with an amplitude in the order of the maximum possible tip-surface force, the average lateral force is significantly lower. We call this range of low velocities the *thermal drift* regime. In the intermediate situation, say at $\beta \sim 1$, the tip exhibits on average one random jump per lattice spacing traveled by the support. In this case, we expect to observe irregular or stochastic stick-slip motion.

4.4b Zero-limit approximation in β : the limiting case of zero velocity

Here we concentrate on the cases $\alpha \ll 1, \beta > 1$ and $\beta < 1$, which cover both the stick-slip and thermal drift regimes. The average behavior of the system can be described by an appropriate kinetic equation for the distribution function (probability density) to find the tip at a certain time at a certain position x . In the case $\alpha \ll 1$ under consideration, this complicated situation can be substantially simplified by the fact that, while being in a certain potential well, the motion of the tip both in physical space and in energy space (characterized by ν and η respectively) is fast with respect to the velocity of scanning.

We again consider the simple case, treated in Chapter 3, where only two potential energy wells exist. To zero limit of β , we may set the left hand side of the Eqn 3.7 to zero and find

$$p_1^{(0)} = \frac{r_2^-}{r_1^+ + r_2^-} \quad (4.5)$$

Physically, this expression, together with $p_2^{(0)} = 1 - p_1^{(0)}$, describes the equilibrium distribution of positions of the tip established in the situation when activated jumps between the wells have enough time to occur many times before a sizable displacement of the support takes place.

Since the ensemble averaged lateral force $\bar{F}^{(0)}(X)$ at position X is periodic with the lattice constant a , averaging over one lattice spacing gives us the mean value of the lateral force – the friction force – on a large timescale. An immediate result is that the friction force (in the zero-order approximation in β under consideration) is zero, i.e.

$$F_{fric}^{(0)} = \frac{1}{a} \int_0^a \bar{F}^{(0)} dX = 0 \quad (4.6)$$

Since $\beta \propto V$, the friction force in the limiting case of small velocity is completely given by its zero-order approximation in β . We conclude that

$$\lim_{v \rightarrow 0} F_{fric} = 0 \quad (4.7)$$

We see that the friction force at finite temperature should vanish in the zero-velocity limit, because of the thermally activated jumps of the tip between the surface potential wells. For any given surface corrugation and any nonzero

temperature, thermal jumps occur and, due to the thermal drift motion described here, friction will vanish in the limit of zero velocity.

In a sense, the result of Eqn 4.7 is trivial. In fact, speculations have been published that friction might vanish as the velocity goes to zero [22]. However, in many studies, this possibility has been ignored or overlooked. There is even a study, performed with the extended adiabatic approximation method, that suggested that whenever the thermal energy would be lower than the potential barrier, static friction would not vanish, even in the zero-velocity limit [30].

This result is important at least in two respects. First, a strong decrease in the friction force with decreasing velocity is expected when going down in velocity from the stick-slip regime to the deep thermal drift regime, where F_{fric} becomes small and finally vanishes when $V \rightarrow 0$. The overall behavior for any given relative corrugation can be obtained from a numerical solution of the corresponding system of equations (3.4).

Second, the role of thermally activated processes requires us to reconsider *static* friction. Static friction is the minimum force required to set an object-at-rest into motion along the surface. Within the classical Tomlinson model, this force is given by the maximum value of the lateral surface force, which is determined by the corrugation of the surface potential, $F_{static} = \pi U_0 / a$, and it is independent of whether the subsequent motion is dissipative ($\gamma > 1$, $F_{fric} = F_{fric}(U_0, \gamma) \neq 0$) or nondissipative ($\gamma < 1$, $F_{fric} = 0$). Apparently, the usual definition of static friction tacitly implies observation on a sufficiently short timescale that thermal effects can be ignored. On a larger timescale the object will exhibit thermally activated motion. In the absence of an external force, this is a random walk along the surface, while in the case of a slowly increasing bias, the walk is not random but has the character of biased diffusion. In this case, the system is not static and the definition of static friction loses its meaning. The static friction force could be understood as an essentially conditional quantity. It is given by the maximum surface force, provided that the external force increases sufficiently rapidly and it will be smaller for a more slowly ramped external force, as a result of the thermal jumps. Static friction will simply vanish if the external force is ramped up sufficiently slowly.

4.4c First-order approximation in β : friction in the thermal drift regime

In Eqn 3.4, if we introduce a first-order term $p_1^{(1)} \sim \beta$ in the probability $p_1 \equiv p_1^{(0)} + p_1^{(1)}$ for the tip to reside in the first well and neglect second-order terms in β , we get

$$p_1^{(1)} = -V[r_1^+ + r_2^-]^{-1} \frac{dp_1^{(0)}}{dX}. \quad (4.8)$$

Substituting this in Eqn 3.7 for the evolution of the probabilities in the two-well case, we obtain

$$p_1^{(1)} = -Vr_1^+r_2^- [r_1^+ + r_2^-]^{-3} \left[\frac{1}{k_B T} \frac{dU_2}{dX} - \frac{1}{k_B T} \frac{dU_1}{dX} + \frac{1}{v_1} \frac{dv_1}{dX} - \frac{1}{v_2} \frac{dv_2}{dX} \right]. \quad (4.9)$$

Note that $p_2^{(1)} = -p_1^{(1)}$. We have introduced the last two terms to take into account explicitly that the attempt frequencies v_1 and v_2 for forward and reverse jumps between wells 1 and 2 can be different from each other and dependent on support position X , for example by making them proportional to the square root of the curvature of the local potential. Equation 4.9 looks counterintuitive in the sense that the probability to find the tip in the first well increases both with increasing forward barrier U_1 and with increasing reverse barrier U_2 . Here, $p_1^{(1)}$ and $p_2^{(1)}$ describe the nonequilibrium correction to the distribution of tip positions, due to the fact that at nonzero scanning velocity thermally activated jumps do not have enough time to establish the true equilibrium distribution $[p_1^{(0)}(X), p_2^{(0)}(X)]$ at each support position X . As seen in Eqn 4.8, the effect is proportional to two factors; the first factor $V[r_1^+ + r_2^-]^{-1}$, shows how large is the systematic lack of time needed to realize the changes needed at every new support position X and the second factor, $\frac{dp_1^{(0)}}{dX}$, shows how $p_1^{(0)}$ changes with X , i.e. what changes in the distribution are to be realized by the jumps. If the system moves to the right ($V > 0$), these changes are due to the first well becoming more shallow and the second well becoming deeper. As seen from Eqn 4.9, all four contributions to $p_1^{(1)}$ are positive. Consequently, the overall effect is seen as a systematic delay of the transfer of the tip from the first to the second well. Clearly, on average, this will lead to an

increase in the ensemble-averaged lateral force. The friction force experienced by the tip at nonzero velocity will be nonzero.

Indeed, calculating the ensemble-averaged lateral force as in Eqn 3.8 with $p_1 = p_1^{(0)} + p_1^{(1)}$ using Eqns 3.8 and 4.9 we see that $\bar{F}(X)$ is larger than $\bar{F}^{(0)}(X)$ at every support position X (except for the intervals where they coincide due to the temporary absence of a second potential well). Averaging $\bar{F}(X)$ over one lattice spacing,

$$F_{fric} = \frac{1}{a} \int_0^a \bar{F} dX, \quad (4.10)$$

we obtain the friction force, which is nonzero at nonzero velocity.

Now we assume for simplicity that, except at very high temperatures, the effect of changes in the vibrational frequencies ν_1 and ν_2 with changing X can be neglected with respect to the more pronounced effect of changes in the potential barriers, i.e. we neglect the last two terms in Eqn. 4.9. This leads to the following approximation to the average lateral force.

$$F_{fric}|_{\beta \ll 1} \approx \frac{Cka}{4} \frac{U_0}{k_B T} \beta = \frac{CkV}{4\nu} \frac{U_0}{k_B T} \exp\left(\frac{U_0}{k_B T}\right) \quad (4.11)$$

Here, ν and U_0 are the characteristic values of the vibrational frequency and the barriers in the total potential, respectively. C is a dimensionless quantity representing the relative width of the region of the support positions for which there is more than one well in the total potential as a function of the tip position, and hence, thermally activated jumps can occur. It varies between $C = 0$ at $\gamma = 1$ and $C \sim 1$ at $\gamma = 3\pi/2$. The friction force vanishes at $\gamma \leq 1$, as a reminiscence of the classical Tomlinson model.

In the thermal drift regime, where $\beta \ll 1$, Eqn 4.11 gives the friction force linear in the scanning velocity, and it strongly – exponentially – depends on both the effective corrugation and the temperature. Even a small decrease in U or a small increase in T can lead to a substantial reduction in friction. By initiating motion of the tip, here, temperature acts as a *lubricant*.

In the derivations above, we assumed for simplicity that the rates of thermally activated jumps of the tip can be calculated in the framework of

transition state theory, so that the pre-exponential factors were taken simply to be the vibrational frequencies, $r_0 = \nu$. This traditional approximation tacitly assumes that the damping coefficient in the equation of motion is of the order of the vibrational frequency, $\eta \sim \nu$. A more general approach, valid for the case of both moderate and strong damping, allows estimating the jump rate pre-factor as $r_0 = \nu^2 / \eta$. For this case, after revision of the derivations given above, the result (4.11), with a slightly redefinition of the γ -dependent dimensionless factor C , becomes

$$F_{fric} \Big|_{\beta \ll 1} \approx C * \frac{U_0}{k_B T} \exp\left(\frac{U_0}{k_B T}\right) \eta M V, \quad (4.12)$$

with M the effective mass. This result is instructive in several respects. First, we have an apparent result that the friction force is proportional to the damping coefficient η . With increasing damping, at any surface corrugation, thermal jumps become rarer and their role as a lubricant therefore reduces, thus increasing friction towards the much higher value characteristic for stick-slip type of motion.

Second, we notice that $\eta M V$ is equal to the friction experienced by an object of mass M moving along a featureless surface with constant velocity V , as a result of dissipation to the thermal bath with rate η . Thus we expect friction to approach $F_{fric} = \eta M V$ realizing at very high V . The lower-velocity friction reflects the nontrivial physics behind the thermal drift motion of the tip. If the thermal jumps had enough time to establish the equilibrium distribution of the tip positions around the support position, the (mean) friction force would be close to $\eta M V$, as a result of the motion with mean velocity of the order of V . However, due to the lack of time at any nonzero velocity, the distribution is not equilibrium. A systematic delay of the tip with respect to the mean equilibrium position, as discussed above, manifests itself as an increase of friction. This effect is stronger when the jumps become less frequent, i.e. at larger U/T , as seen from Eqn 4.12. It is to be noted that the friction forces, although larger than $\eta M V$, remain significantly lower than the value ($\sim U_0/a \sim ka$) characteristic for the stick-slip motion, that takes place when thermal jumps can be neglected.

4.4d Numerical calculations

In Section 3.4 of the previous chapter, we discussed numerical calculations of the thermolubricity effect and we concentrated on a comparison between experiment and calculation in plots of friction versus relative corrugation γ . Here we use the same type of numerical calculations to predict the velocity dependence of friction at low velocities. The numerical results in Fig. 4.3 illustrate that the numerical results indeed follow the predictions of Eqns 4.7 and 4.11 that friction vanishes linearly in the limit of near-zero velocity. At higher velocities the numerical results show a regime where the friction force increases with the logarithmic of the velocity region. At even higher velocities, the friction force reaches a constant plateau at the value given by the Tomlinson model.

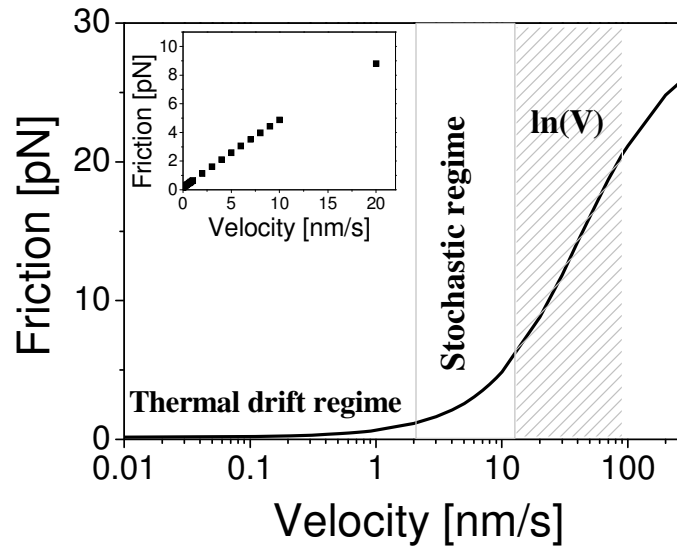


Fig. 4.3. Numerical calculation of the velocity dependence of friction, obtained using Eqn 3.4, at a relative corrugation $\gamma = 2$. The extreme reduction of friction due to multiple backward and forward jumps of the tip (thermal drift or thermolubric regime) can be easily discriminated from the regime of pre-critical jumps (logarithmic velocity dependence). The inset shows the linear velocity dependence of friction at ultra-low velocities. This is the regime where Eqns 4.7 and 4.11 are valid. The extent of this velocity range depends on the relative corrugation and the temperature.

4.5 Experiments: velocity dependence in various friction regimes

The primary experimental difficulty of most AFMs and FFMs in the measurement of friction at very low velocities is the combination of thermal drift and piezo creep

in the precise position of the tip with respect to the surface and in the zero-point setting of the force detection system (in our case the interferometers). In our setup, we employed special, home-built drift-compensators, integrated into our detection electronics, to compensate the variation of the four interferometer signals in case of drift. This has enabled us to measure spectacularly slow friction loops even at velocities down to 0.01 nm/s without any noticeable drift. All measurements were performed at a constant normal load of 3.7 nN and we scanned along the high-symmetry [1110] direction. In order to avoid graphite flakes getting attached to the tip while scanning, we used freshly etched tungsten tip on a high-quality HOPG, with grain-sizes of the order of millimeters, basically one single crystal as the sample. To minimize the effects of ‘third particles’, in particular water from the environment (see Chapter 6), we performed the experiments in a closed chamber, where the relative humidity was maintained below 1%, by continually flushing with dry nitrogen. The scan range was fixed at 3 nm and all force images are composed of 512×512 pixels.

Lateral force images at two different scan velocities of 30 nm/s and 7.5 nm/s are shown in Fig. 4.4. The atomic rows can be recognized vaguely, but that information is washed out to a large extent by the thermal noise, especially at the lower velocity.

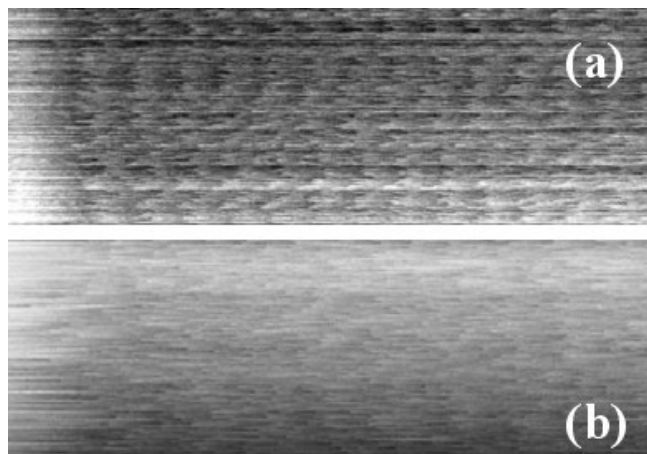


Fig. 4.4. Two forward lateral force images of graphite surface (3 nm scan-range) at two different velocities of (a) 30 nm/s and (b) 7.5 nm/s. The signature of parallel atomic row is clearly visible in the upper panel and rather difficult to distinguish in the lower panel.

The difference in the atomic contrast is also seen in the individual force loops at these two velocities, as is illustrated in Figs. 4.5 a and b, which further show that the stick-slip motion is much more irregular at the lower of these two velocities.

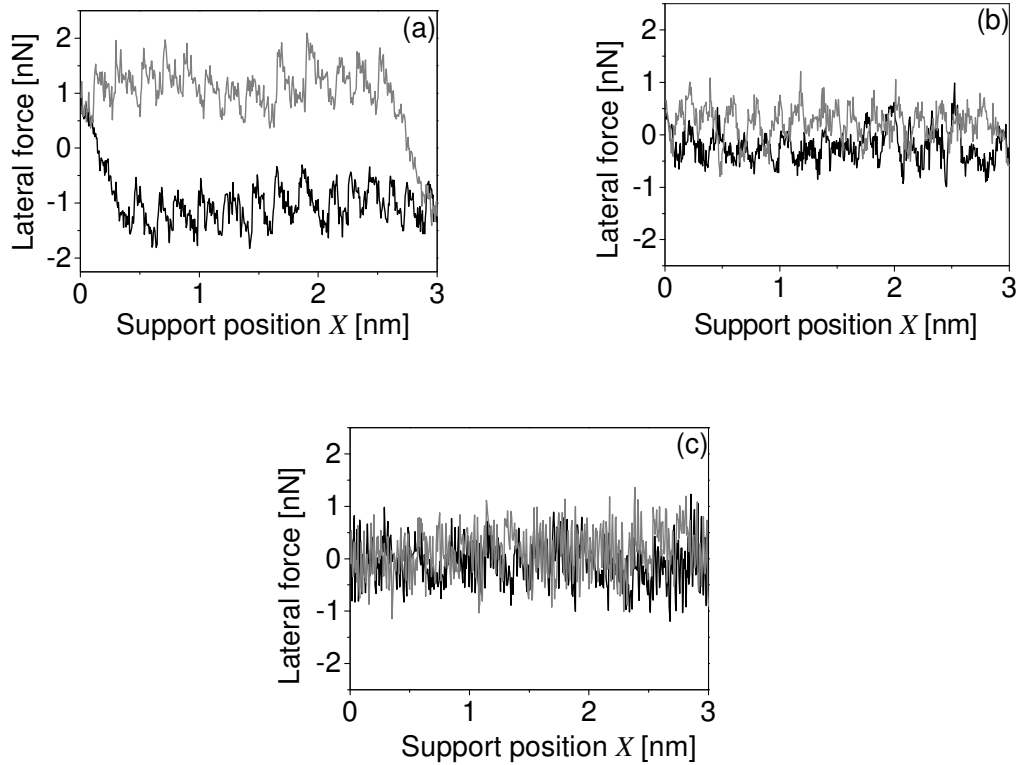


Fig 4.5. Three characteristic friction loops at velocities of (a) 30 nm/s, (b) 7.5 nm/s and (c) 0.6 nm/s. The area enclosed in the force loops reduces to almost zero as the velocity is reduced. At lower velocities, multiple peaks can be seen, corresponding to the multiple backward and forward jumps of the tip. This is a direct demonstration of the three regimes of (a) regular stick-slip, (b) stochastic stick-slip and (c) thermal drift motion.

Figure 4.5 also demonstrates that when we reduce the velocity, the area enclosed in the lateral force loops shrinks significantly. In other words, the average friction force is reduced to a near-zero value. At the lower velocity of 0.6 nm/s (Fig. 4.5 c) the character of the motion has changed completely. It is hard to recognize any atomic periodicity. The noise shows that the tip makes frequent forward and backward jumps. Together, Figs. 4.5 a, b and c illustrate three of the

friction regimes discussed above, namely regular stick-slip, stochastic stick-slip and thermal drift.

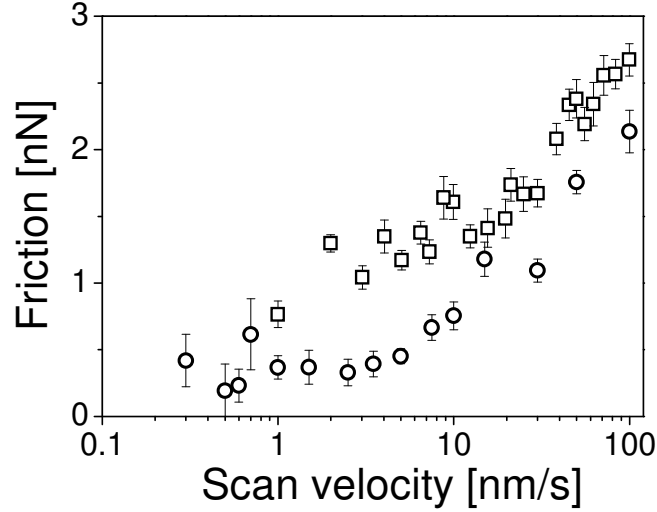


Fig. 4.6. Mean friction force as a function of velocity, measured at two different days (squares measured first, circles are data points under the same conditions, measured one month later). Each data point is the average of 512 scan-lines. At low velocities, the data clearly deviate from logarithmic behavior. Instead, friction is reduced nearly to zero: thermolubricity.

The friction force measured as a function of support velocity ranging from 0.1 nm/s to 100 nm/s is shown in Fig. 4.6, where the velocity is put on a logarithmic scale, for comparison with Eqn. 4.2 (Ref. [10,18]). The data deviates from this logarithmic law at lower velocities and the overall behavior is qualitatively very similar to our numerically calculated friction over a wider range of velocities (Fig. 4.3)

4.6 Comparison between the experimental results and the thermolubricity model

In this section, we confront our one-dimensional, one-spring thermolubricity model of Section 4.4 with the experimental results of Section 4.5. Our experimental results are in qualitative agreement with the velocity dependence predicted by the

model. In particular, we observe the three expected regimes of stick-slip, stochastic and thermal drift, as the velocity is lowered.

The seemingly trivial result in Eqn 4.7 predicts that a system that is thermally activated will move under the influence of an arbitrarily low driving force if we are willing to wait long enough. Reframing the same argument in terms of the static friction the system exhibits, the system will move because of the vanishing of the static friction at the zero velocity limits.

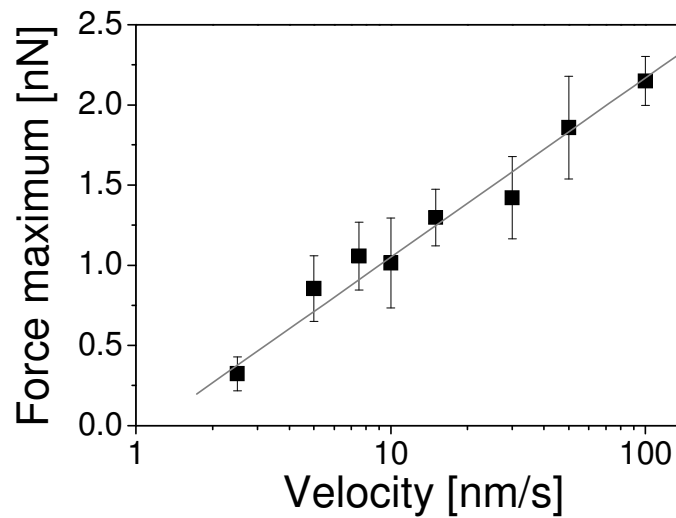


Fig. 4.7. Reduction of the force maxima with reducing velocity. The data show a distinct logarithmic dependence on the scan velocity. The grey line is the linear fit to the experimental data.

Fig. 4.7 shows the experimental result of how the force maxima reduces with velocity, which follows a logarithmic behavior, because of the Boltzmann factor in the exponent in the rate equation. This means that our theory applies to the behavior of force maxima as well.

4.6a Tip jump statistics at different scan velocities

As we discussed in the previous section, Fig. 4.5 can be viewed as a demonstration of multiple backward and forward jumps of the tip between neighboring potential wells. A natural way of quantifying this aspect is via the statistics of jump events. Experiments have been reported estimating the distributions of early jumps of the

tip at different scan velocities and surface corrugations under ultrahigh vacuum conditions, scanning with a commercial AFM on an HOPG surface [12].

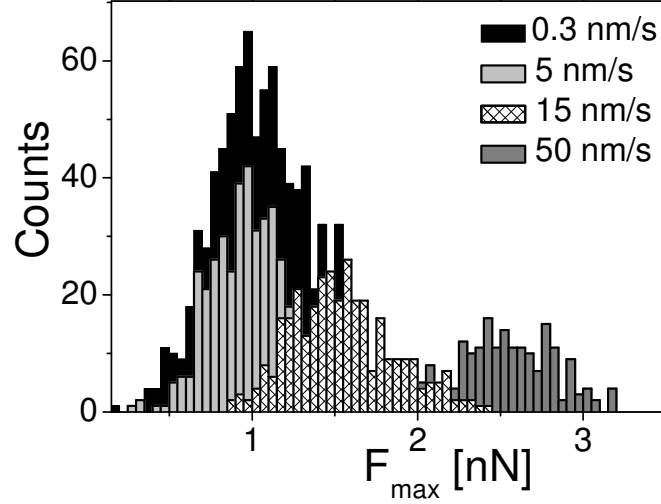


Fig 4.8. Distributions of the maximum lateral force F_{max} measured at four different scan velocities. The differences in area under the four distributions reflect the differences between the four velocities in total number of jumps observed per lattice spacing.

The number of multiple jumps per lattice spacing and the corresponding reduction of friction at ultra-low velocities can be read off directly from the distributions in Fig. 4.8 of the force maxima (F_{max}) in the slip/jump events. These distributions have been obtained at four different velocities. We see a clear trend that the average force maximum goes down when the velocity is lowered.

Since the distributions of the maximum lateral force in Fig. 4.8 have not been normalized, the area under each distribution is a measure for the number of forward jumps performed by the tip per lattice spacing traveled by the support. Clearly, the lower-velocity distributions show a much higher number of jumps per lattice spacing than the higher-velocity distributions. Figure 4.9 shows the velocity dependence of this number.

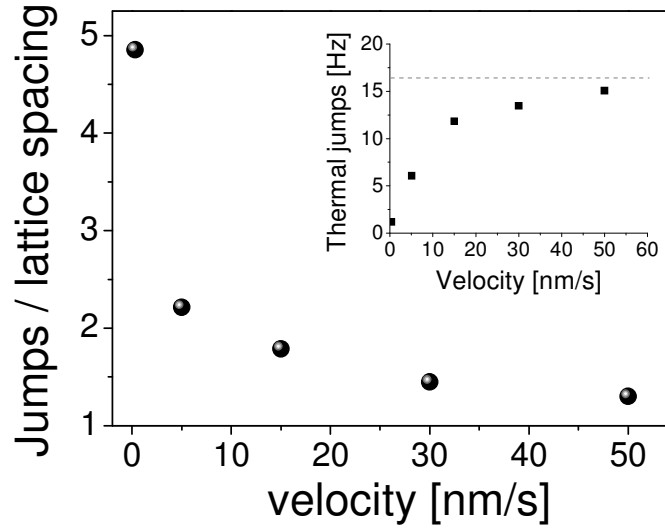


Fig. 4.9. Experimentally obtained number of forward jumps per lattice distance, as a function of velocity. At higher velocities, the loops exhibit only a single, pre-critical jump per lattice spacing, but as the velocity is reduced, we clearly observe additional, thermally activated jumps. The inset shows the same data but now expressed as the frequency of forward thermal jumps (see text) against velocity. As explained in the text, our measurement underestimates the true jump frequencies at the lower velocities and we estimate the thermal rate of forward jumps to be approximately 17Hz.

Since the tip has to perform at least one jump per lattice spacing, either a mechanical slip, or a pre-critical jump or a more distant, thermally activated jump, in order to keep up with the moving support, the number we get by subtracting 1 from the average number of jumps per lattice spacing value will be a measure for the frequency of non-mechanistic, thermally activated jumps. If we multiply this quantity by the velocity expressed in lattice spacings/sec we get the number of thermal jumps per second. The result of this exercise is shown in the inset of Fig. 4.9. The fact that the resulting frequency is not independent of the scan velocity is an artifact of our data acquisition system, which does not allow us to acquire an arbitrarily large number of pixels per scan line. At our extremely slow measurements, this actually limits the pixel frequency and thus leads to an under-sampling of the jumps. This means that the asymptotic value of ~ 16 Hz at high velocities in the inset of Fig. 4.9 can be taken as a reliable estimate of the true rate of thermally activated forward jumps under these conditions. If we use this number as the jump frequency r and calculate the potential barrier height U_0 from the

friction loops, we can readily estimate the exponential pre-factor r_0 , the most relevant parameter in our model.

4.6b Friction force versus relative corrugation

In this section we concentrate on the shape of the lateral force scans and, in particular, on the relation between the average lateral force, i.e. the *friction* force F_{fric} , and the maxima in the force F_{max} , which are equivalent to the relative corrugation γ . At constant temperature there are two ways to vary these two quantities, namely by varying the scan velocity V and by varying the potential corrugation U_0 . We first discuss how we can use measurements under a single set of conditions and still obtain information for a range of U_0 -values and then proceed to the relation between F_{fric} and F_{max} .

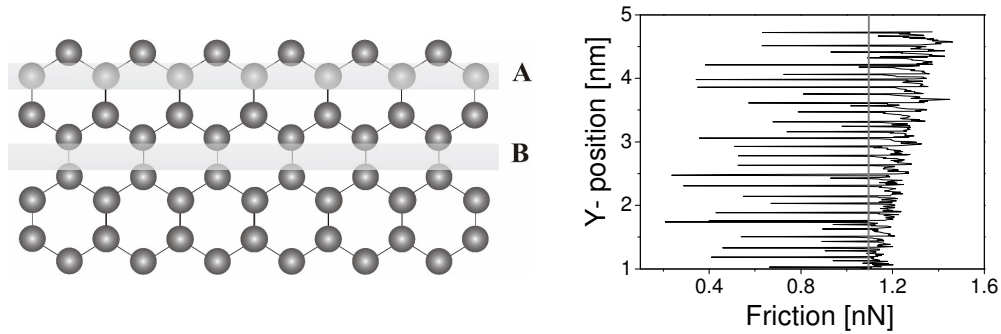


Fig. 4.10. Left: (A) and (B) indicate regions on the (graphite) lattice where the surface corrugations are rather different. The scan lines in region (B) are expected to exhibit lower friction than those in (A). Right: measured friction force as a function of the Y-coordinate of the scan line within a lateral-force image on graphite. At regular intervals, corresponding to the two distances between carbon atom rows along the Y-direction of 0.15 and 0.25 nm, the friction force shows a sharp minimum. The straight grey line indicates the average friction force of the entire lateral-force image.

The two-dimensional structure of the surface leads to distinct variations in the potential energy corrugation as a function of the precise location of the scan line on the surface. These variations are particularly strong when the scan direction is aligned with one of the crystallographic directions of the substrate. Such effects have been reported recently by Schirmeisen and colleagues on a graphite lattice [12]. This variation and the corresponding periodic variation in the observed stick-

slip period was already discussed briefly in Chapter 3, where we used only a selection of force loops, corresponding to single-period, one-dimensional type trajectories over the two-dimensional surface. The left panel of Fig. 4.10 indicates two bands of scan lines where we may expect the surface corrugations to be rather different.

The right panel of Fig. 4.10 demonstrates the measured variation of the friction force between scan lines at different Y positions. The friction force shows a distinct minimum at intervals of 0.15 nm and 0.25 nm. Similar variations can be recognized in the contrast in the lateral force image shown in Fig. 4.4a. Below, we use these position-dependent variations in the potential corrugation to obtain plots of the friction force over a range of relative corrugations γ .

Figure 4.11 shows a compilation of all measured friction forces F_{fric} against the relative corrugation γ , which was obtained from the force maxima F_{max} in the way, described in Chapter 3. The figure is similar to Fig. 3.10, but it spans a wider range of γ and F_{fric} -values. Interestingly, all data in this plot at first sight seem to collapse onto a single curve, even though the measured lateral force images used in this analysis have been obtained at widely different scan velocities from 0.1 to 100 nm/s and, as explained above, each force image already covers a substantial range of F_{max} and F_{fric} . Since F_{fric} is the average lateral force, we should, of course, expect that changes in the force maximum F_{max} are directly accompanied by changes in the frictional force F_{fric} . In the regime of stick-slip motion, we should even expect that the frictional force and the force maximum follow a nearly linear relation (Tomlinson model), with a derivative dF_{fric}/dF_{max} close to unity, since the difference between the two is close to a constant $\frac{1}{2}k_{eff}a$. When thermal excitations lead to pre-critical jumps, F_{max} and F_{fric} will be lowered by approximately the same amount, so that F_{max} and F_{fric} will still approximately satisfy the same nearly linear relation. These predictions are confirmed by Fig. 4.11 (note that γ is proportional to F_{max}). The slope of the linear part corresponds to $dF_{fric}/dF_{max} = 0.9$, which is indeed close to unity. The offset of this linear part of 0.5 nN (zero-crossing of the extrapolated straight line) is close to the naively expected $\frac{1}{2}k_{eff}a = 0.55$ nN in the present experiment. We see that the linear part covers the full range of conditions over which the system exhibits pre-critical jumps and F_{max} and F_{fric} follow a logarithmic velocity dependence (cf. Figs. 4.6 and 4.7). Interestingly, in the thermal

drift regime, where we already recognized that the tip performs multiple backward and forward jumps per lattice spacing traveled by the support, the plot of F_{fric} against γ deviates substantially from the linear relation. In a relatively narrow interval of γ -values, F_{fric} reduces to a near-zero value.

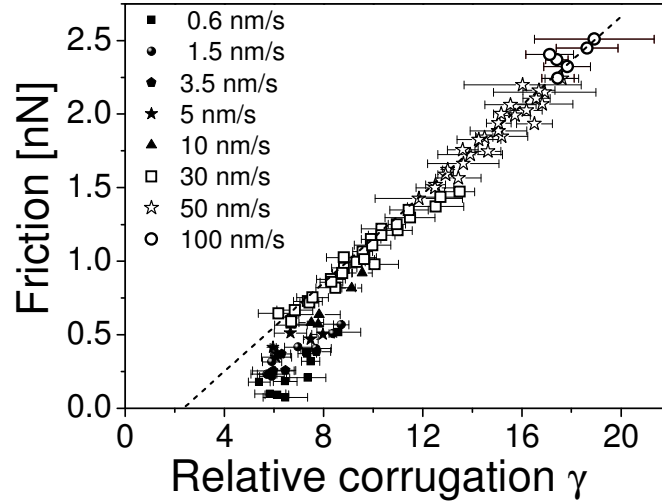


Fig.4.11. Friction versus relative corrugation, obtained from individual friction loops for a wide range of velocities. The observed, nearly linear relation is expected in the case of stick-slip motion or pre-critical jumps. The deviation from the linear relation, shown by all data measured at lower velocities, occurs under conditions corresponding to the thermal drift regime.

In Fig. 4.12 we show a blow-up of the lower-left part of Fig. 4.11. On this enlarged scale, we see that the lower part of the data is not really collapsing onto a single curve. In fact, at each velocity we obtain a separate curve, lower velocities corresponding to lower friction values. In Fig. 4.12 we compare our low-velocity data to theoretical predictions. Similar to Fig. 3.10, where we re-analyzed experimental data from [31], all data fall below the friction values predicted by the Tomlinson model. At the lowest velocity of 0.6 nm/s, friction nearly vanishes at $\gamma \sim 5$, which is 5 times higher than the γ -value at which friction would become zero in the Tomlinson model. Note that in our experiment this high relative corrugation of 5 corresponds to a barrier height U_0 of approximately 0.43 eV, which is more than 17 times the thermal energy at room temperature. The three solid curves are fits to the data for the three different velocities in Fig. 4.12, according to the

thermolubricity model, detailed in Chapter 3. Within the statistical scatter of the data, these curves provide an excellent description of the data.

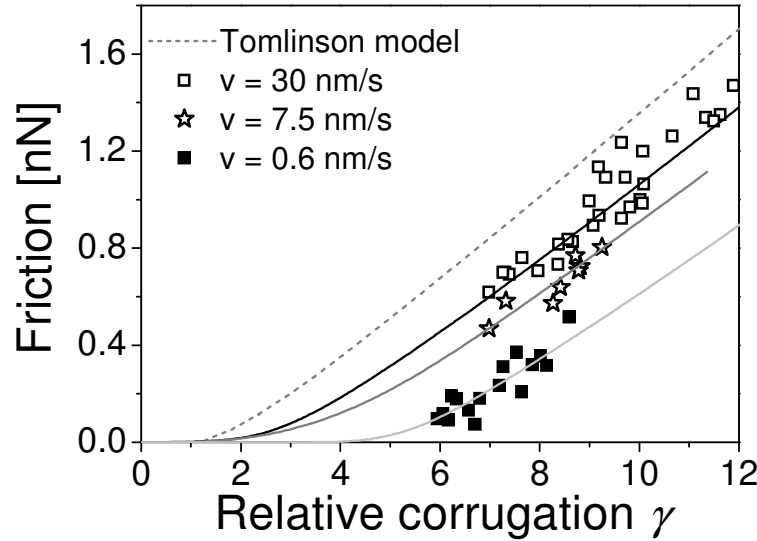


Fig. 4.12. Friction versus relative corrugation (enlarged view of lower-left part of Fig. 4.11) plotted together with theoretical curves. The symbols represent experimental data at 30 nm/s (squares), 7.5 nm/s (stars) and 0.6 nm/s (filled squares), which correspond to stick-slip, stochastic and thermal drift regimes of thermal activation. The dotted grey line is the friction according to the Tomlinson model and the three solid lines fitting the data at the three velocities are the results from numerical calculations using our thermolubricity model.

In each curve, there has been only a single free parameter, which was the pre-exponential factor, which we have associated in Chapter 3 with the attempt frequency ν . In order to obtain a good fit, we have been forced to use three very different values for ν at the three velocities, as is indicated in the figure, the highest ν -value being as much as three orders of magnitude above the resonance frequency of the Tribolover.

There are several potential reasons for the unexpected value of the pre-exponential factor and for its variation with the scan velocity. Within the employed transition-state theory for the driven diffusion of the tip and cantilever it seems natural to use the resonance frequency of the cantilever as the pre-exponential

factor. In a more sophisticated treatment, also entropic factors may be important, in particular in cases where the moving entity (contact area) is not a *single* atom but a small *ensemble* of atoms [32]. Although this aspect could be affecting the value of ν , it would not explain the velocity dependence of ν . We have considered several other aspects and will concentrate in the next section specifically on the role of dimensionality, the model having been one-dimensional and the data having been acquired on a two-dimensional surface.

4.7 Role of dimensionality in thermolubricity

The theoretical model we have discussed so far has an obvious inadequacy in that it has framed the problem in a single dimension. In reality, the tip moves over a two-dimensional surface and has the freedom to approach neighboring potential wells not just via a single trajectory but, instead, a variety of two-dimensional walks over the surface. This increases the complexity of the problem tremendously, because the tip may for example choose to move between two potential energy minima via a lower-energy, but non-trivial (e.g. non-straight) trajectory or it may for instance take advantage of the existence of a large number of slightly-higher-energy trajectories. We naturally end up with the picture of driven, two-dimensional Brownian type motion of the tip in the 2D potential energy landscape.

In a two-dimensional Tomlinson picture, the tip perceives local potential minima around it that may be more easily accessed (lower energy barrier) than the next potential minimum strictly along the direction of the support motion. We have performed computer simulations of tip trajectories in two dimensions, which show that at low velocities, instead of overcoming the potential barrier in front of it, the tip may indeed prefer to jump sideways to a temporarily more favorable, local minimum, before jumping to the next minimum along the direction of the support motion. Figure 4.13 shows a two-dimensional total potential profile for tip motion on the HOPG lattice, sensed by a cantilever of spring constant 0.5 N/m in the case of $U_0 = 0.5\text{eV}$. Two trajectories with different energy barriers are indicated in the grey-scale representation of this potential.

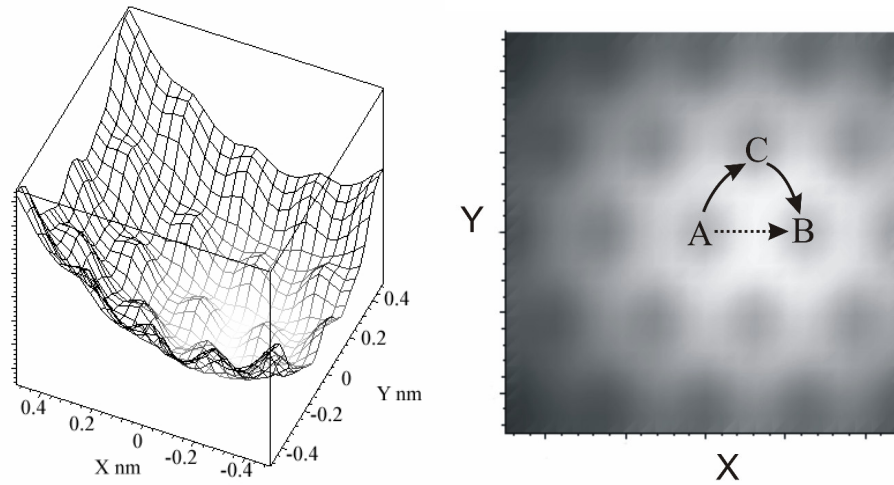


Fig 4.13. Left: The two-dimensional model potential combining the interaction of the tip with the 2D graphite lattice and the elastic energy of a cantilever with an effective spring constant along both X- and Y-directions of 0.5 N/m. The intersections of the minima in X and Y directions shows the possible stable potential minima, to which the tip can jump. Different lines weaved parallel to the x-axis show the geometrical variations in surface corrugations that cause the geometrical lubricity effect discussed in section 4.6 b. **Right:** grey-scale representation of the 2D total potential energy profile, with the potential minima represented by the bright parts and the potential barriers shaded in dark. Two possible trajectories of the tip between two energy minima, (A) and (B), are shown, one direct and the other via an intermediate site (C).

This situation can be viewed as a classical analogue to the concept of Feynman's path integral. There can be an infinitely large number of possible trajectories between two points, for example minima A and B in the potential (Fig. 4.13). Since the energy barriers for these trajectories are not the same, the probabilities for these trajectories depend on the support velocity (and on temperature). In our example, the tip tends to favor the direct potential barrier from A to B at high velocities, even though this barrier is initially relatively high. At high velocities the tip simply does not have enough time to visit one of the two neighboring local minima, sideways to the forward trajectory, before jumping into the energy minimum at B in front. The probability for the tip to choose an alternative, more complex but lower-energy trajectory, for instance from A to C and then from C to B, increases with decreasing scan velocity. At very low

velocities, the tip almost never traverses the higher potential barrier in front of it, but it nearly always travels from A to B via C.

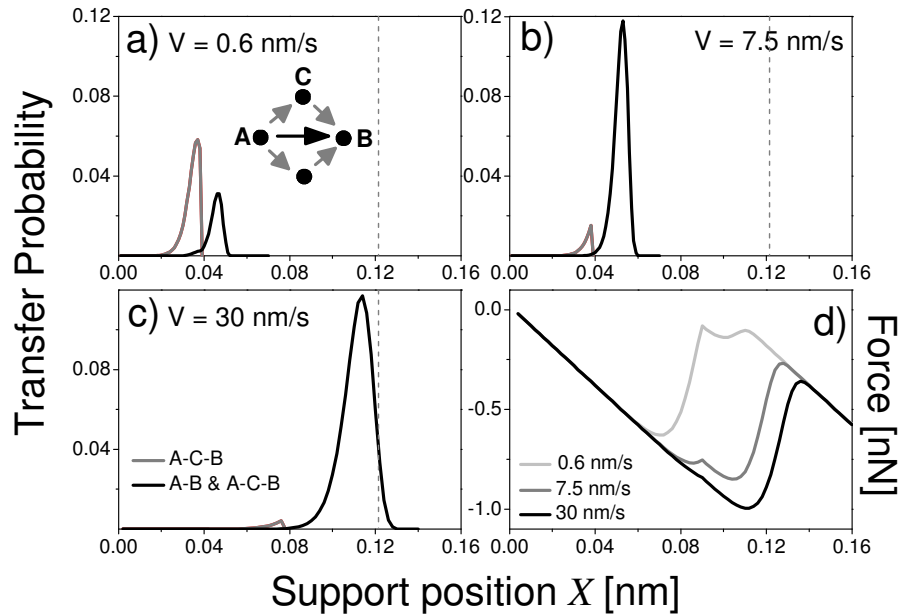


Fig. 4.14. The transfer probability of the tip from the initial potential minimum to the final potential minimum (separated by a lattice distance) calculated for three scan velocities a) 0.6 nm/s, b) 7.5 nm/s and c) 30 nm/s respectively (spring constant $k = 4.5$ N/m). The grey lines show the probability of two-dimensional trajectories (A-C-B) that are dominating at lower velocities and black lines indicate the probability of crossing the barrier directly, which dominates at high velocities. Panel (d) shows the differences in the lateral force variations between the three velocities due to the change from two- to one-dimensional motion of the tip. The grey dotted line is the critical point and the peaks shift more towards the left as the velocity decreases, as a result of the pre-critical jumps.

The transfer probabilities of the tip are shown in Fig. 4.14 for three different scan velocities. At very low velocities (Fig. 4.14a; thermal drift regime) the probability of two-dimensional trajectories (grey trajectory in Fig. 4.14; A – C – B in Fig. 4.13) is higher than that for directly traversing the barrier in front. The preference for such two-dimensional tip motion reduces drastically when the velocity is increased (Fig. 4.14b; stochastic regime). At high velocities the two-

dimensional trajectories are very unlikely, as Fig. 4.14 c shows (regime of pre-critical jumps), where the transfer probabilities calculated in one and two dimensions are nearly identical. The resulting differences in the average lateral force variations behavior can be seen in Fig. 4.14d.

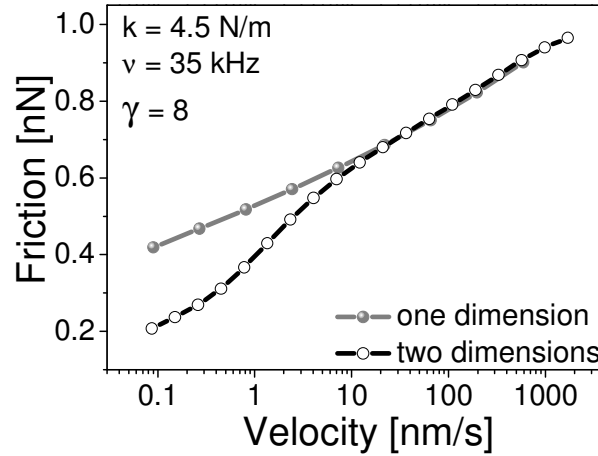


Fig. 4.15. Comparison between the velocity dependence of friction in one- and two-dimensional calculations of thermolubricity for the following choice of parameters, $k = 4.5$ N/m, $v = 35$ kHz and $\gamma = 8$. The enhanced two-dimensionality of the trajectories reduces the calculated value of the friction force significantly at lower velocities in the 2D model.

The consequence of the two-dimensional trajectories that dominate at lower velocities is an easier, i.e. lower-energy passage to the next potential minimum in front of the tip than via a direct, one-dimensional trajectory. As a result, the friction force at lower velocities is significantly lower when calculated for the full ensemble of two-dimensional trajectories than for the one-dimensional case. Fig. 4.15 gives a comparison between the two cases over a wide range of scan velocities. There has been one earlier calculation of thermal effects on friction in two dimensions [33,34]. The effect of the dimensionality was much less dramatic in this calculation. However, in this calculation only the pre-critical jumps were considered. What we find is that it is in the thermal-drift regime where multiple jumps dominate the dynamics that the difference between one and two dimensions becomes noticeable.

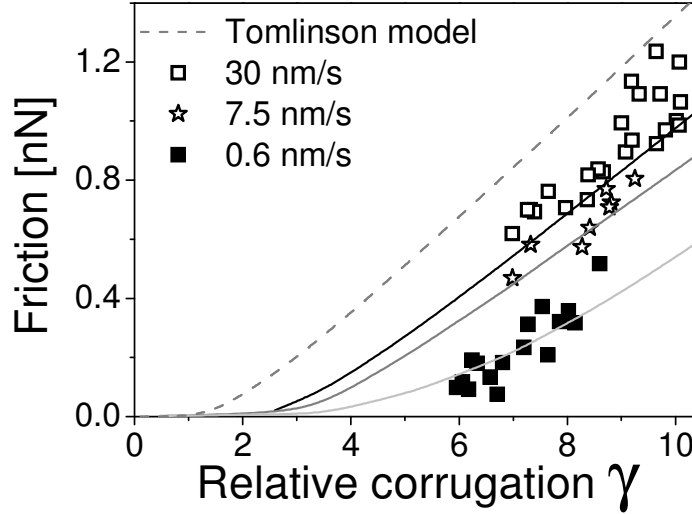


Fig. 4.16. Comparison of the measured γ -dependence of friction at three low velocities with the two-dimensional thermolubricity model. A reasonable fit to all data is obtained with a single attempt frequency of 35 kHz.

The effect of introducing the two-dimensional nature of the trajectories is to make the velocity dependence of the friction force much stronger than it is in the one-dimensional case. In order to establish whether this effect is sufficient to account for the strong velocity dependence observed in Fig. 4.12, we repeated the fitting procedure with our two-dimensional model calculation. Figure 4.16 shows that with a single attempt frequency of $\nu = 35$ kHz the two-dimensional model can indeed fit the data reasonably well. This frequency is one order of magnitude higher than the resonance frequency of the Tribolover. This forces us to reconsider the simple interpretation of ν in terms of the cantilever eigen-frequency.

4.8 Possible necessity for a multiple-mass-multiple-spring description

In the previous section we have seen that a consistent description of all measurements over the full range of experimentally accessed velocities and the full range of relative corrugations is obtained with a rate-equation theory that takes into account the full wealth of thermally activated motion of the tip, including multiple

forward and backward jumps and including sideways jumps, i.e. trajectories with a distinct two-dimensional character. Each of these complicating elements forms an essential ingredient for a faithful description, in particular at the lower velocities. In spite of its seeming complexity, the complete set of rate equations contains only a single adjustable parameter, a common pre-exponential factor, ν , which we have associated with the natural frequency of the system, namely the resonance frequency of the cantilever. Although the (single-velocity) measurements analyzed in Chapter 3 seemed to be in accordance with this picture, the velocity dependence investigated in this chapter and the more complete, i.e. two-dimensional model calculations presented here show that the value of ν found previously by fitting the one-dimensional model to the measurements in Chapter 3 was fortuitously close to the cantilever resonance frequency. We now observe that the more complete treatment provides a simultaneous fit over the entire range of conditions for a value of ν that is one order of magnitude above the cantilever resonance frequency. In this section we speculate about the origin of this high value of the pre-exponential factor.

If we still associate ν with a frequency of mechanical motion, we should search for a higher-frequency element in our system. One obvious element is formed by the tip itself. As we have already discussed, the spring constant measured for our system is systematically below that of the Tribolover. Part of the extra compliance is concentrated in the flexibility of the tip and, in particular, of the thinner end part of the tip. Since the tip apex region also constitutes an effective mass, this extra mass-spring system introduces a second eigen-frequency, which we expect to be many orders of magnitude above that of the heavy Tribolover (see e.g. [35]). It is difficult to predict the effective value of the (single) pre-exponential factor that best describes the combined effect of the low-frequency cantilever motion and the high-frequency tip vibrations within a single-mass-and-spring model, but it seems reasonable to expect it to lie between these two frequencies, i.e. *above* the low resonance frequency of the Tribolover, in accordance with the relatively high value of ν found here.

Preliminary calculations show that the sliding dynamics of a two-mass-two-spring model can be rather complex and can lead to strongly counterintuitive combinations of dynamics. A dramatic example is the situation in which the tip is fully ‘lubricated’ by thermal excitations while the cantilever still performs stick-

slip motion in the effective, lower-amplitude potential reflecting the position-dependent average force exerted on it by the rapidly jumping and vibrating tip [36].

In Fig. 4.17, we provide preliminary experimental evidence that the cantilever is indeed not directly sensing the amplitude U_0 of the tip-substrate interaction but the amplitude of an effective potential, which depends significantly on the scan velocity.

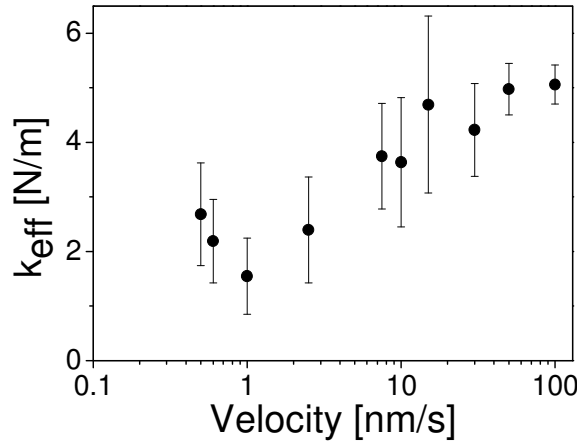


Fig. 4. 17. Variation of the effective spring constant (slope of the initial, static part of the friction loops) with the scan velocity. The strong reduction in the effective spring constant at lower velocities is not expected in the framework of a single-mass-single-spring model and is consistent with the presence of an additional, high-frequency mass-spring combination.

Since the tip-surface potential has not been varied in Fig. 4.17, a variation of k_{eff} should not be expected in the context of a single-mass-single-spring description. The strong reduction in k_{eff} at low velocities must reflect a reduction in the amplitude of the effective potential experienced by the cantilever, which is consistent with the two-mass-two-spring scenario.

4.9 Summary

In this chapter we have presented a simple rate-equation theory and measurements of the velocity dependence of friction between a tungsten tip and a graphite surface. Particular attention has been paid, both in the theory and in the experiment to the

regime of ultra-low velocities where the effect of thermal excitations completely dominates the motion of the tip. In addition to the range of velocities where the tip performs early, pre-critical jumps over the energy barriers, which leads to a modest, logarithmic reduction of the friction force, we identify an ultra-low velocity regime where the friction force scales linearly with velocity and it vanishes in the limit of zero velocity. Although our one-dimensional theory provides an excellent fit to the corrugation dependence of the friction force at each separate velocity, a simultaneous fit for all velocities can only be obtained with a set of rate equations for motion in a two-dimensional energy landscape. Although our theory provides a complete description of our friction data over the full range of velocities and potential corrugations accessed in the experiment, the single fitting parameter in this theory, the pre-exponential factor for thermally activated jumps between the potential energy wells, is found to be one order of magnitude above the resonance frequency of our cantilever. This interesting ‘discrepancy’ forms an important open question, for which we have suggested a potential answer in the form of the additional rapid dynamics of the tip apex, which has not been accounted for in our present theory. Further experimental and theoretical work will be necessary to resolve this issue.



4.10 References:

1. S. Yu Krylov, K.B. Jinesh, H. Valk, M. Dienwiebel, J.W.M. Frenken, *Phys. Rev. E* **71**, 65101(R) (2005).
2. A.E. Filippov, J. Klafter, M. Urbakh, *Phys. Rev. Lett.* **92**, 135503 (2004).
3. P. Reimann, M. Evstigneev, *Phys. Rev. Lett.* **93**, 230802 (2004).
4. G. He, M.H. Müser, M.O. Robbins, *Science* **284**, 1650 (1999).
5. G. Reiter, A.L. Demirel, S. Granick, *Science* **263**, 1741 (1994).
6. E. Riedo, F. Levy, H. Brune, *Phys. Rev. Lett.* **88**, 185505 (2002).
7. M.G. Rozman, M. Urbakh, J. Klafter, *Phys. Rev. Lett.* **77**, 683 (1996).
8. V.L. Popov, *Phys. Rev. Lett.* **83**, 1632 (1999).
9. E. Gnecco *et al*, *Phys. Rev. Lett.* **84**, 1172 (2000).
10. Y. Sang, M. Dube, M. Grant, *Phys. Rev. Lett.* **87**, 174301 (2001).
11. E. Riedo, E. Gnecco, R. Bennewitz, E. Meyer, H. Brune, *Phys. Rev. Lett.* **91**, 84502 (2003).
12. A. Schirmeisen, L. Jansen, H. Fuchs, *Phys. Rev. B* **71**, 245403 (2005).
13. C. Drummond, J. Israelachvili, *Macromolecules* **33**, 4910 (2000).
14. J. Gao, W.D. Luedtke, U. Landman, *J. Phys. Chem. B* **102**, 5033 (1998).
15. M. He, A.S. Blum, G. Overney, R.M. Overney, *Phys. Rev. Lett.* **88**, 154302 (2002).
16. A. Larkin, S. Brazovskii, *Solid State Commun.* **93**, 275 (1995).
17. J.R. Rice, A.L. Ruina, *J. Appl. Mech.* **105**, 343 (1983).
18. T. Baumberger, P. Berthoud, C. Caroli, *Phys. Rev. B* **60**, 3928 (1999).
19. J.N. Glosli, G.M. McClelland, *Phys. Rev. Lett.* **70**, 1960 (1993).
20. V.V. Tsukruk, V.N. Bliznyuk, J. Hazel, D. Visser, M. P. Everson, *Langmuir* **12**, 4840 (1996).
21. H. Dekker, A.M. van den Brink, *Phys. Rev. E* **49**, 2559 (1994).
22. O.K. Dudko, A.E. Filippov, J. Klafter, M. Urbakh, *Chem. Phys. Lett.* **352**, 499 (2002).
23. M. Evstigneev, P. Reimann, *Europhys. Lett.*, **67**, 907 (2004).
24. O. Zwörner, H. Hölscher, U.D. Schwarz, R. Wiesendanger, *Appl. Phys. A* **66**, S263 (1998).
25. O.M. Braun, M. Peyard, V. Bortolani, A. Franchini, A. Vanossi, *Phys. Rev. E* **72**, 56116 (2005).
26. O.M. Braun, M. Peyard, V. Bortolani, A. Franchini, A. Vanossi, *Phys. Rev. E* **72**, 56116 (2005).

-
27. W.G. Conley, A. Raman, C.M. Krousgrill, *J. Appl. Phys.* **98**, 53519 (2005).
 28. Q. Zhang, Y. Qi, L.G. Hector, Jr., T. Çağın, W.A. Goddard III, *Phys. Rev. B* **72**, 45406 (2005).
 29. C. Caroli and P. Nozières, in *Physics of Sliding Friction*, edited by B. N. J. Persson and E. Tosatti, Vol. 311 of NATO Advanced Study Institute, Series E: Applied Sciences, Kluwer, Dordrecht (1996), page 27.
 30. C. Daly, J. Zhang, J.B. Sokoloff, *Phys. Rev. E* **68**, 66118 (2003).
 31. M. Dienwiebel, G. S. Verhoeven, N. Pradeep, J.W.M. Frenken, J.A. Heimberg, H.W. Zandbergen, *Phys. Rev. Lett.* **92**, 126101 (2004).
 32. S. Yu Krylov (Institute of Physical Chemistry, Russian Academy of Sciences, Moscow), personal communications.
 33. C. Fusco, A. Fasolino, *Phys. Rev. B* **71**, 45413 (2005), C. Fusco, *Friction and diffusion dynamics of adsorbates at surfaces* PhD Thesis, University of Nijmegen, 2005, page 107 – 132.
 34. C. Fusco, A. Fasolino, *Phys. Rev. B* **71**, 45413 (2005).
 35. S. Maier, Y. Sang, T. Filleter, M. Grant, R. Bennewitz, E. Gnecco, E. Meyer, *Phys. Rev. B* **72**, 245418 (2005).
 36. J.A. Dijksman, S. Yu. Krylov, J.W.M. Frenken, *unpublished*.

Chapter 5

Effect of forced excitations on atomic-scale friction

We investigate the influence of external excitations of the cantilever of our FFM on the atomic-scale friction between a tungsten tip and a graphite surface. At the lateral resonance frequency of the cantilever, we find that friction goes nearly to zero. The effect can be explained in simple terms and forms a promising strategy for friction lowering in practical devices.

5.1 Introduction

In this chapter, we examine the effects of exciting the FFM cantilever at its lateral resonance frequency using a simple acoustic technique. Basically, by shaking the cantilever with an external force, we energize the system and thus enhance the hopping rate of the tip between neighboring potential minima. This is to some extent analogous to the effect of increasing the temperature and it results in a reduction of the friction force. Recent theoretical studies are in accordance with this qualitative picture and indicate that the excitation of a lateral resonance of the substrate can induce a higher rate of tip hopping, thus significantly reducing friction [1].

Although this idea is relatively new in the context of friction force microscopy[2], the technique of reducing friction with resonant vibrations is well-known and applied in engineering research [3]. Surface acoustic waves (SAW) are used as a tool to generate high-frequency oscillations and study the effects of lateral and vertical vibrations on microscopic friction. In these experiments, usually radio frequency (RF) signals are applied to electrode patterns on piezoelectric substrates to induce highly polarized and localized waves on the surface. AFM probes can be used to measure friction with and without the RF signal [3]. The advantage of this method is the precision in controlling the waves without inducing undesired vibrations in mechanical components of the system. This allows one to investigate a variety of aspects of resonance-induced lubricity, e.g. by applying in-plane or lateral waves that are perpendicular to the k -vector (Love waves) or waves that are polarized in the plane spanned by the k -vector and the surface normal (Rayleigh waves). Another approach is to induce vibrations by exposing the system to sound, thus shaking the substrate (and possibly also the cantilever and tip) with various amplitudes [4].

In this chapter, we use a loudspeaker to examine the effect of the non-thermal excitation of the lateral resonance motion of the cantilever on friction. The central idea of this chapter can be viewed as a corollary to the two previous chapters on thermolubricity, where the intrinsic thermal excitations of the system were shown to be responsible for a reduction of the friction force. Here we study the same effect in a more artificial way, by exciting the system externally and causing what has been called “induced superlubricity”[3].

5.2 Dependence of friction on excitation frequency

The advantage of our sensor, the Tribolover[®], is that due to its architecture it has a lateral spring constant that is lower than its normal spring constant. This makes the lateral resonance frequency of the sensor lower than the normal resonance frequency. For the sensor used in these experiments, the lateral spring constants are both 6.1 N/m and normal spring constant is 30.5 N/m. The lateral resonance frequency of the cantilever when in contact with the surface is 3.6 kHz.

For this experiment we used a regular loudspeaker, driven by a sine-wave generator with which we varied the frequency in the range of 0 – 6 kHz, i.e. around the 3.6 kHz natural frequency of the system. The resulting sound level was not quantified. The loudspeaker was placed close to the microscope with its central axis parallel to the lateral plane of the Tribolover. In practice we found that the precise location and orientation of the loudspeaker had a relatively modest influence on the measured amplitude of the excitations in the FFM. We also found that at each loudspeaker position we could also excite cantilever vibrations along the normal direction. The friction measurements were performed at room temperature and at low relative humidity with an etched tungsten tip, glued in the sensor, on an HOPG substrate. In all friction measurements a feedback system was used to keep the normal force constant at 3.7 nN. The scan range was always 3 nm and the support velocity was 30 nm/s.

Figure 5.1 shows a frequency spectrum, obtained by recording the output amplitude of one of the four interferometers (X_1) during a sweep of the sound frequency at a constant sound amplitude (constant amplitude of the voltage driving the loudspeaker), while the tip was in contact with the HOPG substrate. We recognize the frequency of the two lateral modes of the cantilever and the frequency of its perpendicular mode. Of course, not only the sensor vibrations are excited by the sound of the loudspeaker but also vibrations in the same frequency range of other mechanical components of the system, including the substrate. This gives rise to several additional peaks in Fig. 5.1.

In Fig. 5.2 we show the friction force measured as a function of the driving frequency. We see that at the lateral resonance frequency of the cantilever, there is a drastic reduction of friction.

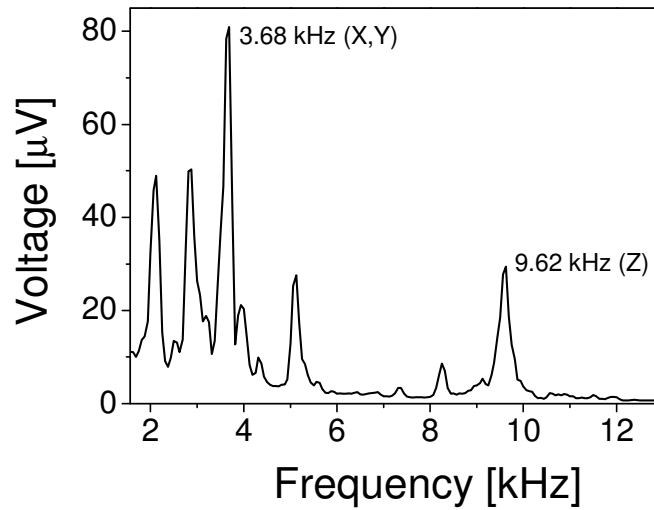


Fig. 5.1. Resonance spectrum measured with the Tribolover, while the tip is in contact with the graphite surface at a normal load of 3.7 nN, during a sweep of the frequency of the externally applied sound. The peaks around 3.68 kHz correspond to the lateral resonance of the cantilever and the peak at 9.6 kHz corresponds to the normal resonance. The other peaks come from the sound-induced vibrations in the rest of the system and are only visible when the tip is in contact with the substrate.

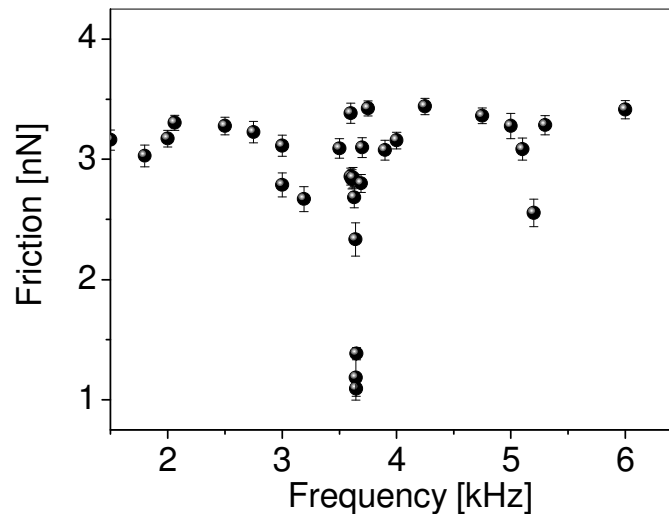


Fig. 5.2. Friction force as a function of the excitation sound frequency (at a constant loudspeaker voltage amplitude of 1 V). A dramatic reduction of friction is observed at the lateral resonance frequency of the cantilever (3.65 kHz). The modest reduction at 5.2 kHz corresponds to the resonance present when the tip is in contact with the surface. Reduction of friction due to the normal resonance is not shown here.

5.3 Friction at the lateral resonance frequency of the Tribolever

Exciting the cantilever at its lateral resonance frequency is similar to increasing the thermal energy of the system, but in this case only in the vibrational mode of interest, which we expect to be most efficient in enabling the diffusion of the tip along the substrate lattice. Analogous to increasing the temperature, we may change the amplitude of vibration of the cantilever (and the tip) by varying the output of the loudspeaker. This is done in Fig. 5.3, where the loudspeaker drive amplitude is varied over a full order of magnitude. Figure 5.3 shows several interesting features. Clearly, the lateral force exhibits periodic variations with an amplitude that increases with the sound level. We have verified that the frequency of these variations corresponds with the 3.65 kHz resonance frequency of the cantilever.

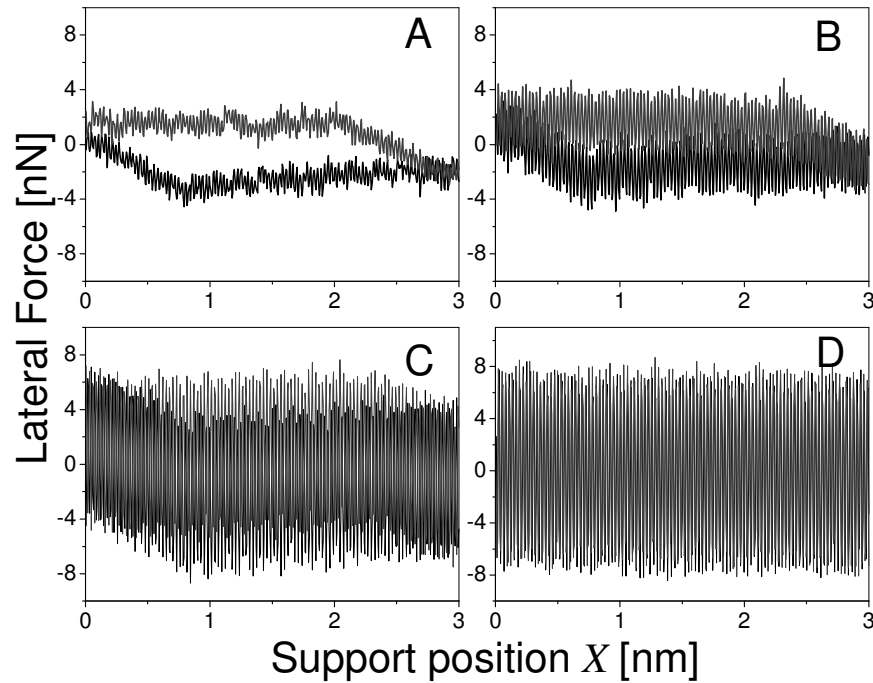


Fig. 5.3. Lateral force loops at different amplitudes of the loudspeaker, which is driven with a sine wave at the lateral resonance frequency of the cantilever: (A) 0.5 V, (B) 1.5 V, (C) 4 V and (D) 5.5 V. Black lines are forward and grey lines are reverse scan-lines. The forced cantilever oscillations are clearly visible.

The amplitude of the driven force oscillations and the maximum force are both increasing with increasing sound level, whereas the average lateral force, i.e. the friction, is reducing with increasing loudspeaker output. How strong the imposed vibrations are can be read off from the cantilever oscillations on the initial, static part of the friction loops, where the tip is stuck in the initial potential well. This amplitude is plotted in the left panel of Fig. 5.4 versus input voltage amplitude of the loudspeaker.

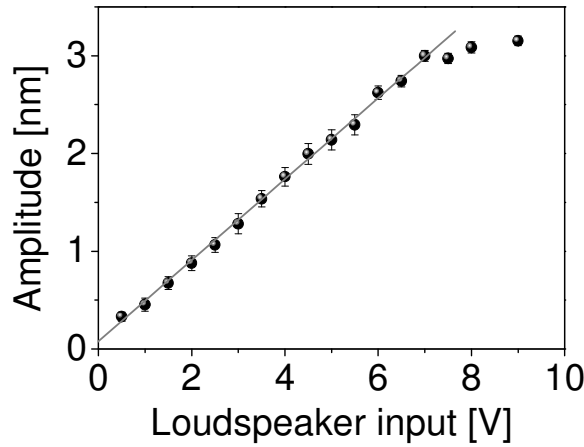


Fig. 5.4. Amplitude of the driven oscillation of the Tribolover in the static part of the lateral force loop as a function of the voltage amplitude offered to the loudspeaker. The grey straight line is a linear fit to the linear part of the data.

The importance of Fig. 5.4 is that it enables us to convert the input parameter, namely the loudspeaker input voltage amplitude, into more physical terms such as the cantilever vibration amplitude or the AC force amplitude. Figure 5.4. B shows how the friction force reduces systematically as the amplitude of oscillation of the cantilever increases. At a cantilever amplitude (peak-peak) of 3 nm, friction has vanished nearly completely. This amplitude would correspond to an experimentally ‘impossible’ temperature of $\sim 10^6$ K.

5.4 Interpretation

Here, we provide a simple explanation for the observed lowering of the friction force under the influence of the external excitation. Since the experiment was

performed at the lateral resonance frequency of the cantilever and we observe (Fig. 5.1) that the system responds to this excitation only in a relatively narrow frequency range around this resonance, we can safely assume that the loudspeaker is directly driving the motion of the cantilever, i.e. it exerts a periodic force on the cantilever. The restoring force on the cantilever is the combination (sum) of the interactions it has with the support, with the full Tribolover spring constant of 6.1 N/m and the combined stiffness of the tip apex and the apex-substrate interaction, which is in the order of 4.9 N/m. This situation is fundamentally different from the familiar setting in which the support acts on the cantilever and the cantilever transmits that same force via the flexible tip to the apex-substrate contact. In the present case, the maximum force Ak_T that the cantilever exerts on the support is much larger than the maximum force $A\left[k_t^{-1} + \left((d^2U/dx_t^2)_{\max}\right)^{-1}\right]^{-1}$ it simultaneously exerts via the tip on the contact. Here, A is the sound-driven vibration amplitude of the cantilever, k_T is the spring constant of the Tribolover, k_t is the tip compliance and $(d^2U/dx_t^2)_{\max}$ is the maximum curvature of the tip-substrate interaction potential. When the support starts its scanning motion and the amplitude A is not too large, the cantilever initially simply oscillates around its average position and the tip moves adiabatically with it, but it stays within one well of the tip-substrate interaction potential. Before the support has reached the position where the first slip event would occur in the absence external excitation, the maximum excursions of the cantilever in the forward direction already provide the geometry at which the tip overcomes the barrier to the next potential well. It is easy to show that the maximum and minimum forces measured between the cantilever and the support at this point is increased and lowered by an amount close to the amplitude of the external force on the cantilever, i.e. by the product $\pm A\left\{k_T + \left[k_t^{-1} + \left(d^2U/dx_t^2\right)^{-1}\right]^{-1}\right\}$ of the displacement amplitude and the combined spring constant to the support and to the contact, experienced by the cantilever. The force variations exerted by the oscillating cantilever on the tip are much smaller, namely $\pm A\left[k_t^{-1} + \left(d^2U/dx_t^2\right)^{-1}\right]^{-1}$. The friction force will be lowered by

approximately $A \left[k_t^{-1} + (d^2U/dx_t^2)^{-1} \right]^{-1}$. When the amplitude is not too large, the situation of ‘early’ jumps is reminiscent of the case of pre-critical jumps in the case of thermal excitation (see Chapters 3 and 4). For the conditions of the present experiment our estimate predicts that the friction force should vanish at an amplitude in the order of $2.5 \text{ nN}/(1.5 \text{ N/m}) \approx 1.8 \text{ nm}$, which is in the correct range, compared to Fig. 5.5.

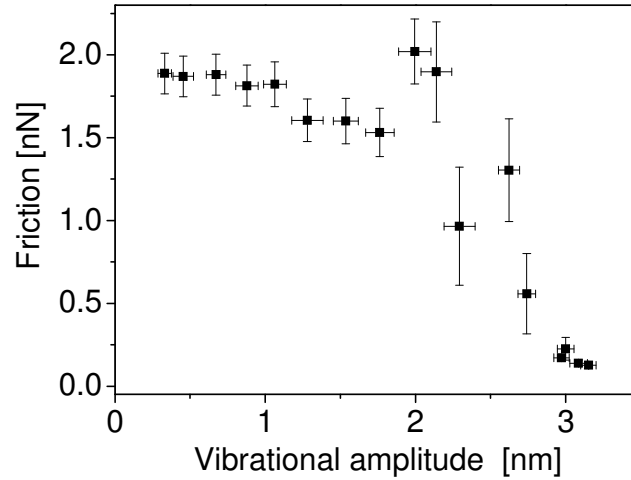


Fig. 5.5. Friction as a function of the amplitude of forced vibration of the cantilever. The equivalent temperature, corresponding to this amplitude is indicated in the top horizontal axis.

When the amplitude is sufficiently large, the tip is forced to jump back and forth one or more well distances during every oscillation period. This situation is somewhat analogous to the thermal drift regime in the case of thermal fluctuations.

5.5 Discussion

Shaking the cantilever at its resonance frequency, using external forces, has effects analogous to those of increasing the temperature of the FFM. Here, we have not provided a full theoretical analysis, but it is clear that whereas the thermal effects of Chapters 3 and 4 are intrinsically stochastic in nature, the imposed vibrations treated in the present chapter make the tip overcome the potential barriers of the

surface in a deterministic way. In both cases the friction force is reduced. As we have shown here, the reduction in the friction force obtained via external excitation of the cantilever at its lateral resonance is dramatic; it is equivalent to an unrealistically high rise in temperature. This shows that lateral resonances form a promising approach for the dry lubrication of moving parts in mechanical devices, especially in MEMS and NEMS, where common lubricants fail to work. Surface acoustic waves (SAW) are generally used to reduce friction [5] and ultrasonic force microscope (UFM) studies are useful to demonstrate phonons as the main dissipation channels in nanoscopic sliding [6].



5.6 References:

1. Z. Tshiprut, A.E. Filippov, M. Urbakh, *Phys. Rev. Lett.* **95**, 16101 (2005).
2. A. Socoliuc *et al.*, *Science* **313**, 207 (2006).
3. T. Hesjedal, G. Behme, *IEEE Trans. Ultrason., Ferroelect., Freq. Contr.* **49**, 356 (2002).
4. F. Dinelli, S.K. Biswas, G.A.D. Briggs. O.V. Kolosov, *Appl. Phys. Lett.* **71**, 1177 (1997).
5. G. Behme, T. Hesjedal, *J. Appl. Phys.* **89**, 4850 (2001).
6. X. Cui, A. La Rosa, *Appl. Phys. Lett.* **87**, 231907 (2005).

Chapter 6

Capillary condensation in atomic-friction experiments

In this chapter we study the influence of water condensing between a tungsten tip and a graphite surface – a phenomenon known as capillary condensation. We find that atomic scale friction increases with relative humidity in this system. The condensate forming between the tip and the surface mechanically behaves like ice, exhibiting elastic behavior for small deformations and very long timescales for the relaxation of plastic deformation.

6.1 Introduction: slippery when wet

Nearly 70 percent of the Earth surface is covered with water. Water is one of the prime substances enabling life on this planet and it is the most common lubricant in everyday life, making it slippery when wet. Unlike manmade lubricants that are entirely oil-based, nature lubricates biological machinery with water-based lubricants [1]. Water is sometimes used in industry as a lubricant between sliding mechanical parts; but there it usually serves as a medium to remove the wear debris of the sliding rough surfaces, like polishing agents typically do. The slipperiness of ice is often associated with the presence of very thin layers of water at the interface between the ice and the sliding body, which would be there because of interfacial melting, pressure melting or frictional melting, as discussed already by Faraday in 1839 [2,3].

However, the excellent properties of biological lubricants have prompted tribologists to investigate the possibilities of water-based lubricants as an efficient alternative for the traditional, ecologically unfriendly, oil-based compounds. In this quest, detailed, molecular-level understanding of how these bio-lubricants work is of prime importance (see Ref. [4] for a recent investigation of the lubricating properties of synovial fluids in cartilaginous joints).

Water works not only as a lubricant. As we mentioned in Chapter 1, water can form bridges between grains of sand and thus contribute to the stability of sand piles [5] and water is the material that determines the strength of seismic rock [6,7]. Hydration forces, associated with the presence of hydration shells of water molecules around ions in solutions account for the swelling of clay [8]. We see that the practical circumstances where water acts on interfaces, as a lubricant, an adhesive or otherwise, are manifold. For a full understanding of these important effects we need to investigate the behavior of spatially confined water down to the molecular level.

This chapter starts with an extensive overview of previous investigations of the behavior of liquids, in particular water, under extreme confinement. In the rest of this chapter and in Chapters 7 and 8 our findings will be presented of thin capillary water bridges, condensed between a tungsten tip and a graphite surface.

6.2 When is a lubricant a lubricant?

In a broader context, the abovementioned aspects of the behavior of water are part of the general question: when does a lubricant really behave as a lubricant, i.e. when does it reduce friction and avoid wear? We should realize that in many practical situations, in a car engine for instance, the molecules lubricating the moving parts undergo extreme pressure variations of many GPa as well as substantial temperatures changes of many 100 K. Research on the basic physics of lubrication in the last two decades shows that liquids under extreme confinement can behave entirely differently from the classical law introduced by Newton in 1686, which states that the shear stress σ is proportional to the shear rate, $\sigma = \eta (dy/dt)$, where η is the viscosity and dy/dt is the shear rate (= sliding velocity/film thickness). This linear relation holds only for small shear rates. At higher velocities the proportionality constant, ie. the viscosity itself, becomes a function of the shear rate. This is referred to as the non-Newtonian regime [9]. When energy dissipation in a lubricated contact can be described completely in terms of viscous damping in the lubricant and the lubricant behaves as a Newtonian fluid, the friction force across the contact scales linearly with the sliding velocity. Typically, at very low sliding velocities, lubricant molecules are squeezed out from between the sliding surfaces, and often only a small number of molecular layers remains in the gap. This geometry constitutes the boundary lubrication problem, where the friction is nearly velocity independent [10].

What happens to the dynamics of lubricant molecules under severe confinement? Simulations predict that hard-sphere fluids, when confined between two flat surfaces to a thickness of a few monolayers, can undergo various levels of ordering, ranging from layering (stratification) to complete crystallization [11,12,13]. As the thickness of the lubricant is reduced to some 5 molecular diameters, the fluid undergoes layering and acquires a partly solid-like character. When the solid-like character is sufficiently strong, the lubricant film can even sustain a finite shear stress. There are several reasons for disorder in these ordered films, for example deriving from the misfit with the two confining substrates. In fact, the shear motion of the substrates can involve the periodic destruction of order in the molecular film ('melting'), followed by a rapid re-ordering ('solidification'). At sufficiently high shear rates, this process of melting and solidification can result in a stick-slip type motion of the sliding surface [9,14]. Note that this is very

different from the *atomic* stick-slip motion discussed in previous chapters, the slip distances being orders of magnitude larger than a substrate lattice period. However, it should be noted that the transition from isotropic liquid to ordered substance, at least in the case of OMCTS, has been observed to proceed continuously, which implies that it is not a first-order phase transition [15,16].

A direct consequence of the liquid-solid transitions discussed above is a dramatic increase of the effective viscosity of the lubricant with reducing film thickness [17]. At sufficiently low shear rates the effective viscosity of such molecularly thin lubricant films can be 10^5 times or more as high as that of the bulk and the corresponding relaxation timescale slows down by a factor 10^8 with respect to the bulk [18]. Also, the translational diffusion within the lubricant film has been estimated to slow down by up to 4 orders of magnitude in such confined systems [19].

At higher shear rates, involving timescales below the typical relaxation time of the lubricant film, the layer remains fluid-like, resulting in a smooth motion of the sliding surface with a relatively low friction force [20]. For solid-like lubricant films under shear, friction of a lubricated sliding contact results from the phononic dissipation within the lubricant layers themselves, the energy being transferred to the substrates via the out-of-plane vibrations of the lubricant molecules into the heating up of the lubricant layer. These mechanisms are responsible for high friction [21]. At higher shear rate, beyond a critical velocity related to the sound velocity in the lubricant, a more smooth sliding motion emerges with lower dissipation. This is assumed to be because of the smooth slipping of the well-defined lubricant layers past each other. This scenario has been addressed in detail by Braun and coworkers recently [22], with the emphasis on the point that shear may induce order in the ‘molten’ film along the shearing plane and thus enabling sliding with less dissipation.

We can conclude that there is no straightforward answer to the question: ‘When is a lubricant a lubricant?’ The friction force of the lubricated contact depends on many factors, such as the film thickness, the tendency of the liquid lubricant to stratify under confinement and to crystallize, the temperature, the normal pressure, the atomic structure of the sliding surfaces, the possible interfacial commensurability of the ordered fluid with the sliding walls, the relaxation timescale in the solid or liquid lubricant and the velocity of sliding [17,18,23,24]. These factors determine the critical velocity, at which the surfaces exhibit smooth

sliding [25,26], below which is the highly dissipative stick-slip (subsequent solid-liquid phase transition) regime. In addition, temperature of the lubricant plays a significant role, since the critical velocity shifts to lower values with the increase of the temperature [27].

The majority of experimental work that has been reported in this field has been performed with the surface force apparatus (SFA), taking full advantage of the atomically smooth and locally parallel mica sheets that constitute an ideal confined geometry to investigate boundary lubrication problems. The liquid lubricant that has been studied in most detail is a *simple* molecule, namely octamethylcyclotetrasiloxane (OMCTS). It is a large (0.85 nm diameter), nearly ideal, physical realization of a hard-sphere molecule, optimal for comparison with simple theories and computer simulations. OMCTS and cyclohexane (0.5 nm diameter) have been shown to exhibit layering in numerous SFA experiments [28,29]. Films of linear molecules such as dodecane and alcohol molecules such as 1-undecanol also have been observed to exhibit layering parallel to the shear plane [30,31]. In this sequence of investigations, not only pure liquids, but also liquid mixtures with different concentrations have been subjected to detailed studies. For instance, SFA measurements on mixtures of OMCTS and cyclohexane show that at lower concentrations of cyclohexane, the solvation force is oscillatory with a period corresponding to the pure OMCTS molecular size, but the range and amplitude of these oscillations are reduced because of less efficient packing of OMCTS when a small fraction of the smaller cyclohexane molecules is present. At equal concentrations, the solvation force is oscillatory in the form of an irregular sequence of layer distances, corresponding to the molecular sizes of both OMCTS and cyclohexane [32,33].

6.3 Conflicting evidence on lubricating properties of water at the nanoscale

Lubrication properties of thin water films have become a highly controversial subject because different research groups derive widely different conclusions from the same type experiments in the same type apparatus. In many SFA investigations water is observed to behave similar to other molecules, mentioned above, exhibiting layering under confinement as can be seen from oscillatory force-distance curves, with an oscillation period of 0.3 nm, corresponding to the size of

one water molecule [34,35]. The natural consequence of this solvation effect is a dramatic increase of shear response and an enhancement of the viscosity by many orders of magnitude, as the distance between the confining surfaces is reduced [36,37]. By contrast, other SFA experiments seem to indicate strongly that water cannot be ordered under confinement. Instead, water molecules seem to be simply squeezed out smoothly from the contact region under the increasing normal load, the remaining thin film retaining its bulk viscosity (0.009 Pa s) and fluidity even under extreme confinement down to 0 ± 0.4 nm [38]. Note, that the latter result was derived mainly from the measurement of the timescales of snap-into-contact of the mica surfaces from a distance of 3.5 nm to 0 ± 0.4 nm. A recent study using interfacial force microscopy shows that the viscosity of water increases up to 7 orders of magnitude with respect to bulk water, when confined to less than 1 nm thickness [39]. The fluidity of hydration layers was concluded to follow the same behavior under confinement [40,41,42]. In another SFA experiment, a confined solution of MgCl_2 was found to have a viscosity enhancement of 10^7 times that of bulk water [43]. Another recent study reports that under the SFA configuration, an NaCl solution has a viscosity enhancement of 2 to 4 orders of magnitude with respect to bulk liquid water [44].

Compared to the simple, hard-sphere-like behavior of OMCTS, a polar, hydrogen-bonded material like water is notoriously difficult to model, for example in a molecular dynamics simulation. In such calculations, the behavior of water under confinement – for example the oscillatory solvation or complete squeeze out – depends on details of the interaction potential of the water [45]. As we have seen already, the probability of ordering under confinement greatly depends on the atomic structure of the confining walls and the interfacial interactions. Moreover, unlike OMCTS, water is not a spherical molecule (it can be regarded as elliptical), which influences the packing geometry under confinement. The reason proposed for the water to be squeezed out completely is the high translational entropy of water molecules [38] and the confining walls suppress the formation of the highly ordered, hydrogen-bonded water network [46].

The ongoing debate in the SFA literature on the viscosity and the corresponding lubricating properties of ultra-thin water films has received an alarming twist with the recent observation that the cleavage and cutting procedure commonly used to prepare the mica surfaces in SFA measurements results in a contamination of the surfaces with platinum nanoparticles coming from the hot

platinum wires used in this procedure! The vapor pressure of platinum at the melting temperature of mica (1613 K) is enough to deposit 0.1 monolayer of platinum on the mica, which is clustered into nanoparticles. When simple adhesive tape is used to cleave the mica, the surface is free of contaminants and enhanced layering is seen of OMCTS molecules in such clean systems [47]. This finding casts doubt on the validity of at least some of the SFA results published in the last decade on the nanoscale lubrication of thin liquid films [47, 48, 49].

6.4 Lubrication by water – AFM studies

Atomic force microscopes (AFM) are increasingly used to study the dissipation mechanism in molecularly thin lubricant films [50,51,52]. In comparison with the surface force apparatus, AFM gives a much smaller area of contact where lubricant molecules can be confined (for a good review of the progresses in this field until 1997, see [53] and the references therein). This may lead to a reduced tendency of the fluid to order but it has the enormous advantage that the region over which the substrate is required to be flat and free from ‘third particles’ in order to produce reliable measurements is also very small (as small as the scan size plus the contact area); in addition, since the instrument actually images the substrate (lateral force image), one can actually select clean and well-defined regions on a substrate and even compare with special regions, such as steps and other ‘defects’ on the surface. Another advantage is that the AFM can apply a high pressure in the lubricant with a relatively low applied normal load. Typical scan velocities in AFM range from a few nanometers to a few micrometers per second, which is a sufficiently wide range to measure noticeable (and possibly drastic) viscosity changes of the confined liquid.

In several earlier AFM studies, clear evidence has been found for ordering phenomena in thin lubricant films. For example, the observation of stratification of water under nano-confinement has been reported [54] and also local solvation shell measurements using a carbon nanotube tip on self-assembled monolayers (SAM) [55]. In a recent AFM study, Jeffery and colleagues have demonstrated layering of water on a mica surface up to a thickness of 7 molecular layers [56].

Although these AFM studies have not been aimed specifically at the friction or lubrication properties of the confined water, the general trend seems to be that the friction force increases in the presence of water. A new category of AFM and

FFM observations, focusing on the frictional properties of confined water is formed by capillary condensation studies [57]. These will be discussed in the next section.

6.5 Capillary condensation

When an SFA or AFM measurement is performed in air, which usually means at a non-zero relative humidity below 100%, the situation of two surfaces in (near) contact forms a potentially suitable geometry for the formation of a water bridge. This phenomenon of water vapor condensing in narrow gaps and cavities is known as capillary condensation [58]. In the SFA such necks have large diameters in the range of micrometers, even though the height can be in the order of only a nanometer. In AFM measurements, on the other hand, the small radius of curvature of the tip confines also the lateral dimensions of the water bridge to the nanometer regime, which enables us to investigate the lubricating properties of water confined in three dimensions to sizes of a few atom spacings. Recent Monte Carlo simulations have shown that the diameter of a capillary water bridge is determined largely by the contact diameter between the tip and the surface and that it cannot be narrower than 5 molecular diameters (1.9 nm), since the meniscus becomes unstable below this size due to thermal fluctuations [59].

The classical, macroscopic picture of a capillary meniscus was given by Lord Kelvin, in terms of the thermodynamics of the film and its molecular free energy [60]. When the radius of curvature of an asperity is below a certain threshold value, that contact allows the water vapor to condense into a capillary bridge between the two surfaces. This critical radius of curvature is known as the Kelvin radius [58]. If R_1 and R_2 are the principal radii of curvature of the meniscus formed, the effective radius r_{eff} of the meniscus is given by the simple relation:

$$\frac{1}{r_{eff}} = \frac{1}{R_1} + \frac{1}{R_2} \quad (6.1)$$

The Kelvin radius has been illustrated in Fig. 6.1, where a water meniscus formed between an AFM tip and a surface is schematically shown. Note that one of the radii corresponds to a convex curvature, so that it has to be counted as *negative* in Eqn. 6.1.

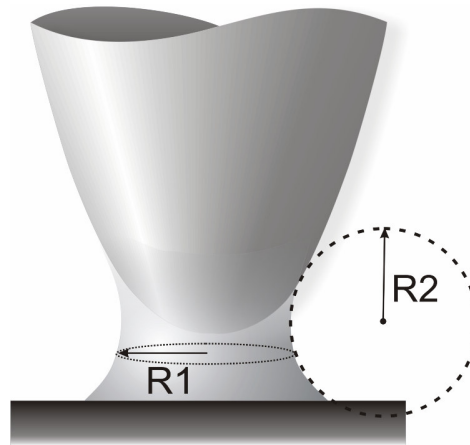


Fig. 6.1. The principal radii of curvature of a capillary meniscus. Together they should satisfy Eqn 6.1 for the Kelvin radius. The contacts of the capillary neck with the substrate and with the tip apex should have the equilibrium contact angles of water with these surfaces.

The equilibrium shape of the meniscus formed by capillary condensation depends on several factors, such as the surface tension γ of the liquid, the partial pressure of the vapor and the effective radius r_{eff} of the capillary bridge. The pressure inside the capillary condensate can be calculated using the Young-Laplace equation, and is below the ambient pressure. This is why the capillary meniscus has a negative radius of curvature (R_2 , in Fig. 6.1). The Laplace pressure $\Delta P = 2\gamma/r_{eff}$ across the air-water interface provides the change in molar free energy of $\Delta E = V \Delta P = 2V\gamma/r_{eff}$, where V is the molar volume of water. For a fixed temperature T , the vapor pressure determines the equilibrium radius of the droplet via the well-known Kelvin equation:

$$k_B T \ln(P/P_0) = 2\gamma v / R_K \quad (6.2)$$

Here, P_0 is the vapor pressure at which the vapor is in equilibrium with the liquid phase at temperature T and v is the molecular volume of water. At room temperature, the surface tension of water is 0.074 N/m, which gives the parameter $\gamma v / k_B T = 0.54$ nm [61,62]. Thus the Kelvin radius at a given relative humidity (RH) is given by

$$R_K (nm) = \frac{0.54}{\ln(RH)} \quad (6.3)$$

Note that, since $RH < 1$, R_K is negative, which means that the condensate should always have a shape with $R_2 < R_1$. It is also instructive to have a look at the actual numbers. They show that the actual size of the condensate for humidities not too close to 100% is in the regime of at most a few nanometers.

With the help of environmental scanning electron microscopy (ESEM), Schenk and colleagues have observed the formation of capillary bridges between a tungsten tip and a mica surface at various relative humidities [63]. Although Schenk and coworkers regard their observations as consistent with the Kelvin equation, their SEM images show that their R_{eff} is strongly positive, which should make their capillary bridges highly unstable. A recent study by Weeks and colleagues shows that the meniscus heights in AFM experiments at high RH values can be far greater than the Kelvin equation predicts [64]. These results are of direct importance in dip pen nanolithography (DPN) experiments, where the dimensions of the capillary meniscus determine the width of the written lines [65].

Capillary condensation plays an essential role in nano-scale friction measurements as well. A capillary condensate of 5 nm radius will have a strongly negative Laplace pressure of -30 MPa. This pressure difference between inside and outside the condensate causes a large adhesive force of 2.3 nN between the AFM tip and the surface. This enhanced pull-off force presents a well-known problem in many AFM experiments [66,67,68]. It also manifests itself often in MEMS devices, blocking motion and causing damage to the moving components.

This increased effective normal load due to capillary condensation causes an increase in the dynamic friction force. In addition, the capillary meniscus itself causes extra dissipation, via internal dynamics (turbulence) in the condensate. Humidity has also been shown to significantly increase the static friction force between solids [69], thus causing logarithmic increase with time (aging) of the friction coefficients [70]. Recently, Riedo and colleagues have reported atomic-scale friction experiments using AFM, where they demonstrate that friction increases logarithmically with the scan velocity on a hydrophobic surface while it decreases logarithmically on a hydrophilic surface at relative humidities high enough to initiate nucleation under the AFM tip [57,71,72]. They explain the logarithmic reduction of friction with the scan velocity with the assumption that the AFM tip is rough, with many nano-asperities that are close enough to the surface that they can support the formation of individual capillary bridges. During sliding

the changing geometry leads to the frequent removal of existing capillary bridges while new bridges are nucleating at the same time. The resulting balance between the breakage and nucleation of bridges determines the average number of bridges present and this, in turn, determines the average dissipation. The dependence of friction on scan velocity reflects that the formation of the bridges is a thermally activated process that is given less time when the scan velocity is higher. It is a matter of concern whether or not multiple nano-bridges can exist at the nanoscale separation typical for the AFM. The Laplace pressure in each bridge will prevent them from existing as individual bridges and they will coalesce to a single capillary meniscus, as we see in the direct observations of Schenk *et al* and Week *et al* [63,64]. Moreover, the logarithmic increase of friction on hydrophobic surfaces is assumed to be due to the thermally activated jumps of the tip in the substrate atomic potential wells in the complete absence of a capillary condensate, even at elevated RH values. But, as we will see later in this chapter, a capillary meniscus forms even on a HOPG surface and it screens the tip from the substrate potential corrugation, even though the HOPG is hydrophobic (contact angle of 86°).

6.6 Experiments: friction and relative humidity

For our experiments we used the set up described in Chapter 2, with an electrochemically etched tungsten tip scanning over a freshly cleaved HOPG surface under a constant normal load of 3.7 nN. Scan speeds were ranging from 0.05 nm/s to 100 nm/s and the scan range in this chapter was always 3 nm. To control the relative humidity, mixtures of dry nitrogen and nitrogen passed through distilled water were continuously flushed through the FFM chamber. This allowed us to control the relative humidity with an accuracy of $\pm 1\%$ from a minimum of 1% to a maximum of 60%. At humidities higher than 60% the optical signal of the four interferometers showed uncompensated drift. The temperature inside the chamber was kept constant at 295 K.

The first result that we present here of the RH-dependence of the friction force is shown in Fig. 6.2. We observe a rapid, modest increase at low humidities, followed by a slow increase up to RH=35%, after which the friction force rapidly increases with increasing RH. As we point out later in this chapter, at humidities above 10%, we lose atomic resolution, which indicates that water is actually intervening between the tip and the surface. This observation and the mere presence

of a humidity dependence of the friction force both strongly suggest that capillary condensation takes place between the tip and the surface. The increase of friction with increasing RH must be related to the increase in size (thickness and diameter) of the condensate. We will come back to this point later in this chapter. The fact that friction *increases* with humidity immediately shows that water does not act as a lubricant in this experiment.

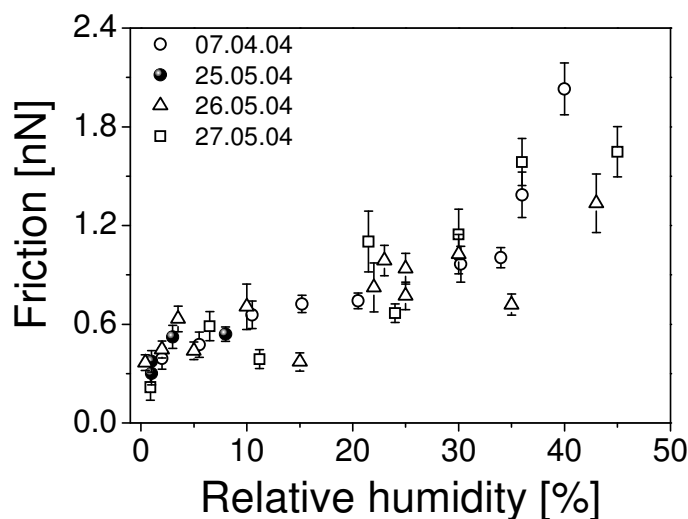


Fig. 6.2. Friction as a function of relative humidity, measured from 3 nm scans at a velocity of 30 nm/s at room temperature. Different symbols correspond to different data sets acquired over a 2-month period.

In Fig. 6.3 we show a first indication that there is a slow time dependence of friction in the case of a high humidity. The timescale involved here is orders of magnitude longer than the millisecond timescale expected (see below), which indicates that the condensate is behaving very differently from regular water.

The most important feature of Fig. 6.3 is that at the higher two relative humidities, the friction force is a slowly increasing function of the time passed since the start of the friction measurement, an effect that is completely absent at RH=1%. This observation raises several interesting questions. For example: is the slow evolution due to wear of the HOPG surface or is the tip slowly wetting the ‘fresh’, i.e. so far unscanned areas of the hydrophobic HOPG surface, or is the capillary condensate slowly changing its structure? We can rule out wear of the substrate as the observations are completely repeatable on the same scan area

without any sign of damage or permanent changes, even though the HOPG substrate would not be able to anneal out wear damage on a reasonable timescale at room temperature.

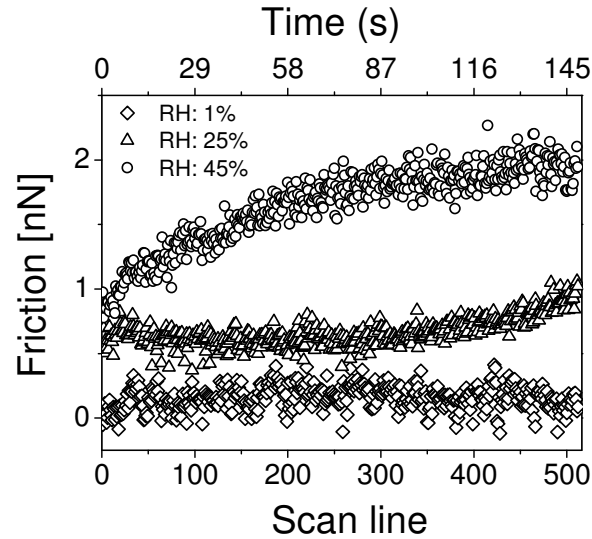


Fig. 6.3. Friction in individual scan lines, plotted versus the scan line number for three different RH values of 1%, 25% and 45%. The scan size was $3 \text{ nm} \times 3 \text{ nm}$ and the velocity was 30 nm/s . The upper horizontal axis shows the time passed during the 512 scan lines in each measurement.

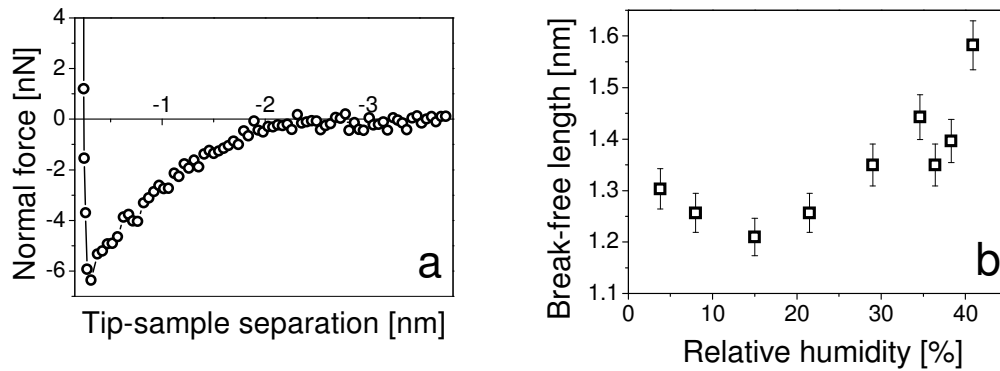


Fig. 6.4. a) A typical force-distance curve (pull-off direction) at 35% relative humidity. The difference between the location of the attractive (negative) force maximum and the distance at which the attraction has reduced to zero force is defined as the break-free length; b) Break-free length as a function of the relative humidity.

We conclude that the slow changes in friction reflect an effect of capillary condensation. One simple measurement provides insight into the dimensions and behavior of the condensate is to quantify the break-free length in force-distance curves at different relative humidities [66]. This is shown in Fig. 6.4.

We associate the break-free length with the maximum extension of the capillary meniscus before it breaks. It has been shown that this length is time dependent because of the nucleation of water from the surroundings [73]. Interestingly, for every value of the relative humidity the measured break-free length is significantly higher than the $2R_K$ (twice the Kelvin radius) height expected for the capillary bridge between two hydrophilic surfaces and even the value of R_K expected for our combination of a hydrophilic surface (the tip) and a hydrophobic surface (the graphite). This may indicate that either the Kelvin equation of the thermodynamic equilibrium of the condensate with the surroundings does not hold for nanoscopic capillary bridges [64] or that the liquid bridge that is stretched to the point of breaking is not in thermodynamic equilibrium. Indeed, Sirghi and colleagues report that the stretching of the meniscus causes a significant reduction of the meniscus curvature, which brings the meniscus noticeably out of thermodynamic equilibrium [73]. This shows that the evaporation rate of water under confinement is much reduced and it qualitatively explains the friction memory effect we observed in Fig. 6.3. This conclusion challenges the recently reported MD simulation results that a condensate readily evaporates from the confinement [74].

The average pull-off force over several different measurements is 7 nN. If F is the meniscus force of a liquid of surface tension γ , which wets the tip of contact radius r with a contact angle φ , then from the relation $F = 4\pi r \gamma \cos(\varphi)$, we may estimate the contact radius of the capillary bridge. Using values of $\gamma = 0.074$ N/m for water at 20° C, $\varphi = 40^\circ$ for the hydrophilic tungsten (oxide) tip, and substituting 7 nN for the meniscus force, we obtain an estimated contact radius of $r = 8.7$ nm.

6.7 Mechanical behavior and velocity dependence of the capillary condensate

One drawback of the FFM compared to the SFA is that we do not have a precise estimate of the thickness of the capillary condensate in our experiments. We have

to rely on the detection of forces under various experimental conditions. In this section, we investigate how capillary condensates behave at various RH values.

From the velocity dependence of friction at different relative humidities several aspects of the dissipation mechanism can be derived. Riedo *et al.* have shown that the velocity dependence at elevated RH values is entirely different on hydrophobic and hydrophilic surfaces [57,72]. They have found a logarithmic increase of friction with velocity for hydrophobic surfaces, which they ascribe to the effect of thermally activated, atomic-scale jumps of the type discussed in Chapter 3, i.e. in the absence of water. On the other hand, the same authors have found a logarithmic *decrease* of friction with velocity on a hydrophilic surface, which they associate with the thermally activated nucleation of capillary condensates between the sliding tip and the substrate. As mentioned before, with a contact angle of 86° , the HOPG substrate used in our experiments should be regarded as hydrophobic. At first sight, Fig. 6.5, which shows that friction between our tungsten tip and the HOPG surface increases with velocity at relative humidities of 1% (nominally dry) and 51%, seems to be in accordance with this picture.

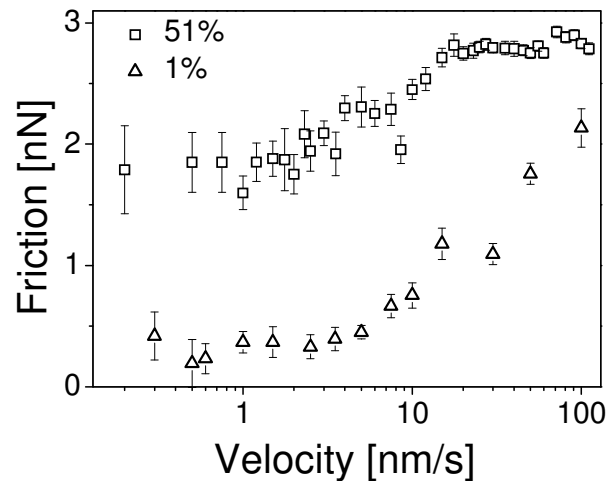


Fig. 6.5. Velocity dependence of friction between a tungsten tip and an HOPG surface at a low and a high relative humidity of 1% (nominally dry) and 51%.

However, the large difference between the friction values under dry and humid conditions cannot be explained in these simple terms. In addition, there is a

second, important difference, which is that we observe the HOPG lattice periodicity in the low-humidity lateral force signals and these atomic features are completely lost at high RH. Instead, we observe that the tip slides rather smoothly, but with higher dissipation. Therefore, we are forced to interpret the velocity dependence of the friction force at high humidity in terms of the visco-elastic properties of a water condensate that is intervening between the tip and the substrate, rather than thermally activated pre-critical jumps of the tip over the substrate lattice.

The absence of HOPG lattice features at high humidity is illustrated by Fig. 6.6, which shows four typical friction loops, measured at $\text{RH} = 51\%$ at four different scan velocities.

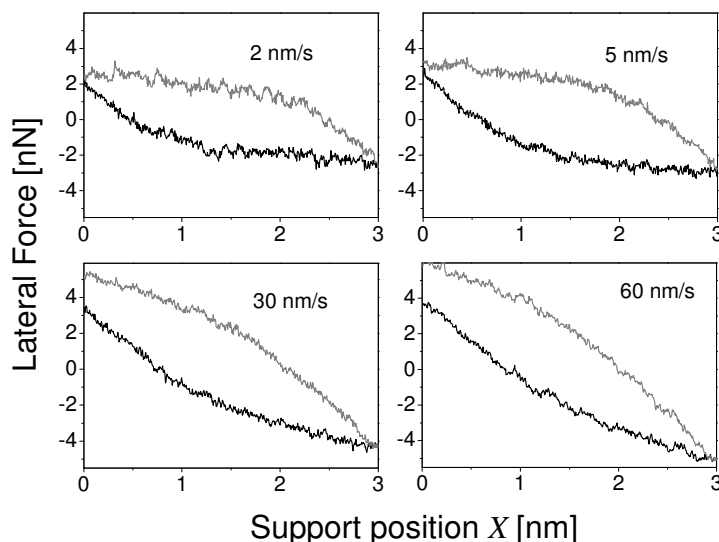


Fig. 6.6. Representative friction loops measured at four different scan velocities at a relative humidity of 51%. Unlike the ‘dry case’, no atomic features are identifiable in any of these loops. Note the velocity-dependent tilting of the dynamic parts of the loops. Also note that the higher-velocity force loops are not closed on the left-hand side. This is a slow relaxation process that we discuss further in the text.

These four lateral force loops are remarkably different from the more traditional force loops that were shown in Chapter 4 for the same velocity ranges under dry conditions ($\text{RH} = 1\%$). In addition to the absence of atomic features, there are two special features in Fig. 6.6 that become more pronounced as the velocity is increased. First of all, the entire force loops are tilted; in particular the

‘kinetic’ parts of the loop show a force that increases with traveled distance. The second feature is that the loop is not closed on the left-hand side, where the force relaxes during the 90 ms dead time of the data acquisition system. We will return to these special characteristics below, but stress here that both are completely absent under dry conditions ($RH = 1\%$), which suggests that their origin is associated with the presence of the capillary condensate between the tip and the substrate.

Having already noticed that the capillary condensate actually separates the tip from the substrate, we now present a simple scenario that accounts for the characteristics of the force loops at higher RH values. We presume that only a single capillary bridge is formed under the sharp tungsten tip, as sketched in Fig. 6.7 (A). The estimated tip radius is about 5 nm and we assume that the condensate size is roughly the same. Evidence for this condensate size comes from measurements with larger scan ranges that will be presented in Chapter 8. The scan range in Fig. 6.6 is only 3 nm.

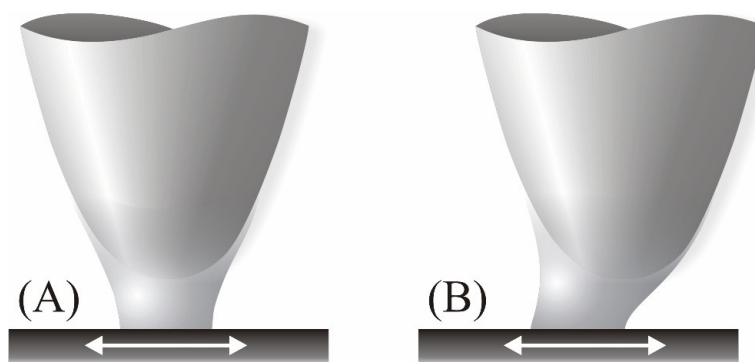


Fig. 6.7. (A) Cartoon of the equilibrium configuration of a capillary condensate in the tip-surface confinement (B) The shearing deformation of the condensate during scanning. The arrows in the substrates denote the 3 nm scan range.

If the condensate cannot translate easily over the substrate, the scanning motion will result in periodic distortions of the condensate, as illustrated in Fig. 6.7 (B). In the following we show that all aspects of the peculiar shape of the force loops can be associated completely with this shearing deformation of the condensate with respect to its equilibrium shape.

When the capillary condensate would behave as a viscous fluid, its response to the periodic forces exerted on it should depend on the frequency (velocity) of the scanning motion. By recording the in-phase (elastic) and out-of-phase (damping)

components of the shear response we should be able to completely characterize the viscous properties of the confined condensate [54].

Interestingly, the slope of the first part of each measured scan line (first ~ 1 nm) shows almost no dependence on scan velocity at all over several orders of magnitude in scan velocity. This can be seen in the right-hand panel of Fig. 6.8, where we show the corresponding spring constant of the condensate, which we obtained by correcting the measured slopes for the 6.1 N/m spring coefficient of the force sensor (see left-hand panel of Fig. 6.8). We will refer to these parts of the friction loops as the ‘static’ parts. The mere existence of a nearly purely static response implies that the condensate endures a finite yield stress, which is a signature that it mechanically behaves like a solid, rather than a liquid. In other words, the tip is ‘glued’ to the substrate by an ice-like capillary condensate.

We find that the spring constant of the condensate depends strongly on relative humidity; at RH = 50% it is 12 N/m and at 23% it is as high as 22.7 N/m. Assuming that the condensate is cylindrical with a diameter d of 5 nm and a height l of 0.802 nm (the Kelvin radius of the condensate at 50% relative humidity), we can estimate its Young’s modulus, using the expression [75]

$$Y = \frac{64kl^3}{3\pi d^4} \quad (6.4)$$

We find that Y is as high as 0.067 GPa at RH = 50% RH and 0.012 GPa at 23%. These estimates for the Young’s modulus of the condensate are substantial fractions of the value of this elastic constant of bulk ice, which is 9.9 GPa. Of course, one may dispute the appropriateness of this comparison between a bulk property of ice and the behavior of an ice-like, nano-scale condensate, which we estimate to contain only between a few hundred and a few thousand water molecules. Porter and Zinn-Warner have studied the Young’s modulus of ice bilayers and multilayers using mercury tunnel junctions and came to the conclusion that the Young’s modulus of ice bilayers is 0.134 GPa, which is well comparable to our estimates [76]. In addition, it is worth mentioning that water layers condensing on surfaces at lower RH values have been reported to have a more ordered ice-like structure than at higher relative humidities [77,78].

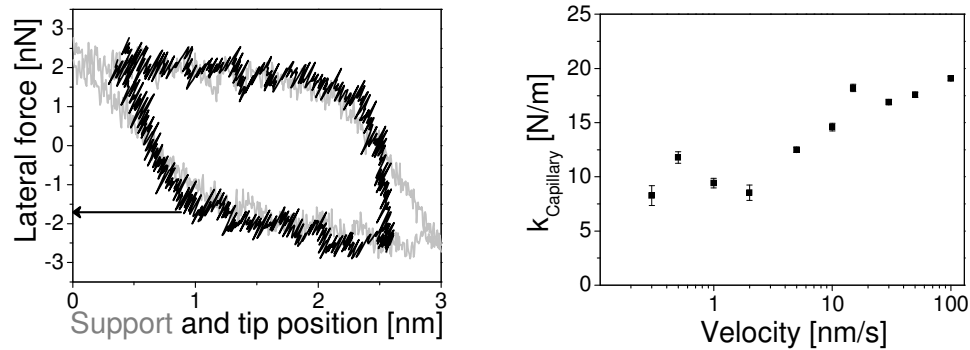


Fig. 6.8. Left: A typical friction loop, measured at $RH = 51\%$ at a velocity of 0.5 nm/s and displayed twice, namely as the lateral force against support position (grey curve) and against tip position (black curve). The arrow indicates the maximum shear stress up to which the condensate behaves elastically. **Right:** The slope of the static part of the force loops as a function of the scan velocity. The near absence of a velocity dependence shows that the condensate is effectively behaving as a solid.

We now turn to the transition to sliding, which takes place at a lateral of approximately 1.7 nN , a value that is again independent of the scan velocity. At this force, the condensate is elastically deformed by as much as 0.5 nm . When we again assume that the condensate has a diameter of 5 nm , we see that this critical shear force of 1.7 nN corresponds to a maximum shear stress of 90 MPa . This value is very close to the yield stress of bulk ice, which is of the order of 100 MPa .

At support displacements beyond 1 nm , i.e. at shear forces larger than 1.7 nN , the tip slides, which leads to actual energy dissipation (friction). However, since the force continues to increase (see Fig. 6.6), we know that the tip lags behind increasingly with respect to the support. This is a very unusual shape for an AFM lateral force loop, which is a direct signature of viscoelastic behavior, combining dissipative motion of the tip (viscous component of the behavior) with a simultaneous elastic response. Below, we will show that the slope of this part of the loop varies strongly with scan velocity, which we associate with the dependence of the competition between these elastic and viscous responses on the sliding timescale. We speculate that beyond the lateral force of 1.7 nN , the condensate is deformed, as sketched in Fig. 6.7 (B), which leads to the buildup of an additional elastic force, proportional to the tip displacement.

6.8 Effective viscosity of the capillary condensation

As discussed above, the parts of the friction loop near the turning points (‘static’ parts) have a slope that is almost completely insensitive to the scan speed, as should be the case for a solid medium. By contrast, the slope k_η of the central parts of the loop, during which the tip is really sliding (‘kinetic’ parts), depends strongly on velocity; it is described well by a power law, as is illustrated in Fig. 6.9. We associate this behavior with the capability of the condensate to rearrange itself, once it is sheared beyond its yield point. These rearrangements may concern the damage, inflicted by the shear motion, as well as the shape of the condensate and the size of its footprint on the substrate, all of which are probably brought out of equilibrium during the sliding motion. At slow scan speeds, the condensate can rearrange sufficiently to always stay close to its equilibrium shape, even though it is continually sheared to its yield stress. As a result, the lateral force no longer changes, once the tip has started to move. At high speeds the condensate is increasingly deformed towards the turning points in the friction loop, which leads to a lateral force that changes (increases) even after the tip has started to slide. The fact that we can observe this out-of-equilibrium signature at our low scan speeds (frequencies) indicates that the characteristic time for the rearrangements of the condensate is extremely long, which suggests that the rearrangements happen via slow processes, such as the diffusion of individual molecules in or over a solid, rather than rapid processes such as collective flow of a fluid.

Interestingly, the slopes of the two data sets in Fig. 6.9, i.e. the exponents of the corresponding two power laws, are different. For RH = 50% we have an exponent of roughly 1/3 and at RH = 23% we get approximately 1/2. This possibly means that the dominant mechanism for rearrangements of the condensate is different at the two humidities.

Formally, we may describe the power-law behavior in Fig. 6.10 with a viscous response, by re-plotting the data as an effective viscosity. This has been done in Fig. 6.10, which shows the effective viscosity (shear force divided by shear rate) against the shear rate (scan velocity divided by ‘film’ thickness obtained from the Kelvin radii of the condensate, which are 0.802 nm at 51% relative humidity and 0.367 nm at 23% relative humidity). To convert the slope of the kinetic part in to force, we multiplied it with a distance of 3 nm, which is the scan-range after which the kinetic force becomes constant, without tilting. This is assumed to be the

saturation value of the force which gives the maximum viscoelastic force. We see in Fig. 6.10 that the effective viscosity is not constant but it is a decreasing function of the shear rate ('shear thinning'). In principle, if the data would level off at low shear rates, Fig. 6.10 would allow us to deduce the intrinsic timescale of the dominant molecular relaxation mechanism (see below) as well as the intrinsic viscosity [15,17]. Over the three and a half orders of magnitude in shear rate of our experiment, we observe no leveling off of the effective viscosity. We should therefore regard the maximum effective viscosity of 10^8 Pa s in Fig. 6.10 as a lower estimate of the condensate's effective viscosity in the limit of slow shearing. Even though this is no more than a *lower* estimate, it is already as much as 10 orders of magnitude higher than the viscosity of water at room temperature (0.009 Pa s). However, our lower estimate is still 6 orders of magnitude below the viscosity of bulk ice (10^{14} Pa s) [79]. A very recent study demonstrates that the viscosity of water can increase 7 orders of magnitude compared to that of bulk liquid water under nano-confinement [39].

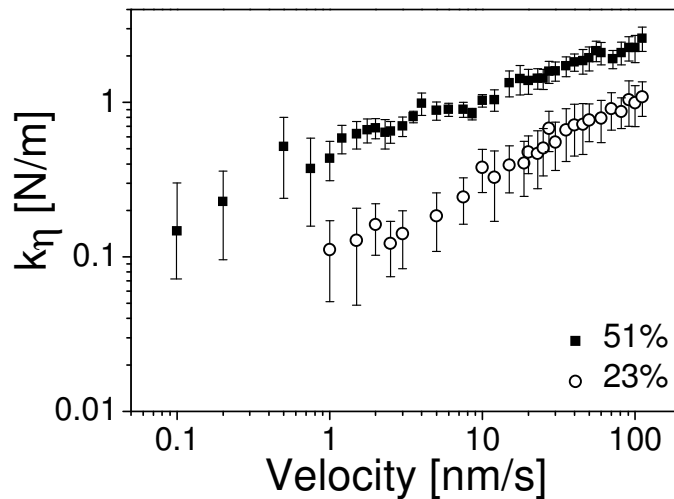


Fig. 6.9. Slope of the 'kinetic' parts of the friction loops plotted against scan velocity on a log-log scale for experimental data sets at $RH = 51\%$ and $RH = 23\%$.

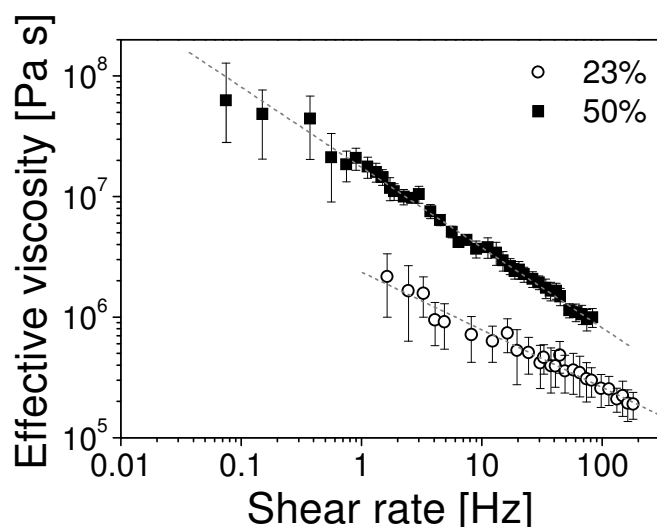


Fig. 6.10. A rough estimate of the effective viscosity of the condensate as a function of the shear rate on a log-log scale. The dotted grey lines are power-law fits.

Like in Fig. 6.9, the slopes of the two data sets in Fig. 6.10 are different; the condensate at 50% following a $2/3^{\text{rd}}$ power law and the condensate at 23% obeying a $1/2^{\text{nd}}$ power law. Demirel and Granick have reported a $2/3^{\text{rd}}$ power law for OMCTS molecules confined between two mica sheets and this has been ascribed to the collective motion in a liquid with partial molecular ordering [15].

The absence of a plateau in the effective viscosity in Fig. 6.10 tells us that all shear rates in this figure are faster than the rate of the dominant relaxation mechanism of the condensate. In other words, the characteristic time of the condensate must be longer than the inverse of the minimum shear rate in Fig. 6.10, which is as long as 4 s. This relaxation time is many orders of magnitude longer than the timescale of picoseconds, known for molecular relaxation of bulk water [80].

6.9 Relaxation timescale of the condensate – additional evidence

As mentioned above, one of the special features in Fig. 6.6 is that the force loops are not closed on the left hand side, an effect that grows with increasing velocity. This is a combination of the relaxation of the condensate and a well-defined timing artifact of the measurement. Each force loop is composed of a constant-velocity

forward part (from left to right), immediately followed by a constant-velocity (same velocity) reverse part (from right to left). Before the start of the next force loop, our scan generator and data acquisition system has a constant waiting time of 90 ms, as is shown in Fig. 6.11. During this time, the support moves a small distance (one line spacing) in the slow scan direction ('Y-direction') and the recorded force loop data is stored on hard disk. If the lateral force relaxes during this 90 ms 'dead time', the next force loop will start at a lower force than that at which the previous force loop ended.

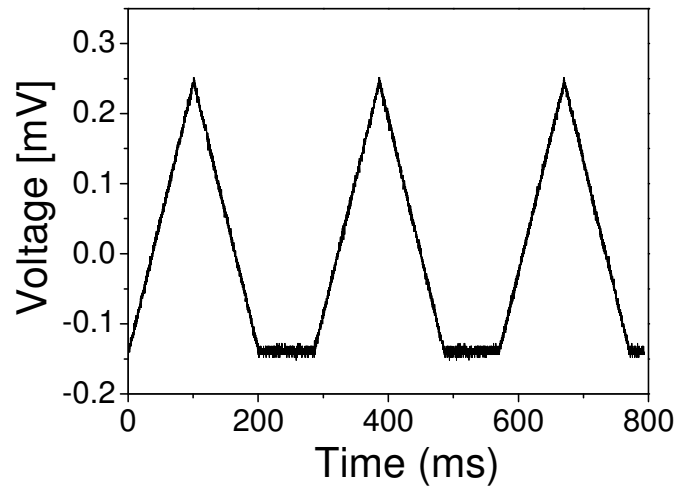


Fig. 6.11. Wave form used for recording lateral force loops (corresponding to 3 nm scan range). Note the (constant) dead time of 90 ms between the end of each force loop and the start of the next one.

We can exploit this effect and measure the dependence of the drop in lateral force ΔF on the force F_0 at the beginning of the 90 ms waiting period. If the force would decay exponentially from its starting value F_0 to an asymptotic value of F_l with a time constant τ , the force reduction ΔF within the fixed waiting period Δt should be

$$\Delta F = (F_0 - F_l) [1 - \exp(-\Delta t/\tau)] . \quad (6.5)$$

Note that the factor between square brackets is a constant that depends on the fixed waiting time of $\Delta t = 90$ ms and the unknown time constant τ . Let us assume that F_l is really constant and that F_0 can be varied by the scan speed. A plot of the ratio ΔF against F_0 should thus result in a straight line with a slope $[1 - \exp(-\Delta t/\tau)]$ that

intersects the horizontal axis at $F_0 = F_1$. Indeed, the data in Fig. 6.13 can be described well by a straight line with a slope of 0.60, corresponding to $\tau = 98$ ms, and with an intersection at $F_1 = 2.0$ nN. Again we find a very long relaxation time. The asymptotic force of 2.0 nN is very close to the 1.7 nN at which the tip starts to slide, which clearly shows that the force relaxation does *not* apply to the static component of the force but it is restricted to the additional force, built up during the dynamic part of the friction loop.

The left panel of Fig. 6.12 shows the relation between ΔF and the sweep time (time for one scan line). It cannot be described by an exponential or a power law. Instead we can fit it with a simple theory. We assume that the following differential equation is at work for the build-up and decay of the additional lateral force, which is added to the ~ 1.7 nN of static yield force of the condensate:

$$\frac{dF}{dt} = a \frac{dx}{dt} - \frac{F}{\tau} \quad (6.6)$$

In other words, we assume that the additional force grows has an intrinsically elastic character. It increases proportionally to the displacement. But it is simultaneously relaxes exponentially, i.e. at a rate proportional to the additional force itself, as we have already verified (Fig. 6.13 right panel). We can rewrite the equation as:

$$\frac{dF}{dx} = a - \frac{F}{\tau v}, \quad (6.7)$$

where v is the scan speed. The solution is:

$$F(x) = a\tau v \left[1 - \exp\left(-\frac{x}{\tau v}\right) \right]. \quad (6.8)$$

This shows an initially linear build-up of force with sliding distance, which levels off at a final value of $a\tau v$. However, we have been performing measurements for very short scan widths (3 nm) so that we have seen mostly the initial, almost linearly increasing part. What I have plotted in the excel sheet is the force built up over the width of the sweep $F(L)$, where L is the scan width (3 nm). The left panel of Fig. 6.13 shows the part ΔF of this force that is relaxed during the 90 ms dead time following the scan. However, since this decay is again exponential, the force change ΔF is a fixed fraction of the force itself $\Delta F = F(L)\exp(-\Delta t/\tau)$. Of course, the characteristic time τ in this decay should be the same as the one used above. Apart from this fixed factor the sweep time or velocity dependence of ΔF

should be precisely the same as calculated here for the full dynamic force of $F(L)$. The fit in the left panel of Fig. 6.12 shows that Eqn. (6.8) is consistent with our observations. We obtain acceptably good fits for relaxation times between 35 ms and 100 ms, which is in the same order of magnitude as the 98 ms coming from the relation between ΔF and $F(L)$ in the right-hand panel of Fig. 6.12. For the constant a we find, after the factor 2.5 correction for the difference between looking directly at $F(L)$ and looking at ΔF , values between 1.5 N/m and 2.8 N/m. This range of values is in the order of magnitude of the maximum slope of ~ 2.5 N/m that we have found at RH = 51% in Fig. 6.9. The nicest fit is obtained for $\tau = 55$ ms and $a = 2.0$ N/m (see right panel of Fig. 6.12).

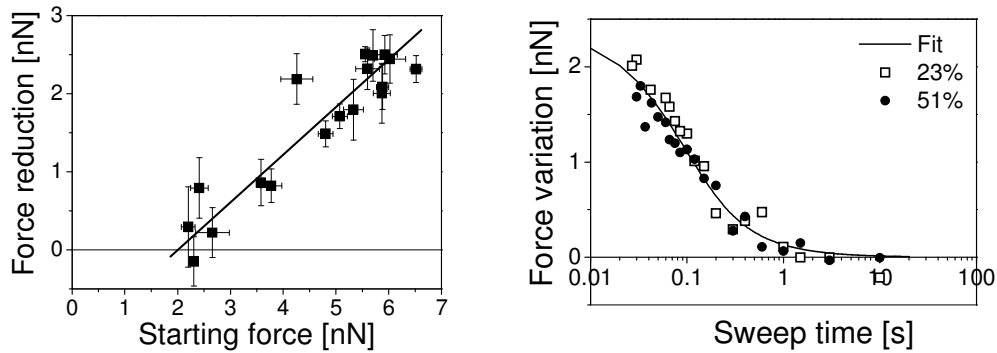


Fig. 6.12. **Left:** Force reduction ΔF during the 90 ms dead time against the maximum force F_0 at the start of the dead time. The linear relation shows that the force reduces exponentially with a characteristic time of 98 ms to a final value of 2.0 nN, measured at RH = 51%. **Right:** Force reduction ΔF during the 90 ms dead time versus the sweep time (time to scan one line), measured at RH = 51% (filled circles) and at 23% (squares). The curve shows the fit according to the model discussed in the text for a relaxation time of $\tau = 55$ ms.

6.10 A simple scenario to explain the tilting of the force loops

As Eqn 6.6 suggests, the additional lateral force that increases as a function of the support position, is velocity dependent. Consider the capillary condensate in an equilibrium shape as shown in Fig. 6.13A. When the support moves forward, the condensate deforms elastically until the lateral force reaches the yield stress of the ice at around $X = 0.5$ nm, as shown in Fig. 6.13B. Beyond this value of the lateral

force, the condensate slips and a highly non-equilibrium shape results, as indicated in Fig. 6.13C. We expect that the two highly curved, concave regions (one on each side of the condensate) are rapidly filled up with water condensing from the environment, thus increasing the cross-sectional area of the ice condensate (Fig. 6.13D). In the simplest approximation, the additional area grows proportionally to the displacement of the tip. This increase in area of the condensate should increase the lateral force required to break the condensate again, which makes the lateral force increase linearly with the support position. There are several restoring mechanisms at work to bring the condensate back into its equilibrium shape and size, such as diffusion of water molecules over the condensate surface and evaporation plus recondensation of water molecules. Whereas the addition of water from the vapor can be a very rapid process, the timescales for evaporation and other forms of rearrangement of the condensate are very long, as is demonstrated in this chapter and the next one.

With a simple calculation, we can estimate the additional area of the condensate. Figure 6.14 shows a schematic cross-sectional view of the condensate after the tip has moved over the full scan width (shape as in Fig. 6.13D). The shaded portion represents the additional area of the condensate formed during scanning over the range L and the rounded parts with a radius R form together the original area of the equilibrium shape of the ice condensate. We assume that the velocity has been sufficiently slow for the additional water (ice) to have condensed during the scan, but sufficiently fast to have avoided rearrangements of the condensate completely. Thus, the total area of the condensate would be $A = \pi R^2 + 2LR$. Compared to the equilibrium area of $A_0 = \pi R^2$ there is an increase

in area, and therefore also an increase in lateral force by a factor $\frac{A}{A_0} = 1 + \frac{2L}{\pi R}$. We

compare this simple description, which completely ignores the rearrangements of the condensate, with some of our highest-velocity measurements, e.g. the one in Fig. 6.6 at 60 nm/s. The ratio between the final lateral force at the end of the scan line and the lateral force at which the tip starts to move is approximately 2, from which we find that $R = 2L/\pi = 2nm$.

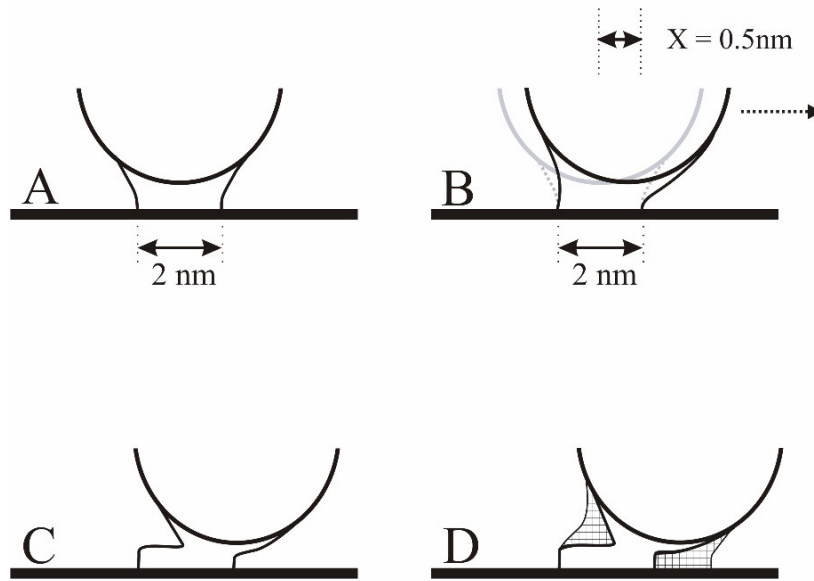


Fig. 6.13. Cartoons showing the scenario to explain the tilting of the force loops. (A) Equilibrium shape of the condensate under the tip, (B) bending of the condensate in the elastic regime of the tip displacement (≤ 0.5 nm), (C) slipping of the ice when the lateral force exceeds the yield stress of the condensate and (D) condensation of additional ice in the exposed areas of the condensate.

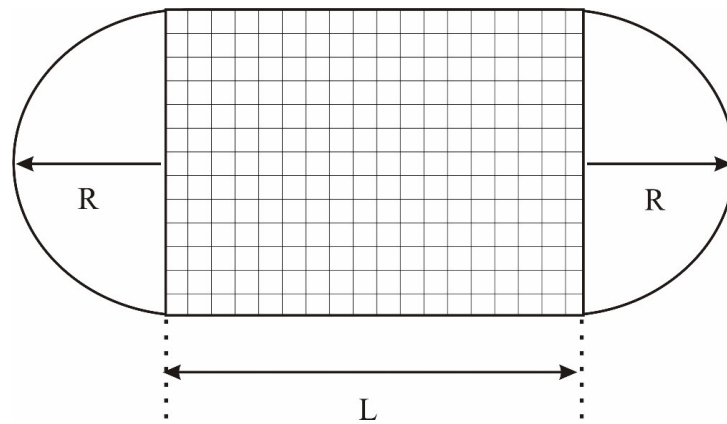


Fig. 6.14. Schematic cross section of the condensate. The shaded portion is the additional area introduced by scanning over a length L . In all measurements in this chapter $L = 3$ nm. The circular part with radius R represents the area of the original, equilibrium cross section of the condensate.

6.11 Conclusions

In this chapter, we have studied the behavior of the capillary condensate forming between a hydrophilic tungsten tip and a hydrophobic HOPG surface at different relative humidities. To our surprise, the capillary condensate behaves mechanically like a solid, exhibiting static friction, which is a signature of a finite yield stress. The yield stress estimated for the condensate is comparable to that of bulk ice. Mechanically, the capillary condensates at RH values of 23% and 51% behave differently, showing different values of the friction force and exhibiting a somewhat different relaxation dynamics, which might be an indication that the condensates have different structures or follow different relaxation mechanisms. The higher estimate for the Young's modulus of the condensate at RH = 23%, compared to 51% might indicate that the condensate is more crystalline and therefore stronger at the lower RH.

A rough lower estimate of the effective viscosity of the condensate at RH = 50% is 10 orders of magnitude higher than the viscosity of water. The relaxation timescales for the rearrangement of a distorted condensate is estimated to be nearly 4 seconds, which is many orders of magnitude larger than the typical molecular rearrangement timescales of bulk liquid water. This exploding timescale is taken as a symptom of a high degree of ordering of the molecules in the confinement between the tip and the surface. Relaxation timescales of the condensate can be estimated in various ways, for instance by observing the relaxation of the tip in the condensate, and from each observation we conclude that the condensate rearranges on a very long timescale of the order of seconds.

The essence of the conclusions drawn from these experiments is that the condensate behaves more like ice than like a fluid. Further experiments are necessary to investigate whether this confinement induced solidification of water at room temperature is sensitive to different combinations of interfaces. Extremely slow experiments, well below the relaxation timescale of the condensate provide us with more insight into the structural and mechanical properties of the capillary bridge formed under similar circumstances. These aspects shall be discussed in the next chapter.



6.12 References:

1. M. Urbakh, J. Klafter, D. Gourdon, J.N. Israelachvili, *Nature* **430**, 525 (2004).
2. M. Faraday, *Experimental researches in Chemistry and Physics*, Taylor and Francis, London (1859), page 372.
3. R. Rosenberg, *Physics Today* **58**, 50 (2005).
4. N. Kawai *et al.*, *J. Biomed. Mater. Res.* **70A**, 149 (2004).
5. L. Bocquet, E. Charlaix, S. Ciliberto, J. Crassous, *Nature* **396**, 735 (1998).
6. D. Broseta *et al.*, *Phys. Rev. Lett.* **86**, 5313 (2001).
7. Y.Q. Song, S. Ryu, P.N. Sen, *Nature* **406**, 178 (2000).
8. S Karaborni, B Smit, W Heidug, J Urai, E van Oort, *Science* **271**, 1102 (1996).
9. A.L. Demirel, S. Granick, *J. Chem. Phys.* **109**, 6889 (1998).
10. B.N.J. Persson, *Sliding friction – Physical principles and applications*, Ed.2, Springer, Berlin (1998), page 140.
11. P.A. Thompson, M.O. Robbins, *Phys. Rev. A* **41**, 6830 (1990).
12. P.A. Thompson, G.S. Grest, M.O. Robbins, *Phys. Rev. Lett.* **68**, 3448 (1992).
13. M. Schoen, C.L. Rhykerd Jr., D.J. Diestler, J.H. Cushman, *Science* **245**, 1223 (1989).
14. J.H. Cushman, *Nature* **347**, 227 (1990).
15. A.L. Demirel, S. Granick, *Phys. Rev. Lett.* **77**, 2261 (1996).
16. A.L. Demirel, S. Granck, *J.Phys.: Condens. Matter* **8**, 9537 (1996).
17. S. Granick, *Science* **253**, 1374 (1991).
18. M.L. Gee, P.M. McGuiggan, J.N. Israelachvili, A.M. Homola, *J. Chem. Phys.* **93**, 1895 (1990).
19. A. Mukhopadhyay, J. Zhao, S.C. Bae, S. Granick, *Phys. Rev. Lett.* **89**, 136103 (2002).
20. D. Gourdon, J.N. Israelachvili, *Phys. Rev. E* **68**, 21602 (2003).
21. O.M. Braun, M. Peyrard, *Phys. Rev. E* **63**, 46110 (2001).
22. O.M. Braun, M. Paliy, S. Consta, *Phys. Rev. Lett.* **92**, 256103 (2004).
23. J. Gao, W.D. Luedtke, U. Landmann, *Phys. Rev. Lett.* **79**, 705 (1997).
24. B. Bhushan, J.N. Israelachvili, U. Landman, *Nature* **374**, 607 (1995).
25. M.O. Robbins, P.A. Thompson, *Science* **250**, 792 (1990).
26. M.O. Robbins, P.A. Thompson, *Science* **253**, 916 (1991).
27. O.M. Braun, M. Peyrard, *Phys. Rev. E* **68**, 11506 (2003).
28. J.N. Israelachvili, P.M. McGuiggan, A.M. Homola, *Science* **240**, 189 (1988).
29. T. Becker, F. Mugele, *Phys. Rev. Lett.* **91**, 166104 (2003).

30. S.T. Cui, C. McCabe, P.T. Cummings, H.D. Cochran, *J. Chem. Phys.* **118**, 8941 (2003).
31. F. Mugele, M. Salmeron, *Phys. Rev. Lett.* **84**, 5796 (2000).
32. H.K. Christenson, *Chem. Phys. Lett.* **118**, 455 (1985).
33. T.K.S.L.E van der Lick, H.T. Davis, *Colloids Surf.* **52**, 9 (1991).
34. R.M. Pashley, J.N. Israelachvili, *J. Colloid Interface Sci.* **101**, 511 (1984).
35. P.D. Ashby, *Intermolecular and interfacial forces: Elucidating molecular mechanisms using chemical force microscopy*, PhD Thesis, Harvard University, USA, 2003.
36. Y. Zhu, S. Granick, *Phys. Rev. Lett.* **87**, 96104 (2001).
37. X. Zhang, Y. Zhu, & S. Granick, *Science* **295**, 663 (2002).
38. U. Raviv, J. Klein, *Science* **297**, 1540 (2002).
39. R.C. Major, J.E. Houston, M.J. McGrath, J.I. Siepmann, X.-Y. Zhu, *Phys. Rev. Lett.* **96**, 177803 (2006).
40. U. Raviv, P. Laurat, J. Klein, *Nature* **413**, 51 (2001).
41. J.N. Israelachvili, *J. Colloid Interface Sci.* **110**, 263 (1986).
42. R.G. Horn, D.T. Smith, W. Haller, *Chem. Phys. Lett.* **162**, 404 (1989).
43. A. Dhinojwala, S. Granick, *J. Am. Chem. Soc.* **119**, 241 (1997).
44. H. Sakuma, K. Otsuki, K. Kurihara, *Phys. Rev. Lett.* **96**, 46104 (2006).
45. O.M. Braun (Institute of Physics, National Academy of Sciences, Ukraine), Personal communications 2005.
46. U. Raviv, S. Giasson, J. Frey, J. Klein, *J. Phys.: Condens. Matter* **14**, 9275 (2002).
47. Y. Zhu, S. Granick, *Langmuir* **19**, 8148 (2003).
48. J.N. Israelachvili, N. Maeda, M. Akbulut, *Langmuir* **22**, 2397 (2006).
49. S. Granick, Y. Zhu, Z. Lin, S.C. Bae, J.S. Wong, J. Turner, *Langmuir* **22**, 2399 (2006).
50. S.J. O'Shea, M.E. Welland, J.B. Pethica, *Chem. Phys. Lett.* **223**, 336 (1994).
51. A. Maali, T.C. Bouhacina, G. Couturier, J.P. Aimé, *Phys. Rev. Lett.* **96**, 86105 (2006).
52. R.Y.H. Lim, S.J. O'Shea, *Langmuir* **20**, 4916 (2004).
53. R.W. Carpick, M. Salmeron, *Chem. Rev.* **97**, 1163 (1997).
54. M. Antognozzi, A.D.L. Humphris, M.J. Miles, *Appl. Phys. Lett.* **78**, 300 (2001).
55. S.P. Jarvis, T. Uchihashi, T. Ishida, H. Tokumoto, Y. Nakayama, *J. Phys. Chem. B* **104**, 6091 (2000).

-
56. S. Jeffery, P.M. Hoffmann, J.B. Pethica, C. Ramanujan, H.O. Özer, A. Oral, *Phys. Rev. B* **70**, 54114 (2004).
57. E. Riedo, F. Lévy, H. Brune, *Phys. Rev. Lett.* **88**, 185505 (2002).
58. J.N. Israelachvili, *Intermolecular and surface forces*, Ed. 2, Academic Press Inc., San Diego (1992), page 330.
59. J. Jang, G.C. Schatz, M.A. Ratner, *Phys. Rev. Lett.* **92**, 85504 (2004).
60. A.W. Adomson, *Physical Chemistry of Surfaces*, Interscience Publishers, New York, 1960, page 56.
61. E. Meyer, R.M. Overney, K. Dransfeld, T. Gyalog, *Nanoscience: friction and rheology on the nanometer scale*, World Scientific Publishing, Ed. 1 (1998), page 103.
62. J.L. Parker, P.M. Claesson, P. Attard, *J. Phys. Chem.* **98**, 8468 (1994).
63. M. Schenk, M. Füting, R. Reichelt, *J. Appl. Phys.* **84**, 4880 (1998).
64. B.L. Weeks, M.W. Vaughn, J.J. DeYoreo, *Langmuir* **21**, 8096 (2005).
65. R.D. Piner, J. Zhu, F. Xu, S. Hong, C.A. Mirkin, *Science* **283**, 661 (1999).
66. M. Binggeli, C.M. Mate, *Appl. Phys. Lett.* **65**, 451 (1994).
67. B. Cappella, G. Dietler, *Surf. Sci. Rep.* **34**, 1 (1999).
68. Y.L.E. Chen, M.L. Gee, C.A. Helm, J.N. Israelachvili, P.M. McGuiggan, *J. Phys. Chem.* **93**, 7057 (1989).
69. H. Bock, D.J. Diestler, M. Schoen, *Phys. Rev. E* **64**, 46124 (2001).
70. J. Crassous, L. Bocquet, S. Ciliberto, C. Laroche, *Europhys. Lett.* **47**, 562 (1999).
71. E. Riedo, E. Gnecco, *Nanotechnology* **15**, S288 (2004).
72. E. Riedo, I. Pallaci, C. Boragno, H. Brune, *J. Phys. Chem. B* **108**, 5324 (2004).
73. L. Sirghi, R. Szoszkiewics, E. Riedo, *Langmuir* **22**, 1093 (2006).
74. K. Leung, A. Luzar, D. Bratko, *Phys. Rev. Lett.* **90**, 65502 (2003).
75. W.D. Pilkey, *Formulas for stress, strain and structural matrices*, Wiley-Interscience (1994).
76. J.D. Porter, A.S. Zinn-Warner, *Phys. Rev. Lett.* **73**, 2879 (1994).
77. M. Luna, J. Colchero, A.M. Baró, *J. Phys. Chem. B*, **103**, 9576 (1999).
78. P.B. Miranda, L. Xu, Y.R. Shen, M. Salmeron, *Phys. Rev. Lett.* **81**, 5876 (1998).
79. J.P. Poirier, C. Sotin, J. Peyronneau, *Nature* **292**, 225 (1981).
80. A.W. Omta, M.F. Kropman, S. Woutersen, H.J. Bakker, *Science* **301**, 374 (2003).

Chapter 7

Ice formation at room temperature and new physical phenomena in atomic friction

We present direct evidence for ice formation at room temperature in atomic-scale friction experiments. At modest relative humidities and ultra-low velocities, the lateral force loops measured with a tungsten tip sliding over a graphite surface exhibit a pronounced stick-slip period of 0.4 nm, which we ascribe to the ice lattice. We discuss the behavior of lateral force loops at different humidities and scan velocities, which we combine into a single humidity-velocity diagram. In this diagram we identify a variety of regimes, which we interpret in terms of dry friction, crystalline ice formation and the formation of less ordered ice.

7.1 Introduction

Water adsorbed on surfaces forms a subject of ongoing controversy. According to several reports in the literature, when water adsorbs on a smooth surface, the molecules adjust themselves to form a stable and energetically favorable configuration of a highly ordered hydrogen bonded network [2-6]. At room temperature, this layering and surface-induced ordering may be expected to occur up to a distance (correlation length) of one or two monolayers from the interface with the smooth substrate, beyond which the structural properties are more like those of bulk liquid water than like a solid form of water. However, while the molecules would lower their potential energy by adsorbing on the substrate in an ordered structure, they should pay the price of also lowering their translational entropy. Water is notorious for its high translational entropy. This is one of the reasons why other research groups claim that ordering is prohibited unless the interaction with the substrate is strongly imposing such order [1]. This conflicting view seems to be confirmed by some SFA experiments of water confined between mica surfaces.

Several experiments have recently been reported that show that water does form ice-like interfacial monolayers on atomically smooth surfaces that are immersed in water. For instance, surface X-ray diffraction measurements show the presence of an ice-like monolayer with a lattice similar to that of bulk ice at the interface between water and a RuO_2 (110) plane [7]. Sum frequency generation studies provide further evidence that water forms ice-like monolayers also on quartz and mica surfaces [2,6,8].

In FFM experiments, the confinement between the tip and the surface makes it extra favorable for water to become ordered at temperatures above 0°C . One may view the interface with the tip as a second surface that tends to order one or two monolayers of water similar to what the substrate does. In Fig. 7.1 we show tapping-mode images that indicate that water can adsorb on graphite even without confinement, for example as nano-droplets at defect lines and step edges. Such nanoscale clusters have been reported to exhibit ice-like order [5,6]. Molecular dynamics (MD) simulations predict that water confined in hydrophobic slit pores undergoes a first-order phase transition from liquid to solid at temperatures significantly higher than the melting points at different pressures [9]. Even under the confinement between hydrophobic surfaces, persisting in the liquid state is

energetically more expensive than ordering into a regular, hydrogen-bonded network [10]. There have been extensive MD simulations on the confinement-induced solidification of water between hydrophobic surfaces [11] and in particular, related to water condensation and transport properties in carbon nanotubes [12-14].

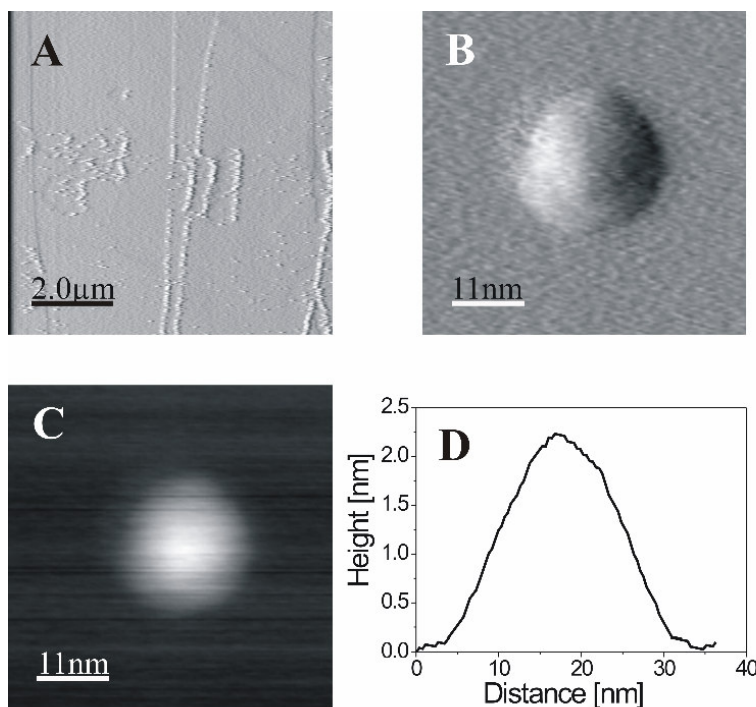


Fig 7.1 Adsorption of water and spontaneous nucleation of condensates on graphite at elevated RH values (~80%) imaged with tapping mode AFM (MultiMode™). (A) Water islands decorating step edges and defect lines on graphite; (B) amplitude image of a single water nanodroplet on graphite; (C) height image of the same droplet and (D) a cross-section of image C, showing that the water droplet is 2 nm high.

In the previous chapter we have already provided evidence that the capillary water condensate between a tungsten tip and a graphite surface shows mechanical behavior that is more like that of a solid than a liquid. This is reflected in the elastic response of the condensate to small distortions, the high yield stress and the extremely long relaxation times, observed when the condensate is deformed beyond its yield point. In the present chapter we explore other properties of the capillary condensate, providing further, conclusive evidence that the condensate tends to

form *crystalline* ice, when given sufficient time. We further the effects of this icy condensate on the atomic-scale friction between the tungsten tip and the graphite surface at a range of humidities and scan velocities and find a surprisingly wide variation in friction behavior.

7.2 Velocity dependence of friction at different relative humidities

The experiments presented in this chapter were again obtained with a tungsten tip on an HOPG surface, using a Tribolover with a lateral spring constant of 6.1 N/m and a normal spring constant of 30.5 N/m. All measurements were performed at a constant normal force of 3.7 nN. The extremely long relaxation timescales, in the order of seconds, reported in the previous chapter, should give rise to a strong velocity dependence of the friction force, especially at ultra-low velocities of, for example, 1 nm/s. Figure 7.2 shows the velocity dependence of friction over three orders of magnitude in the velocity, at four different values of the relative humidity. These friction values were obtained from scans with a size of 3 nm \times 3 nm.

An interesting feature of the velocity dependence of friction at different RH is the behavior at ultra-low velocities. At the lowest humidity of 1%, corresponding to our nominally ‘dry’ conditions, the friction force increases monotonically (logarithmically) with increasing velocity (Fig. 7.2a). This is the signature of thermal jumps, as we discussed in Chapter 4. A similar monotonic trend is observed at RH = 51%, albeit at a higher friction level at all velocities than the 1% data (Fig. 7.2d). As we argued in Chapter 6, the velocity dependence at 50% has a different origin, which directly reflects the relaxation dynamics of the deformed capillary condensate between the moving tip and the substrate. The velocity dependence at the two intermediate RH values (Figs. 7.2b,c) is strikingly different. In addition to the increase of friction with velocity, which is still observed at higher velocities, there is an intriguing, significant increase of the friction force when the velocity is decreased to ultra-low values. The width of this special, low-velocity regime depends on the humidity, it runs to approximately 3 nm/s at RH = 5% and to 2 nm/s at RH = 26%.

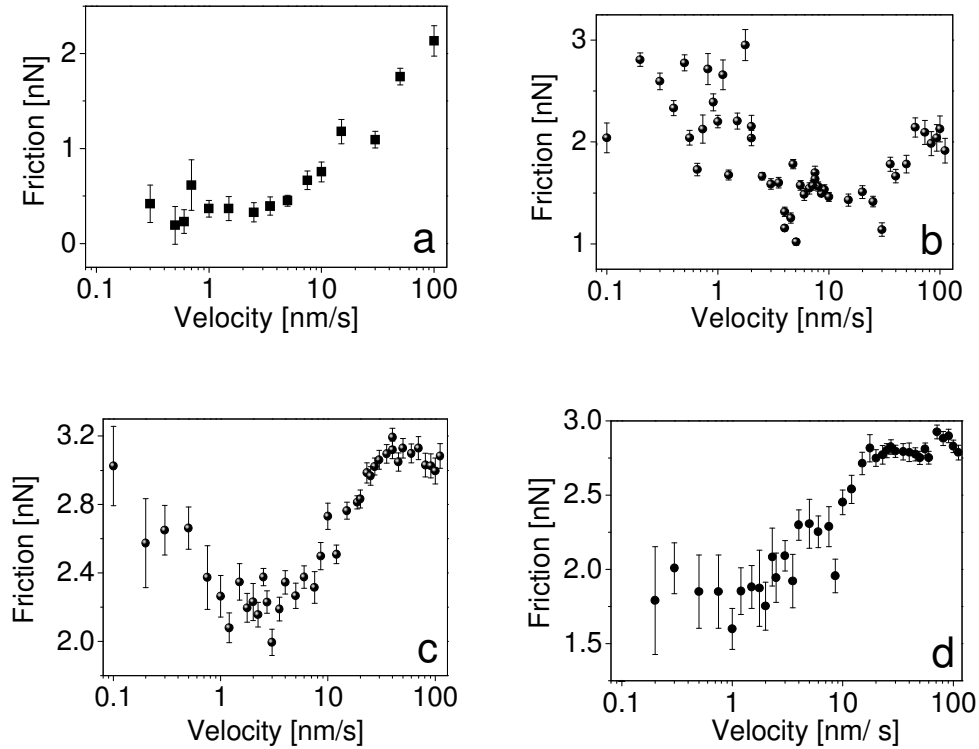


Fig. 7.2. Velocity dependence of friction at four different relative humidities: (a) 1%, (b) 5%, (c) 26% and (d) 51%. The lowest RH value of 1% corresponds to the driest conditions that we have been able to set. At 1% and 51%, the friction force varies monotonically with velocity, starting from a constant value at low velocities. By contrast, at intermediate RH values, the friction force shows a significant increase when the velocity is reduced below 1 nm/s.

A closer look at the lateral force loops measured at different scan velocities at intermediate relative humidities (5% to 33%) provides us with further details of this unusual, low-velocity increase in dissipation. The force loops in which we measure the increased friction force at low velocities all look like the ones reproduced in Figs. 7.3a,b for RH = 5% (results at other humidities in this intermediate range are very similar).

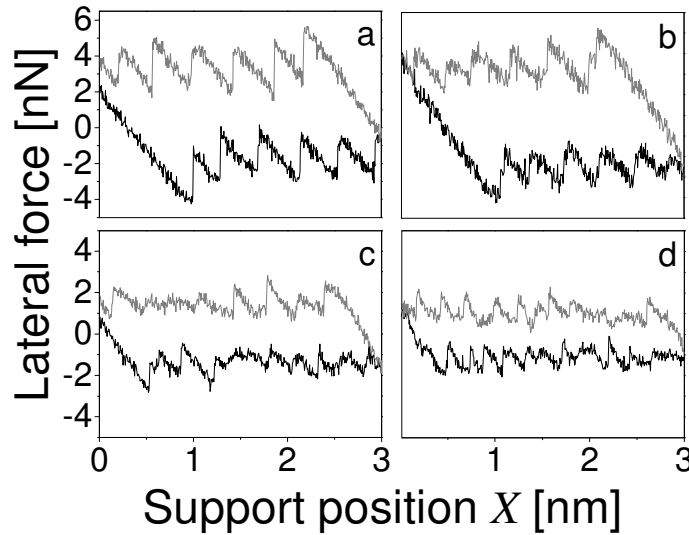


Fig. 7. 3. Typical force loops at 5% relative humidity, acquired at velocities of (a) 0.1 nm/s, (b) 3 nm/s, (c) 10 nm/s and (d) 30 nm/s.

The nature of the low-velocity force loops at 5% relative humidity is strikingly different from what we always observed (before and after the higher-humidity experiments) at the same, low velocities at RH = 1%. Under dry conditions we observed for low velocities the thermolubric regime, with multiple backward and forward jumps of the tip between neighboring potential wells of the interaction with the graphite surface (Chapter 4), and a corresponding, dramatic reduction of the friction force to a near-zero value. But at these same velocities, when we introduce water vapor up to a modest humidity of 5%, the friction loops exhibit a very pronounced stick-slip signature with dramatically high dissipation. One spectacular aspect of this observation is the completely unexpected period of the stick-slip motion at low velocities, which does not correspond to the lattice structure of the graphite substrate and which shows no dependence on the precise scan velocity and humidity (see below). When the scan velocity is increased slightly to 3 nm/s, the stick-slip character becomes less pronounced and more irregular (Fig. 7.3b). At even higher velocities, e.g. at 10 nm/s, a very irregular stick-slip pattern is observed (Fig. 7.3c). At even higher scan velocities, a new, more or less regular pattern emerges with a periodicity consistent with that of the graphite lattice (Fig. 7.3d).

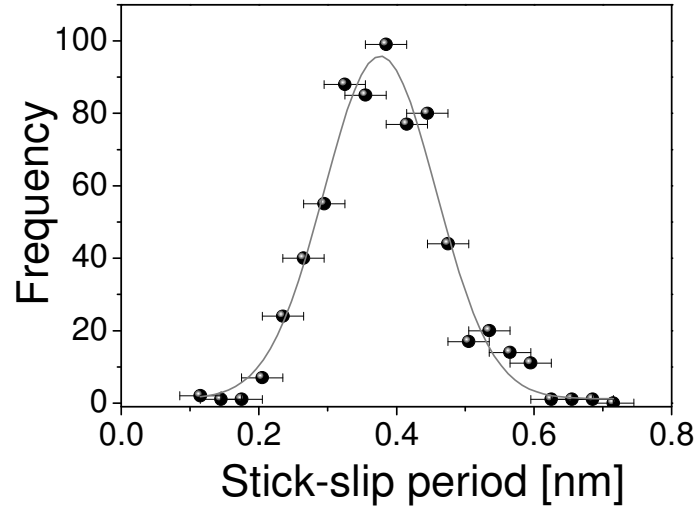


Fig. 7.4. Distribution of the stick-slip period observed at ultra-low velocities, at intermediate relative humidities (5%-33%). The distribution gives an average value of 0.38 ± 0.01 nm.

Figure 7.4 shows the distribution of stick-slip distances measured from these peculiar friction loops. The average stick-slip period measured from this distribution is 0.38 ± 0.01 nm. Within our statistics this value is independent of the velocity and the humidity. This period has no correlation with the structure of the graphite lattice. These strong, long-period stick-slip instabilities are observed exclusively at nonzero RH values (remember that 1% is our detection level, corresponding to a nominally dry chamber). Similar to the low-velocity increase in friction, also the stick-slip motion with the well-defined, long period is observed at higher humidities up to lower velocities than at 5%; for example, up to 1.5 nm/s at 26% and up to 0.5 nm/s at 33%. The re-entry of the graphite lattice at high velocities was seen only at RH = 5% and not at the higher humidities.

Since the low-velocity, long-period stick-slip process was seen only at non-zero relative humidities, we directly conclude that it is a consequence of capillary condensation between the tip and the graphite surface. In the previous chapter, we have already concluded that the confined geometry between tip and surface easily leads to capillary condensation and that the condensate behaves more like a solid than a liquid [4,15]. We now argue that the unusual repeat distance observed here

actually reflects the period of the lattice of the ice-like condensate. In Chapter 6 we had already concluded that the shear force exerted by the support leads to tip motion when the shear stress on the condensate exceeds a value close to the yield stress of bulk ice. This indicates that the condensate is not sheared as a single unit over the graphite or, alternatively, over the tip, but that one part of the ice remains attached to the substrate while the remainder stays attached to the tip. In this picture, the slipping actually takes part in the ice itself. The disorder introduced temporarily in the lattice of a piece of perfectly crystalline ice when it is sheared beyond the yield point can be viewed as a form of ‘shear-induced melting’. When given enough time, the damage inflicted upon the perfect crystal structure will anneal out, as a result of diffusion of the point defects (vacancies and interstitials) and dislocations in the ice. If this is the case, every slip event should start from a perfect crystal and the shear force should exhibit a stick-slip modulation with the periodicity of the ice lattice. This is our explanation for our observation of the ice lattice period at ultra-low scan velocities. In other words, we associate the 0.38 nm period with the lattice constant of the ice-like condensate (see below). As the scan velocity is increased, the crystal defects in the ice are given less and less time to anneal out, which reduces the quality of the ice lattice, which, in turn, leads to a reduction of the amplitude and regularity of the stick-slip variations as well as a reduction in the average lateral force, i.e. the friction force. When the velocity is sufficiently high, no stick-slip variations can be seen anymore, although the lateral force loops still exhibit the full signature of the presence of a solid condensate. From our data we cannot decide whether at high speeds the ice is merely strongly defected or locally even amorphized [16]. At sufficiently high velocities we should expect to see an unmodulated shear force, as the slip plane in the ice remains permanently damaged.

There is a variety of known ice structures, of which the most common is the hexagonal structure with lattice constants of 0.27 nm and 0.45 nm. These distances can be slightly modified by the geometry of the surface lattice on which the ice monolayers form [17]. On the other hand, the period of 0.38 ± 0.01 nm that we observed may also be associated with the metastable crystalline phase of ice called ice XII, where oxygen atoms are situated at 0.42 nm and 0.402 nm in a unit cell constituted by lattice vectors with $a = 0.83$ nm and $c = 0.402$ nm [18].

One important result of various simulations is that a film of confined water does not layer throughout its complete thickness if it is thicker than 5 monolayers. A recent molecular dynamics study shows that water solidifies at atmospheric pressure and above its freezing temperature when confined in hydrophobic pores with less than one nanometer width [9]. In the light of these simulation results our observation of the ice periodicity only at intermediate humidities probably means that the thickness of the condensate is still small enough at these humidities to provoke complete layering and crystallization, whereas it is too large to set up a single-crystalline connection between tip and substrate at higher humidities, e.g. RH = 50%. The reduced tendency to order at thicker condensates, i.e. at higher RH, is probably also the reason why there is a trend over the 5%-35% intermediate RH range for the maximum velocity at which we see the ice lattice period to decrease with increasing RH.

On average, the well-defined stick-slip behavior with the 0.38 nm ice period is lost at a velocity in the order of 2 nm/s. This corresponds to a time per lattice period (of the ice) in the order of 0.2 s, which is in the same regime as the relaxation time found in the previous chapter for the dynamic component of the lateral force. Again, we obtain evidence for a very long response time, much longer than that of liquid water. The relaxation time found here is directly connected with the observed crystalline quality, which strongly suggests that it is the characteristic time for the annihilation of crystal defects from the ice condensate at room temperature.

As already mentioned above, the re-entry of the graphite lattice period in the lateral force loops at higher velocities was observed only at relatively low humidities, which we associate with very thin ice structures. The graphite signature implies that either the apex of the tip was actually puncturing the ice to touch the graphite or the tip was shearing the thin ice condensate over the graphite surface. At higher relative humidities, for instance 30%, and at high enough velocities where the ice lattice can no longer be distinguished, we instead obtain a more or less featureless friction force plateau, which is preceded by a static force maximum, as shown in Fig. 7.5.

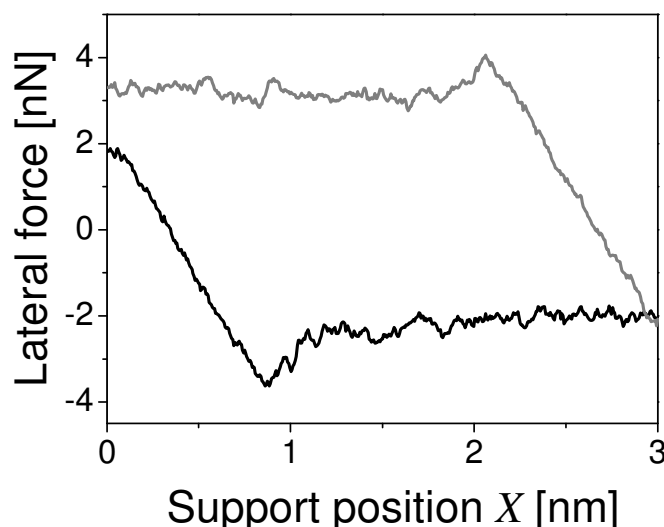


Fig. 7.5. A typical force loop at $RH = 33\%$ and a velocity of 30 nm/s . The lateral force shows no stick-slip instabilities either with the period of the ice lattice or with that of the graphite lattice. Instead the tip slides rather ‘smoothly’. At the start of each scan line (forward and backward) the system has to overcome a higher, static force, which is seen to decay to a lower dynamic force plateau within a distance of $\sim 0.5 \text{ nm}$.

The smooth sliding behavior shows that the tip is not directly in contact with the graphite, which indicates that under these conditions a strongly disordered condensate is present between tip and surface. A natural explanation for the static peak in these measurements is that at the turning points, where the support moves but the tip is (nearly) stationary for some time (order of magnitude 0.1 s) there is again enough time for the condensate to restore its crystalline structure to some extent. As a result, the yield stress of the condensate increases. Once the condensate is stressed beyond its new yield point, the ice quickly damages, within one ice lattice spacing, and sliding proceeds at a lower lateral force because the damaged ice has a lower yield stress.

Not much work has been done before on static friction on the atomic scale. To our knowledge, our results (e.g. Fig. 7.5) form the first observation of an atomic-scale static friction peak obtained with an AFM or FFM. Computer simulations show that static friction may arise due to the presence of adsorbates between the two sliding crystal surfaces [19], which can introduce (contact size

independent) friction coefficients [20]. In the present case, we associate the static peak with a slow crystal damage removal mechanism.

7.3 Friction versus normal loads at high humidity

Since water crystallizes under confinement and the crystalline order seems to reduce with increasing thickness of the condensate, we may expect that also the friction force varies with the thickness of the condensate. Although we have no direct measurement of the thickness of the condensate, we have been able to vary the thickness by changing the normal load on the tip. Figure 7.6 shows the dependence of friction on normal load at elevated RH values. This dependence exhibits several clear plateaus of friction at different normal loads. We interpret each sudden step in the friction force as the result of the removal of a single monolayer of the ice condensate.

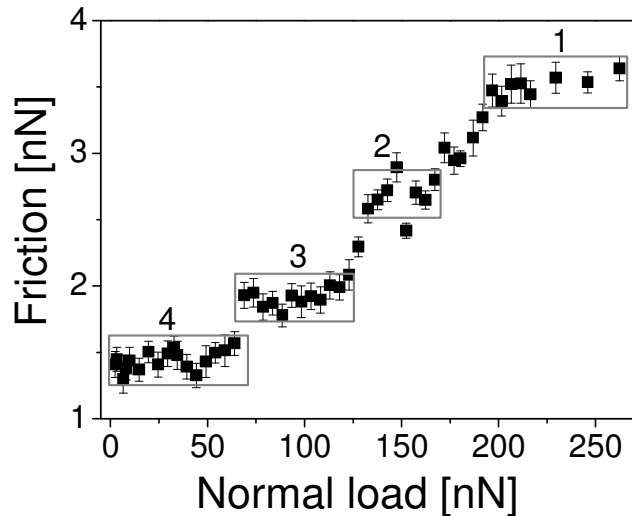


Fig. 7.6. Friction versus normal load at 25% relative humidity. The step-like features are interpreted as the result of the removal of individual monolayers from the ice-like condensate. Each data point is the average of one image (512 force loops).

The different friction levels indicate that either the yield stress of the ice structure or the cross-sectional area of the condensate varies with the number of monolayers present in the condensate. The four levels that we see in Fig. 7.6 show that there are at least four monolayers present in the condensate at low loads (at the highest load, we do not observe stick-slip behavior with the lattice period of

graphite, so there must be at least one monolayer left at that normal load). A stepwise friction responses to variations in the normal load has been observed before for ordered layers of organic molecules, but that has been assigned to the molecular restructuring under higher applied normal loads [21].

7.4 Summary of experimentally observed friction behavior

As a function of the two important parameters that we have varied in Chapter 6 and in the present chapter, namely the relative humidity and the scan velocity, we have encountered a surprisingly wide variety of shear response types. We may think of the two parameters playing completely separated roles. The humidity determines the amount (e.g. thickness) of water condensed into a capillary bridge between the tip and the surface. If the condensate relaxes in structure or shape in response to sliding-induced damage or shape changes, the scan velocity determines how much relaxation can take place during the motion of the tip. Figure 7.7 provides a summary of characteristic lateral force loops, arranged in the form of a humidity-velocity diagram. We have checked that the results were fully reversible with respect to variations in humidity and velocity, without any hysteresis or memory effects, and that the results were reproducible throughout the course of the experiment, over a period of two months.

The lowest humidity of $RH = 1\%$, corresponds to our ‘dry’ conditions, for which we observe stick-slip behavior with the lattice period of graphite at high and medium velocities and nearly vanishing friction at low velocities, reflecting the role of thermal excitations (Chapter 4). The low-velocity force loops at $RH = 5\%$ and 30% show regular stick-slip patterns with the long period that we associate with the lattice structure of crystalline ice. At the intermediate velocity of 5 nm/s the ice lattice can still be recognized, but the amplitude is reduced and the pattern is less regular, which we ascribe to shear-induced damage that cannot be annealed out at this velocity. At $RH = 5\%$ and a high velocity of 50 nm/s we see the re-appearance of the graphite lattice structure, showing that either the tip apex or the thin ice condensate is shearing over the graphite at high velocities. At higher humidities, e.g. $RH = 30\%$, the condensate must be thicker and this high-velocity effect is not seen. We instead observe more or less smooth sliding after an initial static friction peak. Finally, at $RH = 50\%$, tilted force loops are observed, which we have explained with a combination of elastic response and slow relaxation dynamics

(Chapter 6). Our interpretation is summarized in the accompanying diagram of Fig. 7.8.

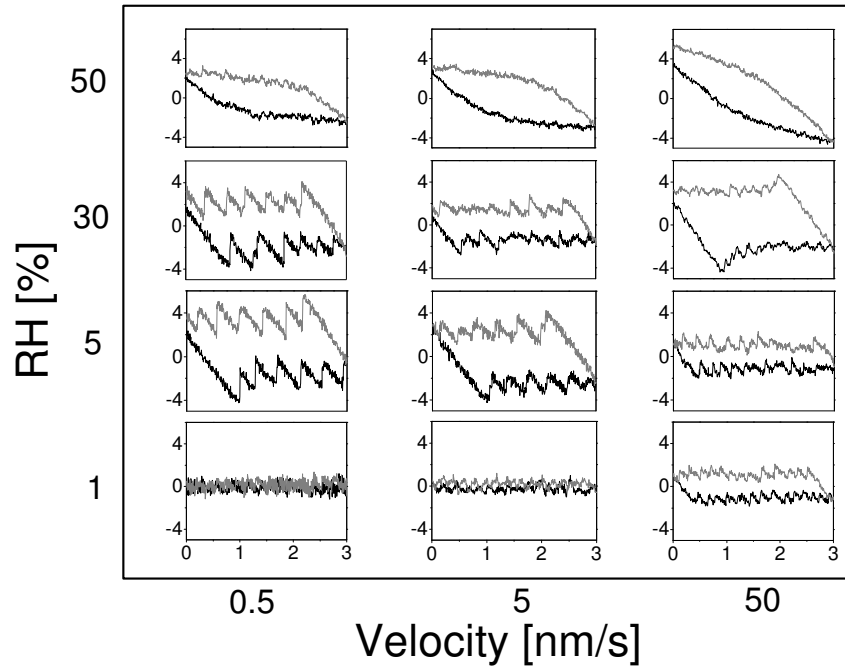


Fig. 7.7. Humidity-velocity diagram, showing the characteristic evolution of lateral force loops with these two crucial parameters. In each loop, the x-axis is the support position in nm and the y-axis is the lateral force in nN.

7.5 Conclusions

In this chapter we have provided very strong evidence for confinement-induced ice formation of a water capillary condensate and we have explored the wide variety of consequences of this phenomenon in the context of atomic friction. At ultra-low scan velocities, slower than the characteristic timescale of the relaxation dynamics of the condensate, the system exhibits stick-slip behavior with relatively high dissipation with a long period that we associate with the lattice of ice. Step-wise variations in the friction force as a function of normal load provide additional evidence for layering of the confined condensate. At high velocities the lattice character of the ice is washed out in the lateral force loops but we still observe the signature of a solid condensate. We report the first observation of a static friction peak that precedes a constant plateau of kinetic friction.

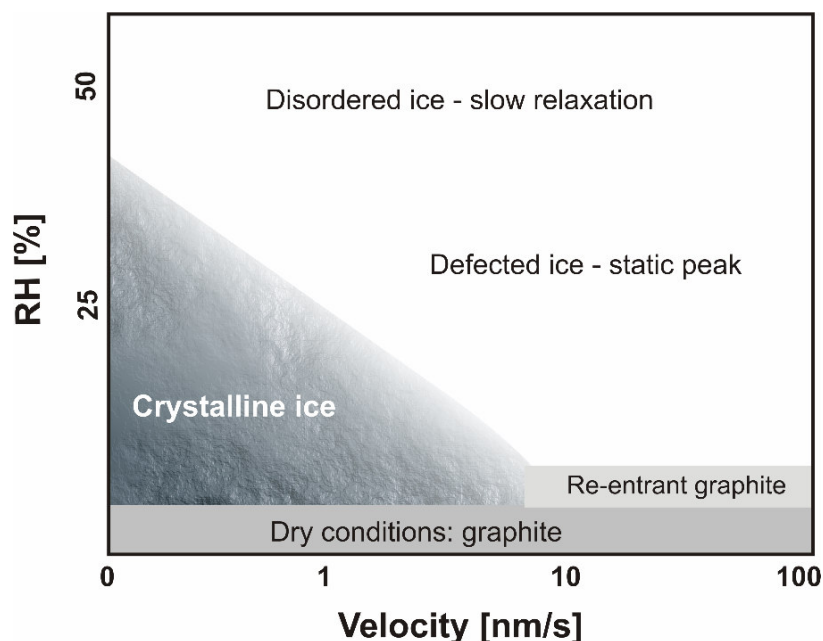


Fig. 7.8. Humidity-velocity diagram, summarizing the interpretation discussed in this chapter and in Chapter 6.

The two key parameters, determining the type of friction behavior observed, are the relative humidity, which dictates the size (e.g. thickness) of the capillary condensate, and the scan velocity, which determines to what extent the condensate can relax in structure and shape, in response to the structural defects and shape changes introduced by the scanning motion. We have come to a basic understanding of the qualitative features of this complex behavior. More detailed modeling and computer simulation will be required to put our ideas to a quantitative test.

7.6 References

1. U. Raviv, P. Laurat, J. Klein, *Nature* **413**, 51 (2001).
2. P.B. Miranda, L. Xu, Y.R. Shen, M. Salmeron, *Phys. Rev. Lett.* **81**, 5876 (1998).
3. M.F. Reedijk, J. Arsic, F.F.A. Hollander, S.A. de Vries, E. Vlieg, *Phys. Rev. Lett.* **90**, 66103 (2003).
4. R. Zangi, A.E. Mark, *J. Chem. Phys.* **119**, 1694 (2003).
5. D.B. Asay, S.H. Kim, *J. Phys. Chem. B* **109**, 16760 (2005).
6. I.M.P. Aarts *et al.* *Phys. Rev. Lett.* **95**, 166104 (2005).
7. Y.S. Chu, T.E. Lister, W.G. Cullen, H. You, Z. Nagy, *Phys. Rev. Lett.* **86** 3364 (2001).
8. V. Ostroverkhov, G. A. Waychunas, Y. R. Shen, *Phys. Rev. Lett.* **94**, 46102 (2005).
9. K.Konga, H. Tanaka, X.C. Zeng, *Nature* **408**, 564 (2000).
10. K. Koga, H. Tanaka, *J. Chem. Phys.* **122**, 104711 (2005).
11. M.C. Gordillo, G. Nagy, J. Martí, *J. Chem. Phys.* **123**, 54707 (2005).
12. K. Koga, G.T. Gao, H. Tanaka, X.C. Zeng, *Nature* **412**, 802 (2001).
13. M. Tadokoro *et al.* *Chem. Commun.* **12**, 1274 (2006).
14. Y. Liu, Q. Wang, *Phys. Rev. B* **72**, 85420 (2005).
15. R. Zangi, A. E. Mark, *Phys. Rev. Lett.* **91**, 25502 (2003).
16. M. Das, G. Ananthakrishna, S. Ramaswamy, *Phys. Rev. E* **68**, 61402 (2003).
17. M.F. Reedijk *et al.* *Phys. Rev. Lett.* **90**, 066103 (2003).
18. C. Lobban, J.L.Finney, W.F. Khus, *Nature* **391**, 268 (1998).
19. G. He, M.H. Müser, M.O. Robbins, *Science* **284**, 1650 (1999).
20. M.H. Müser, L. Wenning, M.O. Robbins, *Phys. Rev. Lett.* **86**,1295 (2001).
21. E. Barrena, S. Kopta, D.F. Ogletree, D.H. Charych, M.Salmeron, *Phys. Rev. Lett.* **82**, 2880 (1999).

Chapter 8

Capillary condensation in atomic friction: large scan ranges

This chapter presents FFM experiments with a tungsten tip sliding over a graphite surface at elevated humidities. By contrast with the measurements of Chapters 6 and 7 we now explore the effect of capillary condensation for scan ranges that are significantly larger than the estimated diameter of the condensate. We find that in this case the tip writes a line of ice on the hydrophobic surface, which stays there for a few seconds.

8.1 Introduction

The experiments presented in the previous two chapters on capillary condensation and its effects on friction have been limited to a small scan range of 3 nm. This means that the support and the tip have been moving back and forth over distances that were in the same order of magnitude as the estimated diameter of the capillary condensate. In the present chapter we investigate scan ranges that are significantly larger than the size of the condensate. One of the prime questions is how well the condensate can follow the moving tip and whether or not we can shear off the condensate at sufficiently high speeds and large scan sizes so that the tip moves over the bare graphite surface again.

8.2 Force loops at higher scan ranges

The experiments presented in this chapter have been performed under the same experimental conditions as those in Chapter 7, with the same tip on the same substrate under a normal load of 3.7 nN. The only differences are in the scan range and the scan velocity. In these experiments, the sweep time was kept constant unless changed intentionally. That means the velocity of scanning varied together with the scan range.

Figure 8.1 shows four characteristic lateral force loops, measured under humid conditions over scan ranges of 8 to 100 nm. We see that the shapes of the force loops are rather different from those reported in the previous chapter for small scans of 3 nm. The striking feature of all four loops is that lateral force in each scan line first levels off (at a value of ~ 2 nN in Fig. 8.1) to increase again just before the *end* of each scan line (both on the forward and on the reverse path). To our knowledge, force loops with such unusual shapes have not been reported before. Force loops measured with the same tip and sample, under the same normal load, but under ‘dry’ conditions (RH = 1%) did not exhibit this peculiar feature. Instead, they followed the *traditional* shape of an elastic force buildup, followed by more or less regular stick-slip motion over the graphite lattice with a constant average lateral force.

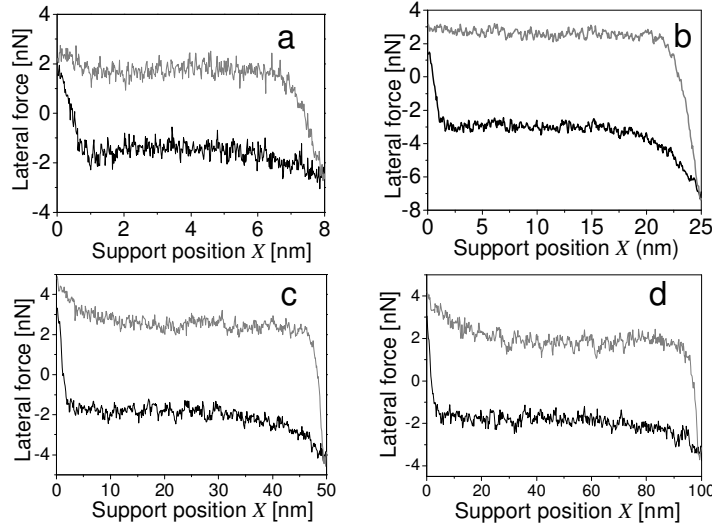


Fig. 8.1. Characteristic lateral force loops measured under humid conditions over different scan ranges: (a) $L = 8$ nm, $RH = 35\%$, b) $L = 25$ nm, $RH = 50\%$, c) $L = 50$ nm, $RH = 40\%$, and d) $L = 100$ nm, $RH = 40\%$.

At high humidities and large scan ranges we have observed both symmetric friction loops, with equally strong friction peaks on both sides and asymmetric loops, with peaks that were not equally large or with only a single peak. Also the force loops in Fig. 8.1 are not completely symmetric. The observations that the asymmetry was independent of scan location and scan size and that it changed primarily between subsequent tip-surface approaches suggest that it is related to the detailed shape of the tip.

In Figure 8.2 we have plotted a collection of force loops obtained within one set of measurements with different scan ranges at the same humidity of $RH = 23\%$. It is clear that the size (width and height) of the pronounced lateral force peak at the end of the forward part of the loop scales more or less linearly with the scan range. This is supported by Fig. 8.3, which shows the height of the force peak versus scan size. The peak width shows a similar variation. We checked that these shapes were completely reproducible and that their variations with scan size were completely reversible. However, as will be explained below, each loop in Fig. 8.2 had to be measured sufficiently long after setting a new scan range to avoid transient effects.

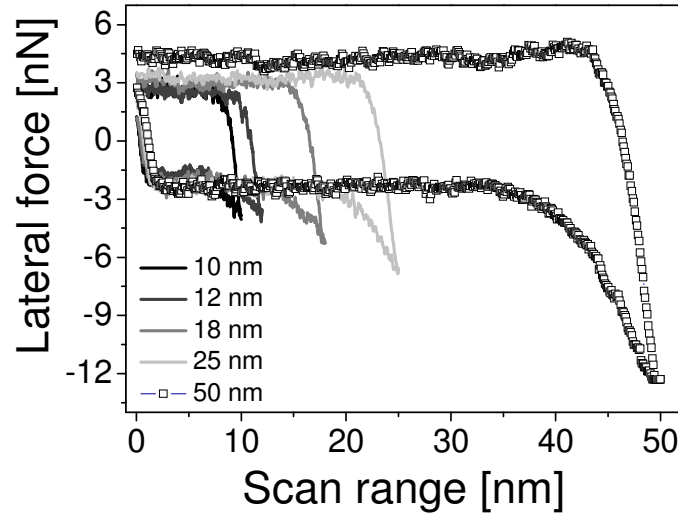


Fig.8.2. Variation of the lateral force peak with the scan range ($RH = 23\%$). Width and height of the (negative) peak in the forward (i.e. lower) part of the force loop are both proportional to the scan range (see Fig. 8.3).

The right panel of Fig. 8.3 shows the dependence of the magnitude of the force peak on velocity at two relative humidities. At $RH = 23\%$ the force peak is constant over a wide range of velocities, whereas it increases with velocity at 35% RH.

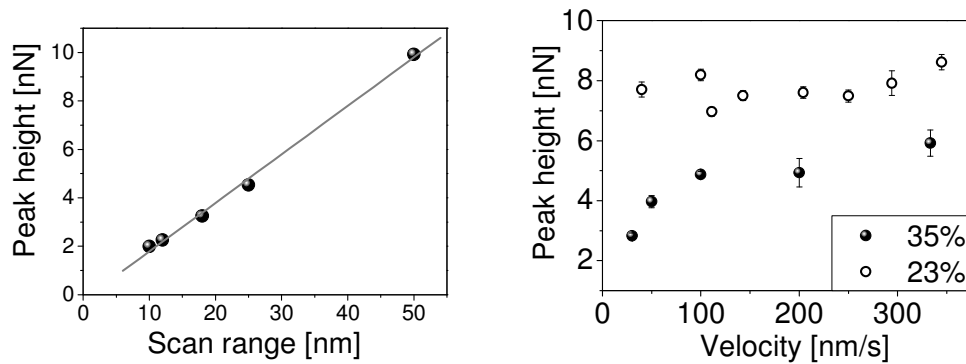


Fig. 8.3. **Left:** Linear relation between the magnitude of the force peak and the scan range. Error margins on the points are smaller than the symbol size. **Right:** Velocity dependence of the magnitude of the force peak at $RH = 23\%$ and 35%.

8.3 Writing ice

Our explanation for the remarkable force loops in Fig. 8.1 and the behavior in Figs. 8.2 and 8.3 forms a natural extension of the mechanism introduced in Chapter 7 to explain the peculiar, tilted force loops for short scan ranges. In this scenario the shear deformations introduced by the scanning motion tend to increase the size of the capillary condensate with respect to its equilibrium size. The cause for this is would reside in a significant discrepancy between the timescale for the addition of water molecules at the front of the moving tip, which we expect to be short (microseconds) and the timescale for the removal of the excess of adsorbed water molecules behind the moving tip, which we speculate to be a slow process (seconds). In other words, the scenario of Chapter 7 is that of writing a short line of water with a limited lifetime of a few seconds. We propose that in the measurements of Figs. 8.1-3 precisely the same mechanism is at work. However, since the scan size is now significantly larger than the diameter of the capillary condensate, the presence of a line of water manifests itself rather differently. The presence of the constant-friction plateau, still without a trace of stick-slip motion, indeed suggests that also for the long scan ranges the tip remains in contact with the condensate over its entire trajectory. We interpret the appearance of a distinct peak near the end of the scan as a sign that the tip reaches the end of the condensate just before the end of each scan line. This means that under these circumstances the condensate is elongated to a length that spans a large fraction of the scan range (Fig. 8.4). In other words, the tip “writes” a stripe of water on the hydrophobic substrate [1]. This situation is strongly reminiscent of the process of Dip-Pen Nanolithography (DPN) [2], with the important difference that in our case the substrate is not hydrophilic and the written line has a finite lifetime.

Up to the maximum scan range of 250 nm in our experiment, we have not observed any indication of the tip detaching from the condensate. Also the maximum abrupt change in scan size of 100 nm (see below) was not accompanied by any sign of detachment. At the end of the large scan range, the situation is similar to that at the end of the smaller scan ranges, with an additional lateral force building up as the tip is deforming the end of the condensate (Fig. 8.4).

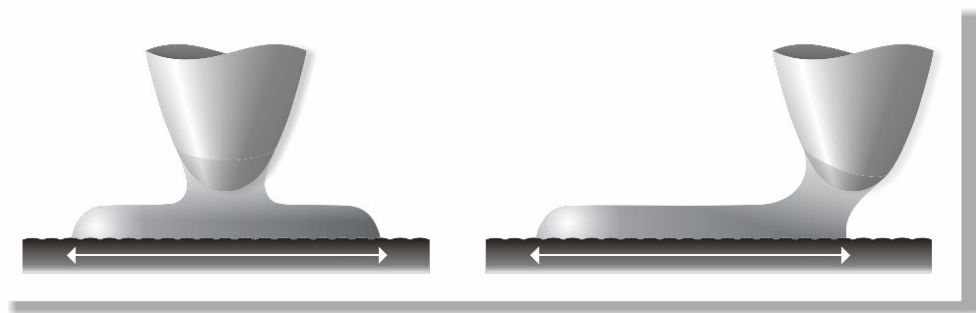


Fig. 8.4. Scenario of the tip drawing a condensate line on the surface. The tip exhibits smooth sliding with a constant lateral force when it is moving over the already written condensate line (left cartoon) and it exhibits a strong increase in the in the lateral force just before it reaches the end of the scan line, where it runs against the end of the condensate (right cartoon). The arrows indicate the scan width.

The scan range of approximately 5 nm, at which the shape of the scans crosses over from a tilted loop to the plateau-and-peak structure, can be used as a crude estimate of the diameter of the equilibrium shape of the capillary neck.

As we argue below, we associate the presence and behavior of the condensed strip on the surface with ice rather than water.

8.4 Dynamic response of the condensate line

Thermodynamically, the presence of a stripe of water on a hydrophobic surface at a humidity well below 100% should not be stable. Instead, once the tip has moved out of the way, the condensate should evaporate completely, possibly passing through an intermediate state in which it would be balled up to a truncated sphere with a contact angle of 86° to the graphite substrate.

To investigate the evolution of the capillary condensate to changes in the tip motion, we performed experiments in which we increased the scan range stepwise during uninterrupted scanning. At a constant RH of 20%, the scan range was varied from 1 nm, to 5 nm, 10 nm, 15 nm, 25 nm, 50 nm, 100 nm and finally to 200 nm. The change in the average friction force of each loop as a function of the scan line number is shown in Fig. 8.5. Every increase in scan size leads to a stepwise increase of the friction force, which quickly decays in the following scan lines.

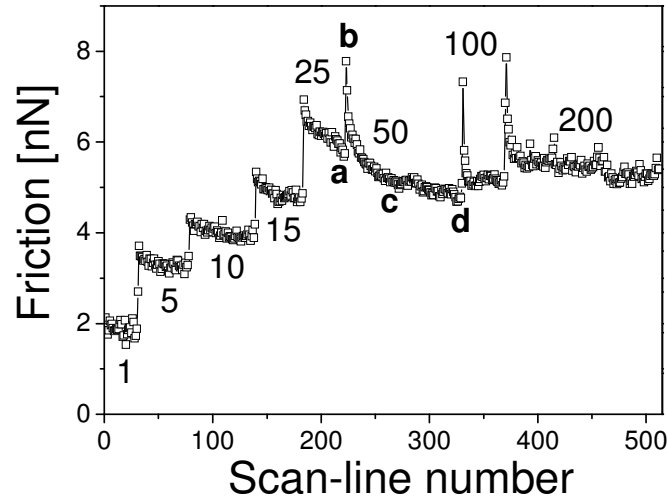


Fig. 8.5. Variation of the average friction force when the scan range is increased suddenly while the tip is scanning. The letters a, b, c and d represent the section of the sequence that we used to study the phenomenon in more quantitative detail.

In Figs. 8.6 and 8.7 we concentrate on the region in Fig. 8.5 denoted by the letters **a-d**, where we changed the scan range from 25 to 50 nm. The four panels in Fig. 8.6 show the individual lateral force loops at the four indicated positions in Fig. 8.5, panel **a** corresponding to the last loop at 25 nm and **b** corresponding to the first one at 50 nm. These loops are all asymmetric, displaying a strong peak near the end of the forward scans and almost not peak at all at the end of the reverse scans. The forward peak is so strong that it exceeds the maximum force that could be measured by our detection system, which is why the forward peaks in all four panels are truncated. The main difference between loops **a** and **b** is that the width of the forward force peak (arrow in panel **b**) has increased dramatically in **b**. In fact, the increase in **b** starts at the same distance from the middle of the scan line as that in **a**. In subsequent scan lines we observe that the peak gradually narrows, the starting position shifting more and more towards the end of the scan line. The shape measured in panel **d** is close to the final shape, which we observe after prolonged scanning at the same scan range. In Fig. 8.7 we have plotted the width of the force peak as a function of the time passed since the stepwise increase in scan range. We

observe an exponential-like decay with a characteristic time in the order of 2 s (see below).

When the scan size is reduced stepwise, e.g. from 50 to 25 nm, the first force loops exhibit the ‘traditional’ shape, i.e. without friction peaks near the ends and the friction peaks reappear only after a delay in the order of 1 s. In spite of the slow response, all changes were found to be completely reversible without a trace of hysteresis.

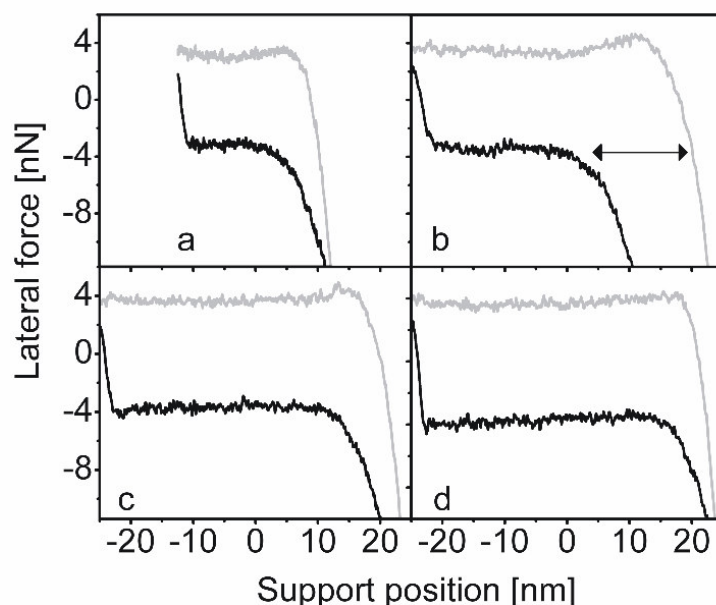


Fig. 8.6. Evolution of the lateral force loop when the scan range was suddenly increased from 25 nm (a) to 50 nm (b). The evolution of the force loops when we continued to scan at 50 nm is shown in c and d. Panels b, c and d were obtained 1, 14 and 102 force loops after panel a, respectively.

These measurements clearly indicate that the length of the strip of condensate on the surface adjusts only very slowly to changes in the scan size. Note, that it is only the support that moves over the entire scan size. The force peak at the end of the scan line indicates that the tip lags behind significantly as it reaches the end of the condensate. In other words, it is held back very strongly by the condensate. The long persistence of the condensate (order of magnitude of seconds) on the surface suggests strongly that not only the water immediately

below the tip, but also the rest of the entire, elongated condensate is solid rather than liquid. If the water would be solid only locally, the liquid remainder of the condensate would have the opportunity to ball up at a speed characteristic for water. This conclusion implies that the condensate does not require confinement between *two* solids, the tip and the substrate, to be solid, but that the mere presence of a single interface with the graphite substrate is sufficient [1].

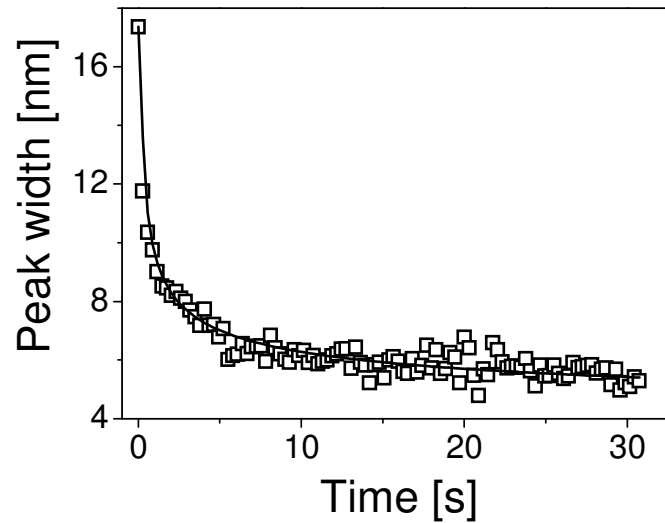


Fig. 8.7. Time dependence of the peak width of the force loops on the time passed after a sudden increase in scan width from 25 to 50 nm (see Figs. 8.6 and 8.7). The continuous line is an empirical fit with a $1/3^{\text{rd}}$ power law.

8.5 Timescales and mechanisms

Above, we referred to the decay of the peak width with time in Fig. 8.7 as ‘exponential-like’. However, the long-time behavior is too slow to be described well by an exponential. The fit in Fig. 8.7 shows that we can obtain an excellent fit with a power law with a time exponent of $1/3$, decaying to a constant peak width of approximately 3.5 nm. This saturation value is in the order of our earlier estimate for the equilibrium diameter of the condensate, which should indeed serve as a natural end point of the evolution of the size and shape of the condensate. The fact that we observe a power law is consistent with a rearrangement dominated by surface-curvature-driven evolution dynamics, e.g. surface diffusion, which would

be in line with our notion that the condensate is solid and cannot exhibit true flow. In the remainder of this section we briefly consider alternative rearrangement mechanisms and the expected timescales.

We can get a rough estimate of the timescale for rearrangement of an ice condensate via evaporation-recondensation dynamics. For this we use a sublimation rate of ice, extrapolated to room temperature, of 2.8×10^6 ML/s [3,4]; the impingement rate of water molecules at a humidity of 100% and room temperature is in the order of 10^6 ML/s. One monolayer of ice corresponds to approximately 10^{15} molecules/cm². In the appendix we show that an ice line on the surface, 50 nm long, 5 nm wide and 5 nm thick would sublime within 430 μ s. Recently reported Molecular dynamics (MD) simulations also predict that a capillary condensate would completely evaporate within a timescale of a few microseconds [5,6]. Our observations of persistence times in the order of seconds stand in strong contradiction with these short timescales. There exists a variety of further experimental observations that deviate completely from the expected microsecond timescales. For example, water nanoclusters of 2-5 nm height formed at elevated RH values have been observed to have ice-like behavior, and they sustained on a graphite surface even after flushing with dry nitrogen for 48 hours [1,7,8]. This intriguingly long persistence of ice-like nanoclusters on surfaces has also been observed in experiments in our laboratory. Further, capillary condensates forming in AFM experiments with gold coated micro-glass spheres have been seen to cause an adhesion force between the tip and the surface that persisted for more than 68 hours while the AFM setup was flushed with dry nitrogen [9]. The mystery of this intriguingly long lifetime has not been resolved yet. Recent studies have shown that the rate at which water evaporates off from a confinement is significantly less than that of the condensation [10], indicating that the energy barrier for the evaporation of the condensed water is much more than the barrier to evaporate off. As result, the capillary bridge grows in time and exhibit longer memory effects. A recent attempt to estimate the nucleation timescales of the capillary meniscus formation shows that the energy barrier to initiate nucleation between a typical AFM tip and a mica surface is 0.47 eV [11], which is, interestingly, the activation barrier for the evaporation of ice at room temperature! [12].

8.6 Conclusions

From the peculiar shapes of lateral force loops obtained in FFM experiments with a tungsten tip on a graphite surface under humid conditions, we infer that the tip “writes” a temporary line of water on the hydrophobic surface. The extremely long timescale, in the order of seconds, observed for the spontaneous rearrangements of the line-shaped condensate in response to sudden changes in scan size indicate that the water is present on the surface in the form of ice.

Further work will be necessary to obtain detailed information on the structure of the solid condensate and to identify the mechanism of its slow rearrangements. It will be important to determine whether other tip-surface combinations and other contact geometries can make the condensate stay liquid. Finally, it remains to be investigated to what extent the ice-like behavior contributes to friction under practical circumstances and what role it might play in novel writing techniques such as Dip-Pen Nanolithography.



8.7 References

1. A. Gil, J. Colchero, M. Luna, J. Gómez-Herrero, A.M. Baró, *Langmuir* **16**, 5086 (2000).
2. R.D. Piner, J. Zhu, F. Xu, S.H. Hong, C.A. Mirkin, *Science* **283**, 661 (1999).
3. J.G. Davy, G.A. Somorjai, *J. Chem. Phys.* **55**, 3624 (1971).
4. M. Elbaum, *Optical search for melting of ice*, PhD Thesis, University of Washington, USA, 1991.
5. K. Leung, A. Luzar, D. Bratko, *Phys. Rev. Lett.* **90**, 65502 (2003).
6. A. Luzar, *J. Phys. Chem. B* **108**, 19859 (2004).
7. M. Luna, J. Colchero, A.M. Baró, *J. Phys. Chem. B* **103**, 9576 (1999).
8. R.K. Workman, S. Manne, *Langmuir* **18**, 661 (2002).
9. J. Grobelny, N. Pradeep, D.I. Kim, Z.C. Yang, *Appl. Phys. Lett.* **88**, 91906 (2006).
10. B.L. Weeks, M.W. Vaughn, *Langmuir* **21**, 8096 (2005).
11. R. Szoszkiewicz, E. Riedo, *Phys. Rev. Lett.* **95**, 135502 (2005).
12. J. G. Davy, G. A. Somorjai, *J. Chem. Phys.* **55**, 3624 (1971).

8.8 Appendix

Here we present a rough estimate of the lifetime of an ice line segment on a surface at a relative humidity of 100%: let us envisage a rectangular block of ice with a length of 50 nm, width of 5 nm and height of 5 nm. Suppose that 1 nm ice at the end of the condensate is relocated to the sides of the condensate, thus reducing the length by 1 nm and increasing the width by 5/50 nm. The initial surface area exposed to the ambient was 800 nm², which reduces to 790.9 nm² due to this rearrangement. Thus, the change in surface area by the rearrangement is -9.1 nm². We estimate the corresponding change in surface free energy to be $\Delta\Gamma$ = change in area \times surface free energy/unit area (γ). Here, γ for ice is 0.46 eV/mol, obtained from M. Elbaum, *Optical search for melting of ice*, PhD Thesis, University of Washington, 1991. Thus,

$$\Delta\Gamma / \text{molecule} = -\frac{9.1 \text{ nm}^2 \times \gamma}{5 \text{ nm} \times 5 \text{ nm} \times \rho} = -4.82 \text{ meV/molecule},$$

where ρ is the number density of ice.

Since evaporation is an activated process, it obeys the Arrhenius law, but due to the energy lowering, the sublimation rate should now be increased with respect to the equilibrium rate, which, in turn, is equal to the rate of attachment of water molecules. As a result the sublimation rate is a factor $\exp(4.82 \text{ meV}/kT) \sim 1.2$ times the equilibrium impingement and sublimation rates.

From Ref [V. Sadtchenk *et al*, *J. Chem. Phys.* **121**, 11980 (2004)] we obtain an equilibrium sublimation rate of ice at 0°C of 50mg/cm² s, which is 1.72 $\times 10^6$ monolayers/ s (ML/ s). If our condensate line reduces its length at 20% of this rate (20% more sublimation than impingement), its lifetime would be roughly (50 nm \times 3 ML/nm) / (0.2 \times 1.72 $\times 10^6$ ML/ s) \sim 430 μ s.

Chapter 9

Conclusions

9.1 Summary of the work presented in this thesis

This Ph.D. thesis presents two important aspects of the atomic scale origin of friction which cannot be ignored under realistic conditions: the role of temperature and the influence of the humidity of the environment. We have experimentally investigated a variety of phenomena related to these aspects, using a special-purpose, high-resolution friction force microscope (FFM). Thermal activation of the sliding asperities in tip-based experiments is discussed at length in the first part of this thesis. We go beyond the basic picture of the thermal energy $k_B T$ assisting the tip to overcome the potential barriers set up by the substrate atoms. This activated process only leads to a weak, logarithmic velocity dependence of friction. In our description the tip can also accomplish occasional backward jumps to a neighboring potential well, even if the energy barrier height for such jumps is much higher than the thermal energy. We mold this description in the form of a set of rate equations for the exchange of probability between the accessible energy wells for finding the tip in these wells. The numerical analysis of this set of rate equations shows that the reduction of friction due to thermal activation of the tip is much more dramatic than the logarithmic lowering in two cases: at low energy barrier heights and at low velocities. These circumstances lead to a high proportion of multiple, backward and forward jumps of the tip, which induce a spectacular reduction of the friction force. We call this effect *thermolubricity*.

Analyzing the intrinsic noise in our experimentally obtained lateral force images, we conclude that most of this noise is purely thermal in origin. We demonstrate in Chapter 3 that a reduction of the surface corrugation (energy barrier) significantly lowers the friction force compared with the friction expected in the absence of thermal effects (Tomlinson model).

As a next step, in Chapter 4 we confront the thermolubricity model with additional experiments that focus on the velocity dependence of friction. Force loops measured at different velocities exhibit explicit differences, in which we can directly identify the predicted velocity regimes of stick-slip motion, stochastic motion (nearly two jumps per lattice spacing) and thermal drift motion (many jumps per lattice spacing). At ultra-low velocities, the friction force reduces more dramatically than logarithmically.

One of the key parameters in our thermolubricity description is a pre-exponential factor, which can be viewed as an attempt frequency for the tip to jump

to the neighboring energy wells. Within a one-dimensional picture, our model fails to fit all observations with different velocities and different energy barriers with a single value for this frequency factor. In a realistic potential energy landscape, the tip has the freedom to follow a variety of two-dimensional trajectories. In particular at lower velocities, the tip occasionally follows an energetically unfavorable path to the next stable potential minimum. The original one-dimensional model is ‘blind’ to this aspect of the tip trajectories. We have extended our calculations to a full, two-dimensional description and find that this makes the velocity dependence of the friction force at low velocities significantly more dramatic than it already was in our 1D model. The 2D model reasonably fits the experimental data with a single attempt frequency. Interestingly, its value is one order of magnitude higher than the mechanical eigenfrequency of the cantilever used in our experiment. Further work is currently in progress attempting to associate the precise value of the attempt frequency with the mechanical behavior of an advanced thermolubricity model with two springs and two masses, mimicking the combination of a slow resonance frequency of the macroscopic cantilever and a rapid motion of the tip apex with atomic-scale vibrational frequencies.

Chapter 5 describes a successful attempt to provoke effects similar to the thermal effects of Chapters 2-4 by mechanical excitation of the friction device. We find that applying external excitations provides an extremely powerful alternative with respect to increasing temperature, which would be unfeasible under most realistic conditions. We actuate the FFM cantilever at its resonance frequency with an external loudspeaker and show that friction reduces to the detection limit of the FFM at sufficiently high actuation amplitude. We provide a straightforward model for this friction lowering effect. Chapter 5 closes the discussion on dry friction in this thesis.

Chapters 6 to 8 discuss the phenomenon of water vapor from the ambience condensing between the tip and the surface, thus forming a water bridge connecting the two surfaces. The energy dissipation in this situation is primarily governed by the energy lost in shearing the capillary condensate. We discover that a very pronounced mechanism causing high dissipation at modest shear rates is the confinement-induced solidification of the capillary condensate. We observe a nearly velocity-independent static friction force in lateral force loops at high humidities, which we interpret as a signature of a finite yield stress of the condensate, proving that the condensate mechanically behaves as a solid. The

estimated mechanical properties, i.e. the Young's modulus and the shear yield stress are in the order of magnitude of those for bulk ice.

In Chapter 7, we discuss the velocity dependence of friction at various humidities. At sufficiently low scan velocities of the order of 1 nm/s, we observe pronounced and well-defined stick-slip motion and strongly increasing friction with reducing velocity. We associate the average stick-slip distance of 0.383 ± 0.01 nm with the lattice of a crystalline form of ice. As a function of velocity and humidity we explore a surprisingly wide variety of manifestations of the presence and rearrangements of the solid-like, capillary condensate, such as e.g. the appearance of a static friction peak. Together, these different types of behavior are summarized in a two-dimensional diagram of rather different lateral force loops versus humidity and velocity. Our capillary ice scenario provides a qualitative explanation for most aspects of this complex diagram.

In Chapter 8 we go beyond confinement by exploring scan ranges that are significantly larger than the size of the condensate. We observe strong transient memory effects that indicate that the tungsten tip writes stripes of ice on the hydrophobic graphite surface, which stay on the surface for an unexpectedly long time in the order of a few seconds.

9.2 Future prospects: scientific challenges

Regarding the dry friction and related phenomena discussed in the first half of the thesis, thermolubricity calculations have to be completed with the full, two-dimensional motion of the two-spring model. These numerical calculations are expected to provide us with a more or less complete picture of the thermally activated processes influencing atomic-scale friction. Results of this complex model should reveal the role of the hidden timescales involved in the dissipation mechanisms – information presently concealed in a single fit parameter, namely the effective attempt frequency. Disentangling the behavior on the two timescales of the two-spring-two-mass system, we should obtain insight into the crucial matter of where the energy is really dissipated and how large the truly microscopic dissipation rate really is.

It should be clear that our thermolubricity model is far from providing a complete description of atomic-scale friction. It shares most of the limitation of other models that are variations on and modest extensions of the classical

Tomlinson model. For example, we assume that the velocity is always low enough that the excess energy involved in a slip-event has been dissipated completely before the next slip can take place. At higher velocities, such a simplifying assumption must break down, and we may expect to even see a signature of ‘wash-board’ resonances in the friction force. At still higher velocities, beyond the maximum (thermal) velocities of the cantilever, tip and surface, we should expect to find a friction force that simply scales linearly with the velocity, showing the truly intrinsic dissipation rate of the tip-surface contact. What the truly intrinsic dissipation mechanisms are, e.g. phonon generation or electronic friction, remains to be explored.

The technique of lowering friction via mechanical resonances carries a promise for potential application. The enforced motion can easily be generated by a component integrated with a small instrument, such as a MEMS or NEMS device. This is a field that surely merits further efforts.

Capillary condensation forms a relatively new aspect in atomic friction studies. We have already discovered a wealth of new phenomena. Although we provide a qualitative explanation for these phenomena, much more systematic work will be required to bring the interpretation and understanding to a quantitative level. Obviously, the presence of water and especially ice between moving asperities has practical implications in static friction and in sliding friction, not only in atomic-scale experiment but also in a wide range of practical settings. The most intriguing observation at this point is that of the enormous timescale of seconds for the rearrangements of the condensate.

There are several improvements to the special-purpose FFM setup in Leiden that will open the door to interesting future experiments. Of course, the key parameter in the thermal effects discussed in this thesis is *temperature*. Yet, we have kept temperature fixed at room temperature in all experiments in this thesis. Relatively modest modifications will be necessary to make it possible to stabilize other temperature, higher and lower, sufficiently to allow temperature-dependent experiments over an appreciable range in temperature and at acceptably low thermal drift speeds of the tip-surface contact and of the fiber-optic force detection system. Another limitation strongly felt in the present work lies in the bandwidth of the force detection and data acquisition system. Higher-speed electronics will allow time-resolved measurements of fast phenomena, such as the statistics of the nucleation of a capillary bridge between a tip and a surface, the rapid multiple

jumps of a tip in the thermolubric regime, or the precise motion of the cantilever and tip during a slip event.

As always, this research has generated more questions than answers. Nevertheless, our insight has progressed and we hope that it will initiate further research on the fundamentals of atomic scale friction.



Samenvatting

Samenvatting van het onderzoek beschreven in dit proefschrift

Dit proefschrift beschrijft twee belangrijke aspecten van de oorsprong van wrijving op atomaire schaal waarmee ook in meer realistische situaties rekening gehouden moet worden: de rol van temperatuur en de invloed luchtvochtigheid. Wij hebben een scala aan verschijnselen die gerelateerd zijn aan deze aspecten experimenteel onderzocht met behulp van een speciale, zelf ontwikkelde, hoge-resolutie wrijvingsmicroscop (*Engels*: Friction Force Microscope).

In het eerste deel van dit proefschrift bespreken we de thermische activering van schuivende contacten in experimenten met scherpe tips. We gaan hierbij verder dan het basisidee dat alleen beschrijft hoe de tip, geholpen door de thermische energie $k_B T$, de potentiaalbarrières overwint die opgeworpen worden door de substraatatomen, overwint. Dit geactiveerde proces alleen leidt tot een logaritmische snelheidsafhankelijkheid van de wrijving. In onze beschrijving kan de tip ook terugspringen naar een aangrenzende potentiaalput, zelfs als de energiebarrière voor zo'n sprong veel hoger is dan de thermische energie. Wij gieten deze beschrijving in de vorm van een serie vergelijkingen voor de uitwisseling van waarschijnlijkheid (om de tip in een bepaalde put te vinden) tussen de op elk moment toegankelijke potentiaalputten. De numerieke analyse van deze serie vergelijkingen laat zien dat de afname van wrijving door thermische activering van de tip in twee gevallen veel dramatischer is dan de logaritmische verlaging: bij lage energiebarrières en bij lage snelheden. Onder deze omstandigheden springt de tip meerdere keren per roosterconstante vooruit en achteruit. Dit veroorzaakt een spectaculaire verlaging van de wrijving. Wij noemen dit effect '*thermolubriciteit*'.

Op basis van de analyse van de intrinsieke ruis in onze experimenteel verkregen laterale-krachtplaatjes concluderen wij dat het overgrote deel van deze ruis thermisch van aard is. In hoofdstuk 3 laten we zien dat een verlaging van de amplitude van de oppervlaktepotentiaal de wrijvingskracht significant verlaagt vergeleken met de verwachte wrijving in afwezigheid van thermische effecten (Tomlinson model).

In hoofdstuk 4 confronteren we het model voor thermolubriciteit met extra experimenten die gericht zijn op de snelheidsafhankelijkheid van wrijving. Krachtcurves gemeten bij verschillende snelheden vertonen opvallend verschillende kenmerken, waarin we direct de voorspelde snelheidsregimes voor ‘stick-slip’ beweging, stochastische beweging (bijna twee sprongen per roosterafstand) en beweging door thermische drift (veel sprongen per roosterafstand) herkennen. Bij ultralage snelheden is de verlaging van de wrijvingskracht dramatischer dan logaritmisch.

Eén van de centrale parameters in onze beschrijving van thermolubriciteit is een voorfactor die gezien kan worden als een probeerfrequentie voor de tip om naar aangrenzende potentiaalminima te springen. De experimentele observaties bij verschillende snelheden en energiebarrières worden niet goed beschreven door een ééndimensionale versie van ons model als we maar één waarde van de probeerfrequentie toelaten. In een meer realistisch potentiaallandschap heeft de tip de vrijheid om verschillende *tweedimensionale* paden te volgen. Soms, in het bijzonder bij lage snelheden, volgt de tip een energetisch gezien ongunstig pad om in het volgende stabiele potentiaalminimum te komen. Het ééndimensionale model is ‘blind’ voor deze mogelijke paden. Wij hebben onze berekeningen uitgebreid naar een volledige, *tweedimensionale* beschrijving en we vinden dat de snelheidsafhankelijkheid van de wrijvingskracht bij lage snelheden nog dramatischer is dan zij al was in ons eendimensionale model. Het *tweedimensionale* model komt redelijk goed overeen met de experimentele data met slechts één probeerfrequentie. De waarde van deze frequentie is, interessant genoeg, een orde van grootte hoger dan de mechanische eigenfrequentie van de miniatuur bladveer die in het experiment gebruikt is. Momenteel is onderzoek gaande waarin wordt getracht de precieze waarde van de probeerfrequentie te associëren met het mechanische gedrag van een geavanceerd thermolubriciteitsmodel met twee veren en twee massa’s. Dit model bootst de combinatie na van een lage resonantiefrequentie van de macroscopische bladveer en de snelle beweging van het uiteinde van de tip met atomaire vibratiefrequenties.

Hoofdstuk 5 beschrijft een succesvolle poging om soortgelijke effecten als het thermische effect uit de hoofdstukken 2-4 met mechanische excitatie van het wrijvingsapparaat op te wekken. Wij denken dat het aanbrengen van een mechanische excitatie een extreem krachtig alternatief is voor een temperatuurverhoging, die onder de meeste realistische omstandigheden onhaalbaar

is. Wij drijven de FFM bladveer aan op zijn resonantiefrequentie met een externe luidspreker en laten zien dat de wrijving bij een voldoende hoge aandrijfamplitude afneemt tot de detectielimiet van de wrijvingsmicroscoop. We geven ook een eenvoudig model voor dit wrijvingsverlagende effect. Hoofdstuk 5 vormt de afsluiting van de discussie over droge wrijving in dit proefschrift.

Hoofdstukken 6 tot en met 8 beschrijven het verschijnsel van de vorming van een waterbrug tussen de tip en het oppervlak door de condensatie van water uit de omgeving. De energiedissipatie wordt in deze situatie vooral bepaald door de energie die verloren gaat bij het vervormen van het condensaat. Wij hebben ontdekt dat door de opsluiting ijsvorming wordt geïnduceerd van het capillaire condensaat en dat dit mechanisme leidt tot hoge dissipatie bij bescheiden schuifsnelheden. We zien een bijna snelheidsonafhankelijke statische wrijvingskracht in laterale krachtmetingen bij hoge luchtvochtigheid. Dit interpreteren we als een kenmerk van de eindige schuifspanning van het condensaat, waarmee bewezen is dat het condensaat zich gedraagt als een vaste stof. De geschatte mechanische eigenschappen, met name de Young modulus en de maximale schuifspanning, zijn van dezelfde orde van grootte als die van ijs.

In hoofdstuk 7 beschrijven we de snelheidsafhankelijkheid van wrijving bij verschillende waarden van de luchtvochtigheid. Bij voldoende lage scansnelheden, in de orde van 1 nm/s, zien we duidelijke en goed gedefinieerde stick-slip beweging en een sterk toenemende wrijving bij afnemende snelheid. Wij associëren de gemiddelde stick-slip afstand van 0.38 ± 0.01 nm met de roosterafstand van een vorm van kristallijn ijs. Als functie van snelheid en luchtvochtigheid verkennen wij een verrassend breed scala van manifestaties van de aanwezigheid van het ijscondensaat, zoals het optreden van een statische wrijvingspiek. Deze verschillende gedragingen van het condensaat worden samengevat in een tweedimensionaal diagram van laterale-krachtmetingen uitgezet tegen luchtvochtigheid en snelheid. Ons capillaire ijsscenario levert een kwalitatieve verklaring voor de meeste aspecten van dit complexe diagram.

In hoofdstuk 8 gaan we voorbij de effecten van opsluiting door het scanbereik significant groter te maken dan de grootte van het condensaat. We zien geheugeneffecten die erop wijzen dat de wolfram tip een lijn van ijs op het oppervlak schrijft. Deze lijn blijft voor de onverwacht lange duur van een paar seconden op het hydrofobe grafietoppervlak liggen.

Toekomstperspectieven: wetenschappelijke uitdagingen

Voor droge wrijving en gerelateerde verschijnselen beschreven in de eerste helft van dit proefschrift moeten thermolubriciteits-berekeningen aangevuld worden met de volledige tweedimensionale beweging van het model met twee veren. Deze numerieke berekeningen zullen ons naar verwachting een complete beschrijving geven van de thermisch geactiveerde processen die de wrijving op atomaire schaal beïnvloeden. De resultaten van dit complexe model zouden de verborgen tijdschalen die een rol spelen in de dissipatiemechanismen moeten onthullen. Deze informatie zit nu nog verborgen in één fit-parameter, namelijk de effectieve probeerfrequentie. Het ontwarren van het gedrag van het systeem van twee veren en twee massa's op de twee tijdschalen zou ons inzicht moeten geven in de cruciale vraag: waar wordt energie gedissipeerd en hoe groot is deze microscopische dissipatiesnelheid echt?

Het moge duidelijk zijn dat ons thermolubriciteitsmodel nog ver is van een volledige beschrijving van atomaire wrijving. Ons model deelt de beperkingen van andere variaties op, en uitbreidingen van, het klassieke Tomlinson model. We nemen bijvoorbeeld aan dat de snelheid altijd zo laag is dat de overvloedige energie van een stick-slip gebeurtenis vóór de volgende stick-slip gebeurtenis al compleet gedissipeerd is. Zo'n aanname is bij hogere snelheden niet meer houdbaar en misschien zullen we in de toekomst bij dergelijke snelheden wel 'wasbord' resonanties waarnemen in de wrijvingskracht. Bij nog hogere snelheden, boven de maximale (thermische) snelheden van de bladveer, de tip en het oppervlak, verwachten we een wrijvingskracht te vinden die lineair schaalt met de snelheid. Op die manier moeten we de intrinsieke dissipatiesnelheid van het tip-oppervlak contact te zien krijgen. Wat de daadwerkelijk belangrijke microscopische dissipatiemechanismen zijn, bijvoorbeeld de creatie van fononen of elektronische wrijving, moet nog onderzocht worden.

De techniek om de wrijving te verlagen via mechanische resonanties draagt een potentiële toepassing in zich. De geforceerde beweging kan gemakkelijk gegenereerd worden door een extra component, geïntegreerd in kleine apparaatjes, zoals een MEMS of een NEMS. Inspanningen in deze richting zijn zeker het proberen waard.

Capillaire condensatie is een relatief nieuw aspect van studies van atomaire wrijving. We hebben al een schat aan nieuwe verschijnselen ontdekt. Hoewel we een kwalitatieve uitleg van deze fenomenen aanvoeren, zal er nog veel meer

systematisch werk nodig zijn voor begrip op kwantitatief niveau. Uiteraard heeft de aanwezigheid van water tussen bewegende contacten praktische gevolgen voor statische en dynamische wrijving, niet alleen in experimenten op atomaire schaal maar ook in veel praktische situaties. De meest intrigerende observatie op dit terrein is de enorm lange tijdschaal van seconden waarop het condensaat zich herschikt.

Er zijn een aantal verbeteringen mogelijk aan de speciale, hoge-resolutie wrijvingsmicroscop in Leiden. Deze zullen de deur openen naar nieuwe, interessante experimenten in de toekomst. De belangrijkste parameter voor de thermische effecten beschreven in dit proefschrift is uiteraard temperatuur. Tot nog toe hebben we alle experimenten uitgevoerd bij kamertemperatuur. Voor het mogelijk maken van experimenten bij andere temperaturen, lager of hoger en over een voldoende groot bereik voor temperatuursafhankelijke metingen en met voldoende lage thermische driftsnelheid van het tip-oppervlak contact en van het fiber-optische krachtmetingsysteem, is een bescheiden uitbreiding van de huidige opstelling nodig. Een andere lastige beperking ligt in de bandbreedte van de krachtmeting en de data-acquisitie. Snellere elektronica zal tijdsopgeloste metingen van snelle verschijnselen mogelijk maken. Denk bijvoorbeeld aan de statistiek van de nucleatie van de capillaire brug, het snelle heen en weer springen van de tip in het thermolubriciteitsregime of de precieze beweging van de bladveer en de tip tijdens een slip-gebeurtenis. Zoals altijd heeft dit onderzoek meer vragen dan antwoorden opgeleverd. Toch hebben we beduidend meer inzicht verkregen en we hopen dan ook dat dit onderzoek een aanzet is tot verder onderzoek naar wrijving op atomaire schaal.

List of publications

This thesis is partly based on the following articles:

1. *Capillary condensation in atomic-scale friction: how water acts like a glue*
K.B. Jinesh, J.W.M. Frenken, *Phys. Rev. Lett.* **96**, 166103 (2006).
2. *Thermally induced reduction of friction at the atomic scale*
S. Yu Krylov, K.B. Jinesh, H. Valk, M. Dienwiebel, J.W.M. Frenken; *Phys. Rev. E* (Rapid communications) **71**, 65101 (2005).
3. *Thermally activated reduction of atomic-scale friction*
K.B. Jinesh, S. Yu Krylov, H. Valk, M. Dienwiebel, J.W.M. Frenken, Conference Proceedings, Micro and Nanotechnology, Vienna, Austria, 2005. Page 409-413.
4. *Direct evidence for ice formation at room temperature*
K.B. Jinesh, J.W.M. Frenken, in preparation for submission to *Nature*.
5. *Velocity dependence of atomic friction: role of dimensionality*
K.B. Jinesh, J.A. Dijksman, S.Yu. Krylov, J.W.M. Frenken, in preparation for submission to *Phys. Rev. Lett.*
6. *Thermolubricity in atomic-scale friction*
K.B. Jinesh, S. Yu Krylov, J.A. Dijksman, H. Valk, M. Dienwiebel, J.W.M. Frenken; in preparation for submission to *Phys. Rev. B*.
7. *Confinement induced solidification of water in atomic friction measurements*
K.B. Jinesh, J.W.M. Frenken, in preparation for submission to *Phys. Rev. B*.
8. *Capillary ice formation and its effects on atomic-scale friction*
K.B. Jinesh, J.W.M. Frenken, in preparation for submission to *Phys. Rev. B*.
9. *Effect of externally excited lateral resonances on atomic-scale friction*
K.B. Jinesh, J.W.M. Frenken, in preparation for submission to *Phys. Rev. B*.

Other publications by K.B. Jinesh:

10. *Effects of size-quantization in the I-V characteristics of CdS bulk- nano junctions*

K.B. Jinesh, C.S. Kartha, K.P. Vijayakumar, *Appl. Surf. Sci.* **195**, 263 (2002).

11. *Role of excess Cadmium in the electrical properties of devices made of chemically deposited nano-CdS*

K.B. Jinesh, C.S. Kartha, K.P. Vijayakumar; *Appl. Surf. Sci.* **207**, 26 (2003).

12. *How quantum confinement comes in chemically deposited CdS? – A detailed XPS investigation*

K.B. Jinesh, K.C. Wilson, S. Thampi, C.S. Kartha, K.P. Vijayakumar, T. Abe, Y. Kashiwaba; *Physica E* **19**, 303 (2003).



Acknowledgements

For the successful completion of this thesis, constructive discussions with Prof. J.W.M. Frenken were very much benefited. Also, extended discussions with Prof. S. Yu Krylov and Dr. T.H. Oosterkamp on topics related to this thesis were very fruitful. Analyses of the experimental data of Dr. M. Dienwiebel, the computational works of H. Valk and J.A. Dijksman and the recent AFM measurements by V. Fokkema were optimal additions to the research described in this thesis. The professional support from the members of the FMD and the ELD is gratefully acknowledged.



Curriculum Vitae

K.B. Jinesh was born in Kapickad, Kerala (India) on 1 June 1978. After receiving his Bachelor's degree in Physics from Mahatma Gandhi University, Kerala, India, in 1998, he pursued his studies at the Department of Physics of the Cochin university of Science and Technology (CUSAT), Kerala, India, and obtained his Master's degree in Physics in 2000, specializing in quantum electronics with a thesis entitled "*Quantum clustered thin films of binary compound semiconductors*". As a PhD student he first joined the group of Dr. C. Narayana at the Jawaharlal Nehru Center for Advanced Scientific Research (JNCASR), Bangalore, India, in 2001, on a project entitled "*High-pressure Raman and Brillouin scattering studies of oxide thin films*". Later in December 2001, he joined in the Delft Institute of Microelectronics and Submicron Technology (DIMES) at the Delft University of Technology, the Netherlands, on a project entitled "*Excimer laser crystallization of amorphous silicon thin films*", under the supervision of Dr. R. Ishihara and Prof. C.I.M. Beenakker. From September 2002 to September 2006, he has worked as a PhD student in the Interface Physics Group of Prof. J.W.M. Frenken, at the Kamerlingh Onnes Laboratory, Leiden University, the Netherlands. His research in this period on fundamental aspects of atomic-scale friction has formed the basis for the present PhD thesis on "*Atomic-Scale Friction: Thermal Effects and Capillary Condensation*".

